UCGE Reports
Number 20384

Department of Geomatics Engineering

Multi-Resolution Spectral Techniques for Static DGPS Error Analysis and Mitigation

(URL: http://www.geomatics.ucalgary.ca/graduatetheses)

by

Ahmed Adel El-Ghazouly

August, 2013

UNIVERSITY OF CALGARY

Multi-Resolution Spectral Techniques for Static DGPS Error Analysis and Mitigation

by

AHMED ADEL EL-GHAZOULY

A THESIS

SUBMITTED TO THE FACULTY OF GRADUATE STUDIES

IN PARTIAL FULFILMENT OF THE REQUIREMENTS FOR THE

DEGREE OF DOCTOR OF PHILOSOPHY

DEPARTMENT OF GEOMATICS ENGINEERING

CALGARY, ALBERTA

AUGUST, 2013

Abstract

GPS measurements can be modeled as a true range plus other errors such as orbital and clock biases, atmospheric residual, multipath, and observation noise. Modeling is one way to deal with some of these errors, if their characteristics are known (e.g. troposphere and ionosphere errors). Another way is to filter in the frequency domain, where all these errors have a different frequency spectrum component. Each error is characterized by a specific frequency band. For example, the receiver noise can be characterized with high-frequency components, multipath errors, which have low to medium frequency bands, while the ionospheric and tropospheric errors are at a lower frequency band.

Wavelet spectral techniques can separate GPS signals into sub-bands where different errors can be separated and mitigated. Using wavelets to transform the GPS measurements into frequency domain helps localize both location and frequency of GPS errors, which allows for easy error separation in frequency domain. This thesis introduces new wavelet spectral analysis techniques to mitigate DGPS errors in the frequency domain, namely cycle slip, code and phase multipath errors. The wavelet-based trend extraction model is applied to DGPS static baseline solutions and compared with the traditional de-noising technique. The de-trending methodology performed impressively for short baselines in RMS and bias reduction as the average RMS and bias reductions were around 80%. However, for longer baselines the bias reduction is minimal although the RMS reduction is still in the 70-80% reduction.

A second approach is introduced to detect and remove cycle slip errors, which can be seen as a singularity in the GPS data. The propagation of singularities between the levels of wavelet decomposition is different from the propagation of noise. This characteristic is used to identify the singularities from noise. The performance of the multi-scale singularity detection technique is evaluated and tested over GPS Code minus Carrier (CmC) and Phase1 minus Phase2 measurements where different cycle slips are added to the measurements. All the simulated cycle slips in CmC test quantities with SNR larger than 30 are effectively detected by the proposed technique. The error in the estimation process is, in most instances, less than 0.1 cycles.

Finally, the Multi-resolution Real-time (MRRT) Code-smoothing technique is introduced to real-time scenarios to mitigate code multipath error (medium to high-frequency) and noise (high-frequency) and retain the ionospheric error (low-frequency) untouched in the mitigation.

Preface

This thesis includes some material (e.g. figures, tables, formulas and texts) previously published, accepted or submitted in one pending patent, five journal papers and ten conference papers, as follows:

El-Ghazouly, A.; M. Elhabiby and N. El-Sheimy, "Wavelet-Based Carrier Phase Multipath Reduction", the United States and Trade Mark Office (Submitted, September 28th, 2008.12 pages).

El-Ghazouly, A.; Elhabiby, M. and El-Sheimy, N. (2013). "Medium to High Frequency DGPS Error Reduction using Two Step De-Noising Procedure". Journal of Geodetic Science. (submitted, May 24th, 2013. 24 pages)

El-Ghazouly, A.; Elhabiby, M. and El-Sheimy, N. (2013). "Cycle Slip Detection and Estimation using Multi-scale Wavelet Aided by Lipschitz-Regularity". Journal of Geodesy. (submitted, May 25th, 2013. 13 pages)

El-Ghazouly, A.; Elhabiby, M. and El-Sheimy, N. (2011). "Multi-resolution Real-time (MRRT) code-smoothing technique". Journal of Applied Geodesy, Volume 5 (Issue 3-4), 147-154,2011.

Elhabiby, M.; **El-Ghazouly, A.** and El-Sheimy, N. (2010). "Wavelet Spectral Techniques for GPS Errors Reduction". 7th International Conference on Electrical Engineering. May 25-27, 2010, Cairo, Egypt.

El-Ghazouly, A.; Elhabiby, M. and El-Sheimy, N. (2009). "Assessment of Wavelets Analysis for Carrier Phase Multipath Mitigation". Canadian Journal of Earth Sciences. Vol. 46. 627-636.doi:10.1139/E09-023.

El-Ghazouly, A.; Elhabiby, M. and El-Sheimy, N. (2010). ”De-Trending Multi-resolution technique to Reduce/Eliminate Long Baselines errors in Static GNSS Mode”. ENC 2010, Braunschweig, Germany, 19 – 21 October, 2010.

Elhabiby, M.; **El-Ghazouly, A.** and El-Sheimy, N. (2010). ”Multi-Resolution Ionospheric Attenuation for Single Frequency Receivers ”. INTERGEO 2010, Session 4, October 05-07, 2010, Messe Köln.Germany.

El-Ghazouly, A.; Elhabiby, M. and El-Sheimy, N. (2010). ”Code Smoothing and Multi-Resolution Analysis”. 2010 Joint Meeting with CMOS in Ottawa, May 31 - June 4.

El-Ghazouly, A. (2009). ”The Aid of Wavelets Correlator in Carrier Phase Multipath Reduction and Motion Detection”. ION GNSS 2009, Session E2: Multipath Effects & Mitigation, September 22-25, 2009, in Savannah, Georgia.

Elhabiby, M.; **El-Ghazouly, A.** and El-Sheimy, N. (2009). ”Singularity Detection Technique for GPS Cycle Slip in Wavelets Domain”. ION GNSS 2009, Session D4: Modeling & Algorithms, September 22-25, 2009, in Savannah, Georgia.

Elhabiby, M.; **El-Ghazouly, A.** and El-Sheimy, N. (2009). ”Wavelets for GPS Singularity Detection and Multipath Mitigation”. INTERGEO 2009, Session 4: Angewandte Geodäsie und GNSS, September 22-24, 2009, Messe Karlsruhe, Rheinstetten. Germany.

El-Ghazouly, A.; Elhabiby, M. and El-Sheimy, N. (2009). ” The use of Wavelets in GPS Error Analysis with Emphasis to Singularity Detection and Multipath Removal”, the American Geophysical Union Joint Assembly, 24-27 May, Toronto, Canada.

Elhabiby, M.; **El-Ghazouly, A.** and El-Sheimy, N. (2009). ”Evaluation of Wavelet Multipath Mitigation Technique in the Final Measurement Domain”. ION ITM 2009, Session C3: Algorithms and Methods 2 (Data Processing), January 26-28, in Anaheim, California.

Elhabiby, M.; **El-Ghazouly, A.** and El-Sheimy, N. (2008). ”A New Wavelet-Based Multipath Mitigation Technique”. ION GNSS 2008, Session C2: Multipath, September 16-19, 2008, in Savannah, Georgia.

El-Ghazouly, A.; Elhabiby, M. and El-Sheimy, N. (2008). ” GPS multipath mitigation in carrier phase double difference domain”, the Canadian Geophysical Union annual scientific Meeting, May 2008.

The above papers were produced by the author during the research phase of this thesis. The co-authors’ valuable feedback on the above materials is acknowledged. Use of the above material in this thesis is allowed by the co-authors and the journal/proceedings publishers.

Acknowledgements

First and foremost, I would like to thank my supervisor Professor Dr. Naser El-Sheimy for his valuable guidance, unwavering support and advice. It was my sincere pleasure to work under his supervision.

I wish to extend my appreciation and thanks to my co-supervisor Dr. Mohamed Elhabiby, for his professional supervision, guidance, vision, ideas and constructive feedback during my graduate studies. His abundant cooperation, positive attitude and understanding deserve everlasting appreciation.

Special thanks to my colleagues in my research group, Mobile Mapping Sensor Systems, for their wonderful friendship, support and valuable discussion: Dr. Sameh, Dr. Walid, Dr. Zainab, Dr. Wes, Dr. Yigiter, Sara, Adel, Abdelrahman and Mohamed Ali. Thanks to, Axel for helping me with data collection. As well, thanks to Dr. Taher, Dr. Wouter and Ossama for the amazing time, friendship and rich discussions. Also, I wish to extend my appreciation to Cansel Survey Equipment and David Davidson for providing GPS data through Can-Net. Also, I would like to extend my appreciation to Dr. Susan Skone for allowing me to use the Bernese software

I also would like to thank the entire faculty and staff members of the Geomatics Department, Schulich School of Engineering for providing a wonderful educational environment. In addition, I would like to thank all the faculty and staff of the Transportation Department, Alexandria University for their continuous support. Lastly, I would like to thank both Dr. Hassan El-Ghazouly and Dr. Kamal Atallah for their continuous encouragement, support and advice. Also, special thanks my friend Ismael for all the support.

This research was funded in part by the Natural Sciences and Engineering Research council of Canada (NSERC) and Canadian Centres of Excellences project grants of my supervisor. The Department of Geomatics Engineering Graduate Scholarships and Travel Grants, Department of Geomatics Engineering Graduate Research Supplement, Graduate Faculty Council Scholarship, Queen Elizabeth II Graduate (Doctoral) Scholarships, Alberta Ingenuity Fund (AIF) and Institute of Navigation best student paper award.

My loveling parents I owe you everything I have achieved. My brothers, Tamer, Hossam and my sister Ghada you are my backbone; thank you very much for your unconditional support and congratulations.

My great wife Dina, I love you. Thank you very much for coming with me to Calgary, for having faith in me, and for all the troubles, sacrifice, and hardships you took on to help me fulfill my dreams. Your help and support cannot be described with words; you are always great as usual. My lovely sons Khaled and Mohamed, my life has a meaning and it is because of you. I love you so much.

Dedication

To the love of my life
My Parents,
My Brothers and Sister,
My Wife
And My Sons

Table of Contents

List of Tables

List of Figures and Illustrations

Acronyms

C/A	Coarse/Acquisition
CMC	Code-Minus-Carrier
CORS	Continuously Operating Receiver Station
CS	Correlator Spacing
CsC	Carrier phase-smoothed Code
CmC	Code minus Carrier
CWT	Continuous Wavelet Transform
DD	Double Difference
DGPS	Differential GPS
DLL	Delay Lock Loop
GPS	Global Positioning System
IF	Ionosphere Free
IGS	International GNSS Service
LOS	Line-Of-Sight
LAAS	Local Area Augmentation System
MRRT	Multi-resolution Real-time
MP	Multipath
MRA	Multi-Resolution Analysis
MSE	Mean Squared Error
NGS	National Geodetic Survey
PLL	Phase Lock Loop
PRN#	GPS Satellite Vehicle Number #

RINEX	Receiver Independent Exchange Format
RMS	Root Mean Square
SD	Single Difference
SNR	Signal-to-Noise Ratio
STD	Standard Deviation
SP3	Standard Product 3 Orbit Format
TEC	Total Electron Content
WAAS	Wide Area Augmentation System

List of Symbols, Abbreviations and Nomenclature

Symbol	Definition
ψ	Wavelet base function
$\hat{\psi}(\omega)$	Fourier transform of ψ
$\mathbb{R}$	Set of all real numbers
Z	Set of all integers numbers
d_n^m	Detailing coefficients at scale m and shift n
λ_0	Scale space parameter
c_n^m	Approximation coefficients
d_n^m	Detailed coefficients
$\nabla\Delta$	Double difference operator
λ	Carrier wavelength
ϕ_M	Measured carrier phase in cycles
ρ	The true receiver to satellite geometric range
N	Carrier phase ambiguity
d_{ION}	Ionospheric delay error
d_{Trop}	Tropospheric delay error
d_{EPHEM}	Satellite ephemeris error
d_{ϕ}	Other carrier phase errors in meters, such as Multipath, receiver biases and thermal noise
p_M	Pseudo range measurements

d_p	Multipath and thermal noise errors
$E\,[]$	The expectation operator
$p_v(t)$	Polynomial part of the signal
$e_\alpha(t).$	Error part of the signal
u	Translation to the Wavelet base function
s	Scaling to the Wavelet base function
$f(t)$	Any function
V_0	The original space
$\mathrm{I}_{\{\lvert \mathrm{d}_\mathrm{n}^\mathrm{m} \rvert > \delta\}}$	Indicator function
δ'	Soft threshold value
δ	Hard threshold value
P	Square of the wavelets coefficients
$R(\,k)$	The risk function
$median$	Intermediate values of operation
$d_j(k)$	High-frequency coefficient
g_n	Detailed coefficients (highpass filter)
h_n	Scaling coefficients (lowpass filter)

Chapter One: Introduction

GPS measurements can be modeled as a true range plus other errors such as orbital and clock biases, atmospheric residual, multipath, and observation noise. Modeling is one way to deal with some of these errors, if their characteristics are known (e.g. troposphere and ionosphere errors). Some error sources, such as atmospheric delays, orbital, and clock errors are spatially correlated and generally cancelled out or reduced through the double differencing process. A linear combination of measurements is used to combine the two L-band frequencies to filter out ionospheric delay.

Another way to deal with these errors is to filter in the frequency domain, where all these errors have a different frequency spectrum component. Each error is characterized by a specific frequency band—e.g. the receiver noise can be characterized by high-frequency components, multipath errors, which have low to medium frequency bands, while the ionospheric and tropospheric errors are at a lower frequency band. Analyzing GPS errors and determining their characteristics, in the frequency domain, helps to separate some of these errors from the Line-Of-Sight (LOS) measurements. This reduces or even mitigates some of these errors, especially the errors that cannot be entirely mitigated by modelling or differencing, such as multipath.

This thesis addresses several GPS errors, namely phase multipath, code multipath and cycle slip errors along with their respective characteristics in the multi-resolution frequency domain. Wavelet analysis is a powerful mathematical tool that has been successfully used in a variety of applications such as data compression, de-noising, pattern recognition, sub-band coding, filtering, outlier detection, and operators approximation (Chui, 1992; Keller, 2004; Mallat, 1998). It is considered a mathematical microscope due to its reliable localized time–frequency properties, which provide an accurate location of the transient component in the signal while retaining information about the fundamental frequency. Using wavelets to transform the GPS measurements into frequency domain helps localize both location and frequency errors, which allows for easy error separation in frequency domain.

This research work will introduce a group of developments that utilize multi-resolution aided techniques to conduct on GPS signals and signal combinations (code minus carrier and double difference carrier) to mitigate inherent GPS measurement errors. These techniques are applicable to two general GPS architectures:

1) single-frequency architectures; and
2) multi-frequency architectures.

In the case of a single frequency GPS architecture, the multi-resolution techniques are applied to code minus carrier and carrier phase measurements to mitigate pseudo-range and carrier phase errors. The multi-resolution correction techniques can be used to mitigate correlated errors (i.e. multipath and atmospheric errors) and to detect/remove cycle slip on a single receiver when using code minus carrier observables or on two receivers when using double differenced carrier phase measurements.

For multi-frequency GPS architecture the first order ionospheric errors are removed by linear combinations. Multi-resolution techniques are used to mitigate multipath and atmospheric errors in addition to detecting/removing cycle slip. In this case Ionosphere-Free linear combination is used to mitigate the first order ionospheric errors by linearly combining L1 and L2 signals. Different test scenarios are involved in this research to cover all errors previously discussed and their mitigation techniques. Short baselines (a few hundred meters to five kilometres), where multipath is the main error source and most other errors are correlated, were tested to determine the effectiveness of different multi-resolution techniques in multipath mitigation. Subsequently, test scenarios for medium to long baselines (20 kilometres to 50 kilometres) were made based on L1 fixed solution, Ionosphere Free (IF) float solution and Ionosphere Free (IF) fixed solution in batch processing mode, respectively.

1.1 Motivation

The primary motivation of this thesis is to improve GPS measurement accuracies by classifying errors in the frequency domain and subsequently separating, mitigating and decreasing them. Irregular variations, such as measurement noise and high-frequency multipath, can be mitigated in the high-frequency band. Errors in this frequency category are mitigated using multi-resolution de-noising techniques. Despite occurring in the high-frequency band, cycle slip errors cannot be removed by multi-resolution de-noising techniques. This error is considered a singularity in GPS measurements and should be detected and removed using the multi-resolution singularity detection techniques. In contrast, ionospheric errors and low-frequency multipath are regular variations that occur in the low-frequency band. Errors in this frequency band should not be mitigated using regular multi-resolution de-noising techniques but rather by modeling and differencing techniques.

This thesis investigates and assesses the performance of different multi-resolution techniques to mitigate DGPS errors in the frequency domain. Multi-resolution techniques can separate GPS signals into sub-bands where different errors can be separated and mitigated. As described, each error should be mitigated separately with the technique that suits the frequency category into which the error occurs.

1.2 Research objectives

The ultimate goal of this research is to develop and implement a multi-resolution tool box for DGPS error analysis and mitigation for static application. The main objectives of this thesis are outlined as follows:

- Investigate static GPS error characteristics in frequency domains, from short to long baselines code and carrier phase measurements.
- Investigate two different measurement combinations namely, code minus carrier and double difference.
- Evaluate the most optimum use of wavelets to reduce or remove high-frequency errors by exploring different wavelet de-noising parameters.
- Develop and test a multi-resolution de-trending tool for low-frequency error mitigation.

- Develop and test a singularity detection and estimation technique for detecting cycle slip location and magnitude in a signal contaminated with noise.
- Develop and test a real-time code multipath mitigation technique that eliminate multipath (medium to high-frequency) and noise (high-frequency) and retain the ionospheric error (low-frequency) untouched in the mitigation procedure.

1.3 Contributions

By conducting the fundamental theoretical research outlined in this thesis, and keeping practical implementation issues in mind, it is hoped that the results will be useful to researchers and GNSS software developers involved in the batch processing of static GNSS data applications.

In precise GPS applications, the estimation of precise DGPS corrections is crucial for slope/landslide, ground subsidence and large structure deformation monitoring. In these scenarios, it is important to correctly interpret the actual observations as closely as possible rather than the combined residual effects of multipath and other systematic errors. The combination of the remaining non-common errors both at the reference and at the point of observations characteristically forms a noise-like variation in the time domain. The magnitude of these errors changes mainly with observation site and time. This thesis will study, analyze and provide new techniques that will help mitigate these errors in the frequency domain.

Using the wavelet transform as a tool to detect and remove cycle slip is simple to implement and does not need any a priori value. However, it does not yield good results on noisy signals (i.e. phase-code combination). This thesis will introduce a new technique based on CWT combined with the Lipchitz exponent to detect the cycle clip singularities and separate between it and the noise.

1.4 Thesis Outline

The next two chapters will present relevant background material to this thesis. Wavelet theory will be discussed in Chapter 2 as well as GPS concepts and the types of errors that affect GPS observations. Chapter 3 will present a description of the field experiments, data collection methods and the computation of reference coordinates. There are three data sets, and the details on how, where, and when they were collected are provided in this chapter. Additionally, the spectral analysis of double difference data will be discussed for short and long baselines, as well as correlation error identification in the double difference domain.

Chapter 4 describes different techniques to eliminate/reduce correlated errors namely, de-noising and de-trending. It offers a detailed analysis of the best wavelet base function and threshold technique estimator by comparing different wavelet parameters along with various thresholding techniques. The two techniques explained in this chapter are applied to the data set introduced in Chapter 3 for short and long baseline. Based on these analyses, the performance of both techniques is discussed and evaluated on baselines of 100 m to 50 km.

Chapter 5 introduces a new multi-scale singularity detection and estimation technique for detecting cycle slip location and magnitude in a signal contaminated with noise. In this chapter, the property of wavelet base function (e.g. compact support and smooth functions) is discussed and the procedure for selecting a wavelet base function that annihilates the low order polynomial in the signal without data fitting is introduced. The performance of the proposed technique is tested over code minus carrier, a geometry-free linear combination GPS data and a simulated slip. In addition, the ability of the proposed multi-scale technique to detect and estimate cycle slips over low signal to noise ratio is investigated.

Chapter 6 introduces the use of a code-smoothing technique—the Multi-resolution Real-time (MRRT) Code-smoothing technique. This technique is used in real-time scenarios to mitigate code multipath error (medium to high-frequency) and noise (high-frequency) and retain the ionospheric error (low-frequency) untouched in the mitigation procedure.

Chapter 7 provides a summary of this research in addition to recommendations for future work in this field of study.

Chapter Two: Background and Literature

2.1 Introduction

Differential Global Positioning System (DGPS) is one of the most popular and reliable techniques for improving GPS accuracy by minimizing correlated errors between reference stations and rovers. DGPS can be used to correct code (code DGPS) or carrier (carrier DGPS) in both real-time and post processing modes. The performance of DGPS depends on a number of factors such as the quality of base station data, quality of rover data, and distance between the reference and the rover. As the distance between the reference and rover increases, DGPS positioning errors become more de-correlated. Double Differencing (DD), Code minus Carrier (CmC) are used to reduce and/or eliminate many of the correlated GPS biases, such as the atmospheric delays, the receiver and satellite clock biases, and orbit error (Satirapod and Rizos, 2005). This chapter focuses on the definition of three types of errors—multipath, cycle slip, ionosphere and troposphere—that will be mitigated or reduced by multi-resolution techniques. These errors, and the multi-resolution techniques used to reduce them, will be explored and discussed in greater detail in the following sections.

2.2 Wavelet Spectral Analysis

Wavelet transform is a tool that represents data, functions or operators into different frequency components, essentially “cutting up” data. This tool is used to study each component with a resolution that matches its scale (Daubechies, 1992). In the last two decades wavelets have been used extensively in different research fields. It has many potential applications such as image processing, medical diagnostics, pattern recognition, geophysical signal processing, boundary value problems, and electromagnetic wave scattering.

2.2.1 Continuous Wavelet Transform

A wavelet (ψ) is a function $\psi \in L^2(\mathbb{R})$ that follows the integral in Equation (2-1) where $\hat{\psi}(\omega)$ is the Fourier transform of ψ. One requirement for this integral to be finite is that $\hat{\psi}(0) = 0$, otherwise the integral is divergent implying that the Fourier transform of the wavelet function vanishes at zero frequency. Based on the definition of Fourier transform, this means that the average value of the wavelet in the time domain must be zero (Equation (2-2)) (Mallat and Hwang, 1992)**:**

$$C_\psi = \int_0^\infty \frac{\left|\hat{\psi}(\omega)\right|^2}{\omega} d\omega < \infty \tag{2-1}$$

$$\hat{\psi}(0) = 0 \iff \int_{-\infty}^{\infty} \psi(t)\, dt = 0 \tag{2-2}$$

The wavelets or daughter wavelets (Equation (2-3)) are generated by translating (u) and scaling (s) the wavelet base function.

$$\psi_{u,s} = \frac{1}{\sqrt{s}} \psi(\frac{t-u}{s}) \tag{2-3}$$

Wavelet transform is a measure of the similarity between the scaled and shifted versions of the wavelet base function and the original signal itself. The Continuous Wavelet

Transform (CWT) of a function $f(t)$ with respect to wavelet base function $\psi(t)$ is defined as the dot product between $\langle f(t), \psi(t)\rangle$:

$$Wf(u,s) = \int_{-\infty}^{\infty} f(t)\frac{1}{\sqrt{s}}\psi^*(\frac{t-u}{s})\,dt \qquad (2\text{-}4)$$

Where ψ^* is the complex conjugate of ψ and $Wf(u,s)$ is the wavelets coefficient.

If the wavelet base function $\psi(t)$satisfies the admissibility condition in Equation (2-1), the CWT can preserve all the information and $f(t)$can be recovered from its CWT coefficients using the following equation:

$$f(t) = \frac{1}{C_\psi}\int_{0}^{+\infty}\int_{-\infty}^{+\infty} Wf(u,s)\frac{1}{\sqrt{s}}\psi^*(\frac{t-u}{s})\,du\frac{ds}{s^2} \qquad (2\text{-}5)$$

2.2.2 Discrete Wavelet Transform

For easy computer implementation, the discrete wavelet transform (DWT) is implemented. Every one-dimensional signal S can be represented using wavelet base functions as follows (Keller, 2004):

$$S(t) = \sum_{m\in \mathrm{Z}}\sum_{n\in \mathrm{Z}} d_n^m \psi_{m,n}^{(\lambda_0,t_0)}(t) \qquad (2\text{-}6)$$

where

$$d_n^m(t) = (S(t), \psi_{m,n}^{(\lambda_0,t_0)}) = \sum_n S(t)\psi_{m,n}^{(\lambda_0,t_0)}(t) \qquad (2\text{-}7)$$

Where ($\mathbb{R}$ and Z) represent the set of all integers and real numbers.

$$\psi_{m,n}^{(\lambda_0,t_0)}(t) = \lambda_0^{-m/2}\psi(\lambda_0^{-m}t - nt_0) \qquad (2\text{-}8)$$

In equation (2-7) d_n^m is the detail coefficient, $\psi_{m,n}$ is the wavelets function generated from the original mother wavelets $\psi \in L^2(\mathbb{R})$, λ_0 is the scale space parameter, t_0 is the translation space parameter, m is the scale or level of decomposition, and n is the shifting or translation integer.

The scale and translation parameters form a wavelet's frame where the signal is completely represented by its spectrum. The representation is on a dense grid for small scales and on a wide grid for large scale. For practical reasons, a dyadic frame is used with $\lambda_0 = 2$ and t_0= 1 (Elhabiby, 2007; Keller, 2004).

2.2.3 Multi-Resolution Concept

The concept of Multi-Resolution Analysis (MRA) is introduced for the construction of orthogonal wavelet bases and for the rapid decomposition of a signal into independent frequency bands through a nested sequence, as follows (Keller, 2004; Mallat, 1998):

$$0 \subset \ldots \subset V_2 \subset V_1 \subset V_0 \subset V_{-1} \subset \ldots . \subset L_2(\mathbb{R}) \qquad \textbf{(2-9)}$$

Where

$$\overline{\underset{m \in Z}{U} V_m} = L_2(\mathbb{R}) \qquad \textbf{(2-10)}$$

$$\underset{m \in Z}{\cap} = \{0\} \qquad \textbf{(2-11)}$$

$$S(\bullet) \in V_m \Leftrightarrow S(2^m \bullet) \in V_0 \qquad \textbf{(2-12)}$$

And the scaling function $\Phi_{m,n} \in L_2(\mathbb{R})$ with

$$V_0 = \overline{span\{\Phi(\bullet - k) \mid k \in Z\}} \tag{2-13}$$

$$\begin{tikzcd}
V_{-1} \arrow[r] \arrow[dr] & V_0 \arrow[r] & V_1 \arrow[r] & V_2 \\
& W_0 \arrow[r] & W_1 \arrow[r] & W_2
\end{tikzcd}$$

Figure 2-1: Multi-resolution analysis using nested sequence

Figure 2-1 and Equation (2-9) illustrate that all spaces of the MRA are a scaled version of the original space V_{-1}, which is spanned by a shifted version of the scaling function $\Phi_{m,n}$ into other space V spaces (approximation) and the wavelet function $\psi_{m,n}$ into W spaces (detailing). In addition to Equation (2-7), another inner product is used for the decomposition of the signal S using scaling function $\Phi_{m,n}$ as:

$$c_n^m = \langle S, \Phi_{m,n} \rangle = \sum_n S(t)\Phi_{m,n}(t) \tag{2-14}$$

From Equation (2-7) and (2-14), which form the wavelet frame, it can be seen that the signal is always represented by approximation coefficients c_n^m and d_n^m detailed part. A number of scaling coefficients (low-pass filter) h_n represent the scaling function, which is the base of space V_0 that is,

$$\Phi(t) = \sqrt{2}\sum_{n \in Z} h_n \Phi(2t - n) \tag{2-15}$$

The base of W_0 is represented by detailing function Ψ , where

$$\Psi(t) = \sqrt{2}\sum_{n\in Z} g_n \Phi(2t-n) \qquad \textbf{(2-16)}$$

Ψ is the wavelet function that is generated from the original mother wavelet function, and g_n are the detailed coefficients (high-pass filter). The relation between the scaling coefficients and the detailed coefficients is:

$$g_n = (-1)^n h_{1-n} \qquad \textbf{(2-17)}$$

The wavelets procedure used in this research is based on the Mallat algorithm, which consists of the following two equations (Keller, 2004; Mallat, 1998; Strang and Nguyen, 1996):

$$c_n^m = \langle S, \Phi_{m,n} \rangle = \sum_{l\in Z} h_l \langle S, \Phi_{m-1,2n+1} \rangle = \sum_{l\in Z} h_{l-2n} c_l^{(m-1)} \qquad \textbf{(2-18)}$$

$$d_n^m = \langle S, \psi_{m,n} \rangle = \sum_{l\in Z} g_l \langle S, \psi_{m-1,2n+1} \rangle = \sum_{l\in Z} g_{l-2n} c_l^{m-1} \qquad \textbf{(2-19)}$$

Where *l* is the level of decomposition.

2.3 Observed Differential GPS Mode Errors

The carrier phase and code double difference model between two satellites and two receivers can be written as follows (Grewal et al., 2007):

$$\nabla\Delta\lambda\phi_M = \nabla\Delta\rho + \lambda\nabla\Delta N - \nabla\Delta d_{ION} + \nabla\Delta d_{TROP} + \nabla\Delta d_{EPHEM} + \nabla\Delta d_\phi \qquad \textbf{(2-20)}$$

$$\nabla\Delta p_m = \nabla\Delta\rho + \nabla\Delta d_{ION} + \nabla\Delta d_{TROP} + \nabla\Delta d_{EPHEM} + \nabla\Delta d_P \qquad \textbf{(2-21)}$$

where $\nabla\Delta$ indicates double difference operator and λ is a carrier wavelength (0.1903 m for L_1 and 0.2442 m for L_2). ϕ_M is the measured carrier phase in cycles, ρ is the true receiver to satellite geometric range in meters, N is carrier phase ambiguity in cycles, d_{ION} is ionospheric delay error in meters, d_{Trop} is tropospheric delay error in meters, d_{EPHEM} is the delay error in meters because of satellite ephemeris error, and d_{ϕ} represents other carrier phase errors in meters, such as multipath, receiver biases and thermal noise. p_M is the pseudo-range measurements in meters and d_p represents the multipath and thermal noise errors.

To improve the position accuracy and reduce the effects of the ionosphere several carrier phase combinations and ambiguity resolution strategies can be derived. In general, carrier phase combinations involve carrier phase measurements (ϕ) on two frequencies, L1 and L2, which are combined in the following manner:

$$\phi_{ij}^{kl}(\beta_1, \beta_2) = \beta_1 \phi_{ij}^{kl}(L1) + \beta_2 \phi_{ij}^{kl}(L2) \quad \textbf{(2-22)}$$

The above equation, shows a linear combination of dual-frequency measurements at a particular epoch between two stations (i and j) and two satellites (k and l). A number of combinations can be formed using Equation (**2-22**) depending on the choice of the coefficients, β_1 and β_2. Using the values of $\beta_1 = 1$ and $\beta_2 = -1$ leads to the most commonly used carrier phase, which referred to as the widelane because of the increase in the wavelength to approximately 86.2 cm, facilitating improved ambiguity resolution in terms of ease and time to fix. However, the noise error, multipath and ionospheric errors are amplified in the widelane combination when compared to the error level in L1 signal. As a result, the position estimate of a widelane combination will suffer from higher position errors than the position determined from L1 only assuming the ambiguity is resolved in both cases. The narrow lane combination is formed when $\beta_1 = 1$ and $\beta_2 = 1$, which leads to a much shorter wavelength, only 10.7 cm, which leads to significantly reduced measurement noise over other common phase combinations.

The ionospheric-free (IF) phase combination can be derived when $\beta_1 = 1$ and $\beta_2 = -\frac{f_{L2}}{f_{L1}}$, which theoretically eliminates the first order effects of the ionosphere. The remaining higher order effects (approximately 0.1%) may be on the order of a few centimetres under high ionospheric conditions, which is significant for some precise applications (Klobuchar, 1996).

It should be mentioned here that even though the first order ionospheric effect is removed, the measurement noise also increases. It can be shown, through simple error propagation of Equation (**2-22**), that the effective noise of the IF observable increases with respect to the L1 and L2 observables as follows:

$$\sigma_{IF} = \sqrt{(\beta_1\, \sigma_{L1})^2 + (\beta_2\, \sigma_{L2})^2} \qquad \textbf{(2-23)}$$

Another drawback of using the IF combination is that the integer nature of the ambiguities is not retained.

Another linear combination strategy that will not suffer from the ionospheric error and keep the ambiguity fixed is the Ionosphere Free Fixed linear combination. This strategy is a cascading scheme that required the fixation of widelane ambiguity first and the creation of modified Ionosphere free observation. Blewitt, (1989) and Liu, (2003) give a detail description of this approach.

As the distance between rover and reference receivers decreases, DGPS positioning errors become more correlated; i.e. ionospheric, tropospheric, and orbital errors. As a result, in cases of short baseline (hundreds of meters to one kilometre), these errors are mitigated in double difference mode and Equation (2-20) and (2-21)can be rewritten as follows:

$$\nabla\Delta\lambda\phi_M = \nabla\Delta\rho + \lambda\nabla\Delta N + \nabla\Delta d_\phi \quad \textbf{(2-24)}$$

$$\nabla\Delta p_m = \nabla\Delta\rho + \nabla\Delta d_P \quad \textbf{(2-25)}$$

Generally, DGPS is used in static mode when the rover is used as a base station, and also in kinematic mode, where the rover is moving. In both modes the behaviour of DGPS errors is different and must be accounted for in different ways. This research thesis will focus on three types of errors, namely multipath, cycle slip, ionosphere and troposphere. In the following section the aforementioned errors and state-of-the-art techniques from the literature will be discussed in further detail.

2.3.1 Multipath Error

I. Pseudo-range Multipath

GPS receivers provide diverse measurements, namely the code and carrier phase measurements. The measurements rates between successive epochs are similar in both observables, but the change in carrier phase can be determined on one order of magnitude higher than the change in code. This diversity of measurements is used in the measurements domain to improve position accuracy. The code measurements are contaminated with diverse errors that fall in different frequency bands (i.e., multipath error, falls in a high to medium frequency band [0.1 to 0.003 Hz], whereas the ionospheric error is in the lower frequency band [0 to 1.2e–4 Hz]). As these errors have different frequency components, the proposed mitigation methodology is presented whereby the multipath error can be removed through frequency domain processing.

Understanding the basic concept behind signal acquisition and tracking within a GPS receiver is essential to understand the behavior of multipath error on the GPS observables. In a simplified explanation, the received GPS signal is mixed with a locally-generated reference signal leading to an intermediate frequency (IF). The IF signal is separately integrated with cosine and sine versions of a locally-generated carrier signal, yielding in-phase and quadrature channels, referred to as I and Q, respectively. For code tracking, the I and Q channels are correlated with a locally-generated version of the PRN code by shifting the local code in time until maximum correlation is achieved between local and received signals.

The Delay Lock Loops (DLLs) correlation algorithm is used by many receiver manufactures to track the GPS pseudo-range signal. Perfect correlation of the tracked signal with the receiver-generated replica signal results in an ideal triangle with peak correlation achieved at the position of the prompt correlator. However, when multipath occurs, one or more smaller correlation peaks are introduced and summing these multipath correlation functions with the true or direct signal correlation leads distorted functions (Misra and Enge, 2006).

GPS receiver correlators and signal processors are designed to suppress reflected signals which demonstrate delays (relative to the direct signal) that exceed one chip (Misra and Enge, 2006). Many multipath mitigation techniques in the receiver currently exist and are based on enhancing the DLL technique. Tracking loop designs involve the use of a series of early, late and prompt correlators which serve as multipath filters. Narrow correlator (van Dierendonck et al., 1992) is a modification of the DLL that provides some multipath rejection. This is achieved by reducing the Early-Late spacing of the DLL, and increasing the correlation bandwidth. With this technique, the jitter is reduced, and the range of multipath delays that affect the DLL tracking point is shorter. Multipath Estimation Delay Lock Loop (MEDLL) Townsend and Fenton (1994), performs an estimation of the amplitudes and delays of the direct and multipath components using the Maximum Likelihood Principle. These estimations are then employed to drive code and carrier generators that close the tracking loop. The estimation is performed at the output of a bank of matched correlators with 0.1 chip spacing.

Another way of multipath modeling is the environment-specific multipath mapping which is done based on prior knowledge of the environment in the vicinity of the GPS receiver, which can be the case for static reciever. Bradbury et al. (2007) simulate a single-reflection specular multipath using a computerized city in an attempt to predict multipath behavior in urban environments. This model attempts to determine and identify the number of multipath-reflecting surfaces as a function of the code correlation spacing of the GPS receiver used. In a different approach, Weiss et al. (2006) compared 24 hours of GPS-estimated multipath error to multipath error that had been simulated using a ±20 cm accurate LiDAR DTM (Light Detection And Ranging Digital Terrain Model) of a CORS site and found that elevation-dependent multipath statistics displayed an overall ±11 cm agreement.

Neither onboard multipath-mitigating GPS receiver algorithms nor well-placed multipath-resistant GPS antennas can completely eradicate the multipath effect. As a result, further processing is needed in post-signal-reception mode at the GPS code measurements. This would involve implementation of algorithms which manipulate the GPS data logged in raw data files.

In 1982, Ron Hatch was the first to introduce the concept of Carrier-smoothed Code (CsC) by using integrated carrier phase measurements to smooth the corresponding code measurement (Hatch, 1982). This technique, named Range Domain Hatch filter (RDH), introduces the CsC to the pseudo-range observations in the measurements domain. The CsC technique can effectively remove high and medium frequency errors such as receiver noise and some multipath errors, but low-frequency errors (ionosphere and low rate multipath) can accumulate as a bias at the output of this smoothing procedure, especially, with single frequency receivers. This bias arises because the ionospheric error affects both carrier phase and code measurements equally, but opposite in sign. The code measurement is delayed and the carrier phase measurement is advanced when passing through the ionospheric layer. As a result, the code and carrier measurements diverge from each other at twice the rate of ionospheric change. Therefore, the ionospheric error must be removed first and separately from the rest of the errors before the smoothing procedure can begin. Keeping the ionospheric divergence in the smoothing procedure will cause the resulting smooth-code measurements to be biased and consequently, will deteriorate the final position solution. One way to reduce the effect of the ionospheric divergence, used in safety of life applications such as Wide/Local Area Augmentation (WAAS and LAAS), is to use a conservative constant carrier smoothing time (100 seconds) (RTCA Inc., 1998).

Shallberg et al. (2001) introduces the Code Noise and Multipath algorithm (CNMP) for dual-frequency users, which generates a multipath-corrected code by combining the code and carrier phase measurements. However, the CNMP is only applicable to dual-frequency receiver users and is very similar to the ionosphere-free linear combination. Zhang and Bartone (2004) proposed a multipath mitigation method in the frequency domain using Fast Fourier Transform (FFT). This technique, in which the filter block size must be close to the multipath cycle to capture most of the error, requires previous knowledge of multipath fading frequency. In 2004, Zhang and Bartone introduced the wavelet multi-resolution technique (WAVESMOOTH) as a tool to mitigate the multipath error in real-time scenarios (Zhang and Bartone, 2004). This technique showed significant potential in multipath mitigation overall, but failed to tackle the core of the problem in real-time mitigation (i.e. bias elimination (ambiguity), noise reduction, boundary problems.)

Chapter six of this research thesis introduces a code-smoothing technique, the multi-resolution real-time (MRRT) code-smoothing technique. This technique is used in real-time scenarios to mitigate multipath error (medium to high-frequency) and noise (high-frequency). It is also used to retain the ionospheric error (low-frequency) untouched in the mitigation procedure (El-Ghazouly et al., 2011). The proposed MRRT technique is superior to those in the literature in that it effectively removes the multipath and noise in real-time scenarios and retains unbiased low variance smoothed code.

II. Carrier phase multipath

Multipath is a combination of high, medium and low frequency errors that contaminate carrier and code measurements (Zhang and Bartone, 2004). Multipath error is a highly localized error that depends on the satellite receiver geometry and cannot be mitigated by differentiation. This is why multipath is one of the most dominant sources of error in GPS positioning.

Carrier phase multipath occurs when the receiver tracks the sum of the direct and multipath signals. As explained in the pseudo-range multipath section, the code is stripped from the incoming signal by correlating the local and received codes, leaving only the received carrier in I and Q channels. The carrier tracking loop is introduced to the recovered signal to match up the recovered carrier with a locally-generated version by minimizing their phase difference. Once the locally-generated carrier's frequency has been looked on the incoming carrier, the carrier phase measurement (the change in phase of the signal over time) is generated by the tracking loop.

The carrier tracking loop can be represented by the phase relationship between the I and Q channels in terms of a phasor diagram (Figure 2-2). In case of multipath free signal, the phasor diagram would contain a single phasor of amplitude A_d; and the misalignment between the local and incoming carriers results in a nonzero phase angle ϕ_d. The carrier phase measurements is generated by keeping track of the misalignment phase ϕ_d. In case of signal with multipath, the multipath signal (A_m) will add one or more phasors to the phasor diagram. The carrier tracking loop attempts to track a composite signal (A_C) which is the vector sum of all phasors (direct plus multipathed), which will cause an incorrect phase measurement with phase error $\delta\phi$.

The phase error due to multipath can be derived from geometric relationships expressed in the phasor diagram and can be described in terms of the multipath parameters:

$$\tan(\delta\phi) = \frac{A_m \sin(\psi)}{A_d + A_m \cos(\psi)} \tag{2-26}$$

The magnitude of the phase error evolves over time as the phase difference between direct and multipath signals changes. In terms of the phasor diagram, changes in ψ cause the multipath phasor to spin around the end of the direct phasor. The phase errors then oscillate between an absolute maximum $\delta\phi$ when ψ = 90± or 270± and a minimum (no phase error) when ψ = 0± or 180±. If the signal is un attenuated at the reflection interface, the direct signal amplitude is equal to the reflected signal amplitude. From this maximum value and Equation **(2-26)** , it is apparent that carrier-phase errors can reach a maximum total phase error of 0.25λ, i.e. 4.7 cm for L1 and 6.1 cm for L2 phase measurements. When phase data are combined in common linear observable combinations for analysis, multipath errors are amplified by 2 to 9 times their single-frequency values.

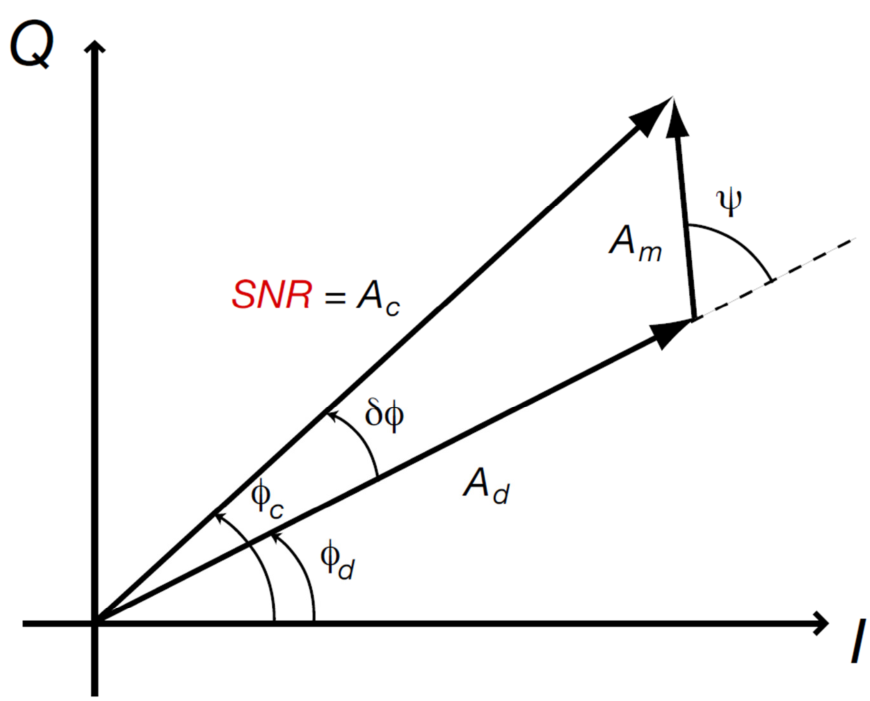

Figure 2-2: Phasor diagram of direct, reflected and composite signals and carrier phase multipath error. (after Ray,2000)

The multipath frequency depends upon the rate of change of the multipath phase, or the differential path delay. The multipath frequency caused by a single dominant reflector may be computed by the Equation (**2-27**) given by (Ray 2000). This equation is built upon the assumption that only one reflected signal is used.

$$\frac{\delta\gamma_{01}}{\delta t} = \frac{2\pi d_1}{\lambda_L}\left(\{\sin\theta.\cos(\varphi-\varphi_1) - \cos\theta.\tan\theta_1\}\frac{\delta\theta}{\delta t} + \{\cos\theta.\sin(\varphi-\varphi_1)\}\frac{\delta\varphi}{\delta t} \right) \qquad \textbf{(2-27)}$$

where γ_{01} is the reflected signal phase at the antenna phase center, $\frac{\delta\gamma_{01}}{\delta t}$ is the multipath error variation (frequency) from the variation in the multipath phase or differential path delay, d_1 is the horizontal distance between the antenna and the reflector, λ_L is the wavelength of the carrier, θ and θ_1 are the elevation of the direct satellite signal and the reflected signal, and φ and φ_1 are the azimuth of the direct and reflected signals.

The equation above relates multipath error frequency with satellite dynamics. The expression is obtained under the assumption that the antenna reflector geometry (defined by d_1, θ_1 and φ_1) does not change significantly over the period under consideration. It is seen from Equation (**2-27**) that the multipath error frequency is directly proportional to both the rate of change of elevation and azimuth of satellite, and it is reversely proportional to the wavelength of the carrier signal. This means that a low elevation satellite is more likely to cause multipath error, as a result of more potential reflectors, and a high elevation satellite is less likely to cause multipath errors. Moreover, from Equation (**2-27**), the multipath frequency error is directly proportional to the distance between the multipath reflector (such as buildings or trees) and the antenna, which means that by having large distances between the reflectors and the antenna, high frequencies will be introduced, and by having short distances between the reflectors and the antenna, long frequencies will exist. The former can be reduced by de-noising and the latter requires de-trending. The long wavelengths from near reflectors, which are mainly the case, lead to significant degradation in the accuracy of the carrier phase.

Many approaches to mitigate multipath error at different domains have been developed in the past three decades. The first step for multipath mitigation begins at the GPS antenna, which usually is referred to as Radio Frequency (RF) domain, to separate the Line Of Sight (LOS) signal from the reflected/diffracted signal. Multipath separation at this level can be accomplished using different approaches. One of the most successful approaches at this level is to control the antenna gain for Left Hand Circularly Polarized (LHCP) and low elevation signals (Braasch, 1994; Counselman, 1998; Izadpanah et al., 2008). NovAtel designed and introduced a novel antenna to the markets—the NovAtel pinwheel antenna, which is based on an array of coupled spiral slots in a pinwheel type configuration (Kunysz, 2005). This antenna is considered a compact version of the chock ring antenna and has comparable performance. However, the main drawbacks to each of these methods are their high cost, large size and weight. Furthermore, they reject a large number of signals, which results in the degradation of the satellite geometry—ultimately affecting the final position accuracy. Park et al., (2004), however, prove that no antenna design or environment is completely multipath-free by analyzing GPS measurements from a worldwide control station operating with different antenna types. Therefore, there is a need for a real-time/post processing extended methodology to solve this issue.

The next stage of multipath mitigation occurs after both the LOS and multipath signals are received inside the receiver. The multipath error is reduced at this point by two different approaches: by modifying the tracking loop discriminator to make it sensitive to multipath error and by estimating the parameters (amplitude, phase and delay) for the LOS and multipath signals. Modification of the tracking loop discriminator required state of the art advancements beginning with a narrow correlator (Van Dierendonck et al., 1992), which led to significant multipath reductions using 0.1 chip spacing and larger band width (Cannon et al., 1994). Several other developments were made based on the same concept such as Strop and Enhanced Strop correlator (Garin and Rousseau, 1997), the Edge correlator (Garin et al., 1996) and the PAC correlator (Jones et al., 2004). All of these correlators achieved good performances with long delay multipath signals greater than 10 m. However, the error due to reflected signal from distances less than 10 m was not reduced (Fenton and Jones, 2005).

The estimation of parameters for LOS and multipath signals is a technique that contains the Multipath Elimination Technique (MET) (Townsend and Fenton, 1994), the Multipath Estimation Delay Lock Loop (MEDLL) (Van Nee, 1995), the Modified Rake DLL (MRDLL) (Laxton and DeVilbiss, 1997) and the Vision correlator (Fenton and Jones, 2005). In spite of the success of these techniques, they are receiver-dependent, which means that the users have no direct access to their technologies. Moreover, for short delay multipath the reflected signal is highly correlated to the direct LOS signal. As a result the reflected signal will be estimated as a part of the LOS signal.

Mitigation in the final measurements domain (carrier/code observables) is a result of the large amount of residuals from mitigation in the antenna/receiver domain. Raquet and Lachapelle, (1996) used a multi-antenna array to mitigate the multipath error GPS reference station. Han and Rizos, (1997) were the first to propose the use of finite impulse response (FIR) filters to extract or eliminate multipath. However, this technique has certain limitations because signals (i.e.: crustal deformation) that fall into the same frequency band will be removed. A more effective technique, based on the use of an adaptive filter to extract and eliminate multipath, was suggested by Linlin et al., (2000), Lee, (2008). Since GPS observation noise tends to change with time, it was determined more appropriate to use an adaptive filter rather than a fixed filter for the purpose of multipath mitigation. The implementation of such technique is dependent on the selection of an appropriate value for the step-size parameter and the filter length. Zhang and Bartone, (2004) developed a multipath mitigation technique based on the multipath frequency spectrum analysis. They used code minus carrier to model multipath errors and identify window size before the error was transformed into the frequency domain using the Fast Fourier Transform (FFT). In the Fourier coefficients domain, the authors mitigated the multipath error based on the estimated multipath frequency.

The reconstruction stage uses the Inverse Fast Fourier Transform (IFFT) to compute the multipath error-reduced code-phase measurements. This technique effectively reduces code multipath error, particularly in the static mode, where the multipath fading frequency is well predicted and the fading frequency ranges from zero to 1 Hz. However, more investigation is required to apply this correction in kinematic mode given the rapid change in multipath frequency.

Wavelets are used extensively as an alternative to FFT analysis because their elements are essentially waveforms indexed by three parameters: position, scale and frequency (Wang et al., 2009; Zohng et al., 2008; Aram et al., 2007; Zhang et al., 2005; Souza and Monico, 2004; Ogaja et al., 2003). This is what produces such strong localized time–frequency properties, which allow the wavelets the ability to provide an accurate location of the transient component in the signal while retaining information about the fundamental frequency. Therefore, wavelet transform offers advantages over the frequency domain analysis (Fourier analysis) and the time domain analysis (Kalman filter). Most of the research conducted on wavelet multipath mitigation uses wavelet transform on its own or combined with other techniques to mitigate high-frequency multipath error. Dammalage et al., (2009) used biorthogonal wavelets to de-noise code measurements for DGPS applications and reached a 60% error reduction. Ogaja and Satirapod, (2007) applied the Symlet base function at the fourth scale decomposition level to detect and separate high-frequency multipath errors from receiver noise when using high-rate (1-Hz) GPS data. (Souza and Monico, 2004) investigated the use of both Symlet and Daubechies base functions to reduce the high-frequency multipath in GPS relative positioning. They tested both the hard and soft threshold along with the median threshold estimator and concluded that Symlet12 along with the hard threshold performed the best and achieved a 30% error reduction. Satirapod and Rizos, (2005) used wavelets to mitigate multipath at permanent stations. The use of wavelets as a de-noising tool for processing and mitigating multipath error proved to be an effective tool for high-frequency multipath mitigation. In contrast, de-noising techniques cannot remove this type of error in medium to low-frequency multipath components. As a result, wavelets should be used differently according to the type of errors being mitigated. Chapter Four presents the various techniques that have been developed in this research thesis to deal with low to high-frequency multipath errors.

2.3.2 Ionospheric and Tropospheric Error

The ionosphere is the top layer of the atmosphere, containing ionized gasses and free electrons, at approximately 70-1000 km above the Earth's surface. The UV rays from the sun breaks up the molecules into ions and free electrons. The ionosphere is a dispersive medium with respect to radio waves and affects GPS signals by modifying their speed with respect to the speed of light in a vacuum. As a result, GPS code measurements are delayed and carrier phases are advanced (Hofmann-Wellenhof et al., 2001).

The ionospheric delay is a function to the total electron content (TEC) in a tube of 1 m^2 cross section along the propagation path., and the frequency of the propagated signal. The TEC depends on time, season and geographic location, with major influencing factors being the solar activity and the geomagnetic field (Klobuchar, 1991). The electron density level reaches a daily minimum around midnight at local time and maximum in early afternoon. The rate of ionisation in a global sense is a function of the 11-year solar cycle activity (Klobuchar, 1996), which corresponds to a peak in the solar flare activities known as the solar cycle peak. The TEC values have been observed to increase by a factor of three during a solar maximum versus a solar minimum (Klobuchar et al., 1995). In addition to the large-scale global increase in the absolute value of TEC during solar maximum, an increase in the frequency and magnitude of magnetic storms accompanies the enhanced solar flare activity (Skone, 1998). The current solar maximum occurred during the year 2012-2013. The data set used in this thesis is collected between 2007 and 2012, which means there is expected a strong ionospheric signature in the data at least for the data collected in 2012.

The path delay for a satellite at zenith typically varies from about 1 m at night to 5–15 m during late afternoon. At low elevation angles the propagation path through the ionosphere is much longer, so the corresponding delays can increase to several meters at night and as much as 50 m during the day (Grewal et al., 2007).

As a dispersive medium, it is possible to compute the ionospheric influence on the GPS signal by combining L1 and L2 frequency to remove most of the ionospheric error (99% under normal atmospheric conditions (Brunner and Gu, 1991)). However, this requires a dual-frequency receiver to track both L1 and L2 frequencies. In the case of single-frequency receivers, ionospheric error is either neglected or reduced using models (Souza and Monico, 2007).

Many models based on GPS observations have been proposed. They generally fall into two main categories: 2-D techniques and tomography technique. The oldest and simplest technique that models the ionosphere in 2-D is the broadcast model (Klobuchar, 1986). Eight coefficients representing this model are transmitted as a part of the navigation message to recover only 50% of the ionospheric error (Klobuchar, 1987). The grid model and polynomial function model (Komjathy, 1997) are two types of ionosphere modeling that estimate the Total Electron Content (TEC) at the receiver position by interpolation. The drawback to this approach for modeling ionosphere error (2-D approach) is that all ionospheric delays are mapped to a single spherical plane. This means that all the models are two-dimensional. As a result, alternative approaches using tomographic techniques have been proposed by many authors to overcome the limitations of 2-D models, such as (Hansen et al., 1997; Hernandez-Pajares et al., 1999; Mitchell and Spencer, 2003).

The troposphere is the portion of the atmosphere extending up to 60 km above the Earth's surface. The refractivity of the troposphere will cause the GPS signal travels through the troposphere to bend slightly. The change of the refractivity from free space to the troposphere causes the speed of the GPS signal to slow down, which causes a delay in the GPS signal. The tropospheric delay depends on the temperature, pressure, and humidity along the signal path through the troposphere.

The troposphere consists of dry and wet components. These components affect the propagation delay of the radio frequency signals quite differently. The dry component causes a delay around 2.3 m in the zenith direction which varies with local temperature and pressure. The dry component induced delay is quite constant and may vary only 1%

in a few hours. This dry zenith delay can be predicted very well using existing models. The wet component of the zenith delay is generally much smaller, between 1 and 80 cm at the zenith, and is very unpredictable. It may change by as much as 10% to 20% in a few hours (Spilker, 1994). Generally, tropospheric delay can be modelled very well. It was found that the contribution of the troposphere to the differential positioning error budget varies typically from 0.2 to 0.4 parts per million (ppm), after applying a model (Lachapelle, 2000).

The troposphere is a non-dispersive medium for GPS signals that affects both code and carrier at L1 and L2 frequency in the same way. The dry and wet constituents of troposphere affect GPS signal propagation differently, and each is modeled separately. The dry part of the troposphere is relatively stable but can depend on the latitude, season and altitude (Misra and Enge, 2006). The wet part of the troposphere is difficult to model since the water vapour density varies with the local weather and changes quickly. Fortunately, around 90% of the tropospheric delay is because of the dry component, which is more predictable.

Several tropospheric models have been developed to provide a priori values for dry and wet delays, as well as several mapping functions. Hopfield (1969) derived a dry delay model based on a refractivity model. Saastamoinen (1973) developed dry delay models based on a theoretical definition of hydrostatic delay and a hydrostatic equilibrium assumption. Mendes (1999) compared different tropospheric models for both dry and wet components and concluded that the Saastamoinen model performed better than other hydrostatic models in modeling both the dry and wet components of the troposphere (Mendes, 1999). He mentioned that the zenith dry and wet delay can be predicted from surface pressure measurements and the estimated accuracy of tropospheric delay can reach below 5 mm for the dry part and just a few centimetres in the wet part.

Another approach to tackle the challenges created by the ionosphere and troposphere is to filter these errors in the frequency domain. Ionospheric error is characterized as a low-frequency, long term trend within the frequency domain. Although of a smaller magnitude, the tropospheric delay occurs because the wet component can be characterized as short-term variations (high-frequency). Mitigation of the ionospheric and tropospheric errors in the frequency domain using Multi-Resolution (MR) spectral analysis is a new and promising area of research. (Souza and Monico, 2007) used the wavelets multi-resolution analysis to mitigate short and medium ionospheric scales affecting rapid static relative positioning in double difference (DD) measurements. They used 30 minutes of the DD measurements at 15-second intervals for three baselines (52, 115, 430 km). The data was processed at different times of the day, including when the ionospheric effects had more significant variations and then they decomposed the double difference signal up to level six using multi-resolution analysis. They applied the hard threshold function and the universal threshold methods to de-noise the signal by modifying the wavelet coefficient. These two techniques are used to de-noise the coefficients at each level of decomposition. Their method achieved promising results comparable to those computed by dual-frequency receivers, and, the resulting horizontal accuracy did not exceed 0.5 m in all scenarios.

2.3.3 Cycle Slips

A cycle slip is a sudden jump in the carrier phase observables by an integer number of cycles. Slips are caused when there is a loss of lock in the phase lock loops, which can be caused by signal blockage or high troposphere activities. Cycle slips occur between two epochs if the satellite signal cannot reach the antenna. The initial step in cycle slip detection and correction consists of setting up a test function (slowly time varying functions) that is a combination of code and/or phase measurements at single receiver or between two receivers. Cycle slip is seen as a singularity in the GPS measurements, which needs to be detected and removed. At lower elevation angle, GPS signal travels a longer path in the atmospheric layers. This will increase the noise level and consequently reduced the Signal to Noise Ratio (SNR). Therefore, it is hard to detect the cycle slip correctly at lower elevation angles because of the low SNR and the multipath effect is more dominant. Signals at lower elevation angles are contaminated with a lot of noise, which can be seen as successive jumps and get conflicted with real cycle slip jumps as a result more false cycle slip will be encountered. (Collin and Warnant, 1995)

Over the past decade, a number of methods have been developed to detect and repair cycle slips. Conventional approaches include the use of time differencing, low-degree polynomial fitting, and Kalman filtering. For instance, in the BERNESE software (Beutler et al., 2006) few minutes of double difference phase observations are modelled by a polynomial functions of low degree and cycle-slips are searched in the residuals of this polynomial interpolation. These methods require user intervention for input parameters tuning or to introduce additional carrier phase ambiguity parameter in the data processing. Some new methods have been come into view in the recent years, for example, Bisnath and Langley, (2000) developed an automated cycle-slip correction method by the combinations of Chebyshev polynomial and least-square scheme. Detecting the cycle slip in the frequency domain using wavelets is first presented by Collin and Warnant, (1995). They developed wavelet base function that is used to detect cycle slip in the details coefficients and the amplitude of the cycle slip is estimated from the coefficient. They did a comparison between Kalman filter and wavelets to detect and remove cycle slip from the phase-phase combination. The problem with using his proposed wavelet technique to detect cycle slip was that false successive jumps will be introduced in the coefficient domain when a lot of noise presents in the signal. Recently, an extension to this technique was made by Tinghua et al., (2006); Huang et al., (2006); Shi et al., (2005); Wang et al., (2007), Zheng et al., (2008) and Xiong et al., (2003) using integrated techniques such as neural network or other aiding statistical methods to determine the location and the amplitude of the cycle slip. However, they did not investigate the effect their techniques under sever noise and until the time this thesis written there is no wavelet technique can be used under sever noise.

Chapter five of this research thesis introduces a newly developed multi-scale singularity detection and estimation technique to identify cycle slip location and magnitude in a signal that is contaminated with noise. In that chapter, the property of a wavelet base function (e.g. compact support and smooth functions) is discussed and the selection procedure required to eliminate the low-order polynomial in the signal without data fitting is introduced. Furthermore, this chapter presents the performance of the proposed technique as tested over code minus carrier and Phase1 minus Phase2 GPS data and the simulated slip. Additionally, the ability of the proposed multi-scale technique to detect and estimate cycle slips over low signal to noise ratio is investigated.

Chapter Three: DGPS Error Behavior in the Multi-Resolution Domain

3.1 Field Experiments and Data Collection

This chapter describes GPS data collection campaigns that were conducted between 2007 and 2012 in order to investigate GPS error in the multi-resolution domain and develop the proper procedure for error mitigation. The focus of these experiments was to investigate correlated errors in the double difference measurement—a critical step for building the necessary procedures for mitigation. Three experiments were designed to cover baselines from 100 m to 50 km in different geometric conditions. The first experiment was established at the University of Calgary in November 2007 using NovAtel's GPS receivers. It was developed in a controlled environment where very short baselines were used to eliminate ionospheric and tropospheric errors and multipath remained the main source of error. The objective of this experiment was to assess multipath and noise errors that can be introduced in reference stations and then evaluate their characteristics within the multi-resolution domain.

To extend the baseline length from 100 m to 30 km, a second experiment is conducted at Nose Hill Park, in northwest Calgary. In this experiment two types of receivers were used: Trimble R8 dual-frequency GPS receivers along with an IGS station designated PRDS, near Priddis, southeast of Calgary. The data was collected at four GPS receivers simultaneously between January 9th and 11th 2008 at one-second intervals. To further extend the analysis to 50 km baseline GPS observations are collected from Cansel VRS network (Can-Net) from May 22nd to May 24th, 2012.

3.1.1 Description of Experiments

3.1.1.1 Experiment #1 (Short baseline at the University of Calgary)

This experiment is designed under control environment to isolate multipath from other error sources. The ultimate goal of this experiment is to distinguish multipath signature because of short and long delays and then transfer it to the multi-resolution domain. This experimental test was made at the University of Calgary using four NovAtel 600 dual-frequency antennas and four OM4 GPS receivers. The data was collected at both the Calgary Center for Innovative Technology (CCIT) and the Engineering building on the University of Calgary campus, shown in Figure 3-1. The equipment used at each station is listed in Table 3-1. The configuration at the reference station consisted of one receiver and antenna, which were used to collect data on the roof of the Engineering building. On the roof of the CCIT building, the three rover stations were arranged, as shown in Figure 3-1. The data collection started on November 11th, 2007 at 15:49:56 local time and repeated for three days at a rate of 1Hz data collection. The total number of epochs collected per day was 7200, which reflects two hours of data collection per day. The average temperature and pressure for the three days were 5^0C, 88 kPa for the first day, 7^0C, 86 kPa for the second day and 5^0C, 89 kPa for the third day. The baseline length between the reference station and the rover station was in the range of 100 m so as to guarantee the elimination of all the correlated errors such as ionosphere and troposphere errors when applying the double difference measurements (Hofmann, 2001). The only remaining errors should be the multipath, noise and the antenna phase center variation. To minimize antenna phase center error a NovAtel 600 antenna, which has a stable phase center variation, was used and both the reference and rover antennas were oriented to the north direction.

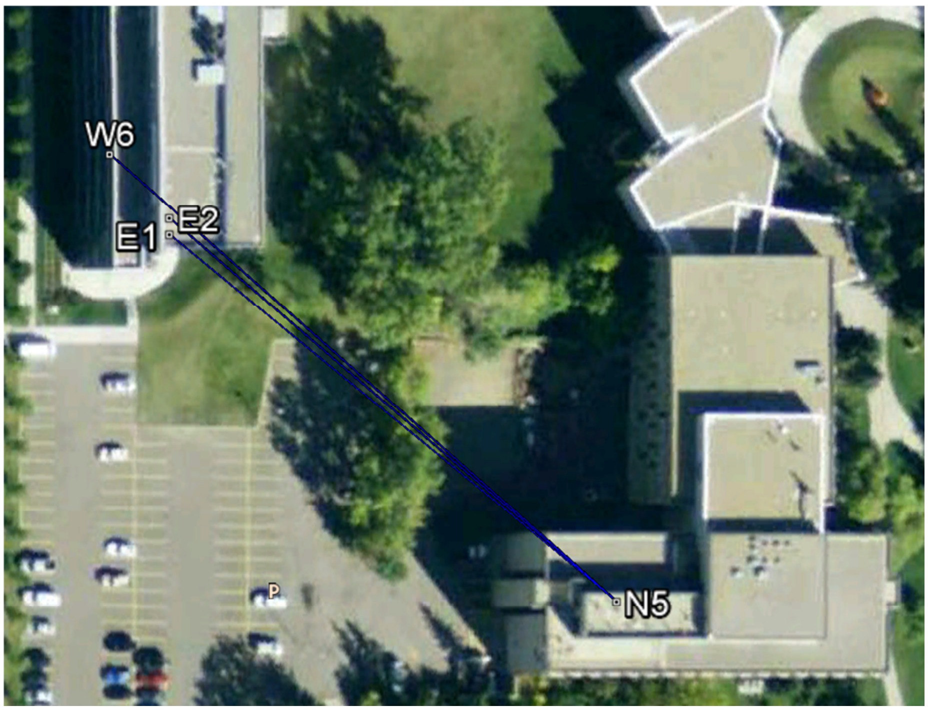

Figure 3-1: Experiment #1 Short baselines at university of Calgary

Table 3-1: Observation dates and equipment used for reference and rover measurements.

Station	**Receiver**	**Antenna**	**Observation**		**Duration (Hour)**
E1, E2, W6	Probak-DL-4-RT2 Novatel,	GPS-600-LB	11-Nov	Day01	2
			12-Nov	Day02	2
			13-Nov	Day03	2
N5	Probak-G2-DB9-RT2 Novatel,	GPS-600-LB	11-Nov	Day01	2
			12-Nov	Day02	2
			13-Nov	Day03	2

3.1.1.2 Experiment #2 (Short to medium baseline at Nose Hill park)

This experiment is designed to investigate the behavior of GPS errors in the multi-resolution domain. It was established using four GPS points set on Nose Hill Park in northwest Calgary. Nose Hill Park is a natural environment park, which provides ideal conditions for GPS observations. It allows a clear view of the sky without any obstructions. Those points, designated NH1, NH2, NH3, and NH4 were marked with an iron rebar drilled into the ground. All points were occupied by Trimble R8 dual-frequency GPS receivers mounted on tripods above the markers.

Figure 3-2: Experiment #2 Short baselines at Nose Hill Park

A fifth point, N5 used in Experiment #1, was chosen on the roof of the engineering building at the University of Calgary. In this station, the 600 dual-frequency antennas and

OEM4 GPS receivers that are used in the previous experiment are also used again in this experiment. Furthermore, an IGS station designated Prds, near Priddis south-east of Calgary, was used as an additional base station. The experiment was conducted over three days, on January 9 to 11 of 2008 from 09:22:46 to 11:22:46 local time. Each receiver was used at the same point on all days. All receivers were operated in static mode. The average temperature and pressure for the three days were -10^0C, 88 kPa for the first day, -5^0C, 87 kPa for the second day and -6^0C, 88 kPa for the third day.

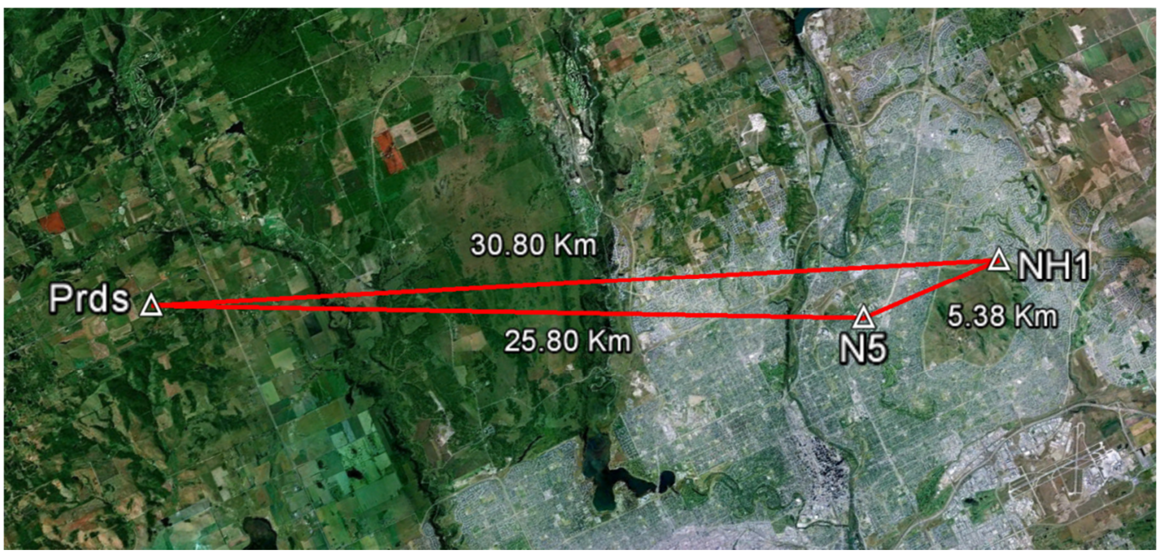

Figure 3-3: Experiment #2 longer baseline from NH1 to N5 and PRDS

The data collection started in January 9th, 2008 and collected in three different days at the rate of one-second data interval. The total number of epochs collected per day was 7200 epoch, which reflects two hours of data collection per day. The baseline length ranged from 200 meters between NH1 and NH3 to 30.80 kilometers between Prds and NH1. (Table 3-2) shows the receiver used at each station, the dates of data collection and duration.

Table 3-2: Observation dates and equipment used for data collection in experiment #02.

Receiver Info			Observation	Duration (Hour)
PtID	**Receiver Type**	**RecID**		
NH1	Trimble R8-2	4651126518	January 9th to 11th, 2008	2
NH2	Trimble R8-2	4629118870		2
NH3	Trimble R8-2	4629118867		2
NH4	Novatel Probak	1017201		2
N5	Novatel Probak	1017062		2
PRDS	AOA BENCHMARK ACT	1126		2

3.1.1.3 Experiment #3 (Can-Net Medium baseline)

To assess the proposed multi-resolution technique for mitigation of medium to low-frequency errors, GPS observations are collected from Cansel VRS network (Can-Net). The Canada Network (Can-Net) consists of 260 GPS receivers across Canada, deployed in 2005 by the Cansel Survey Equipment. Five Can-Net stations are used in this thesis (Figure 3-4) to cover baselines from 23 km to 50 km. Each Can-Net station consists of a Trimble Zephyr Geodetic 2 antenna and either Trimble NetR5 or Trimble NetR9 receiver (Table 3-3). The data is collected over three days for two hours per day at 1-second intervals beginning on May 22nd, 2012 at 19:00:00 local time. The average temperature and pressure for the three days at NCAL station were 8^0C, 87 kPa for the first day, 4^0C, 88 kPa for the second day and 6^0C, 89 kPa for the third day.

Table 3-3: Observation dates and equipment used for data collection in experiment #03.

STN Name	Receiver/ Antenna type			Observation	Duration (Hour)
	Code	Receiver	Antenna		
NCAL	Aref	TRIMBLE NETR9	Trimble Zephyr Geodetic 2	May 22nd – May 24th, 2012	2
AIR2	Ant1	TRIMBLE NETR9			2
COCH	Ant3	TRIMBLE NETR9			2
SBNK	Ant7	TRIMBLE NETR5			2
STRA	Ant8	TRIMBLE NETR5			2

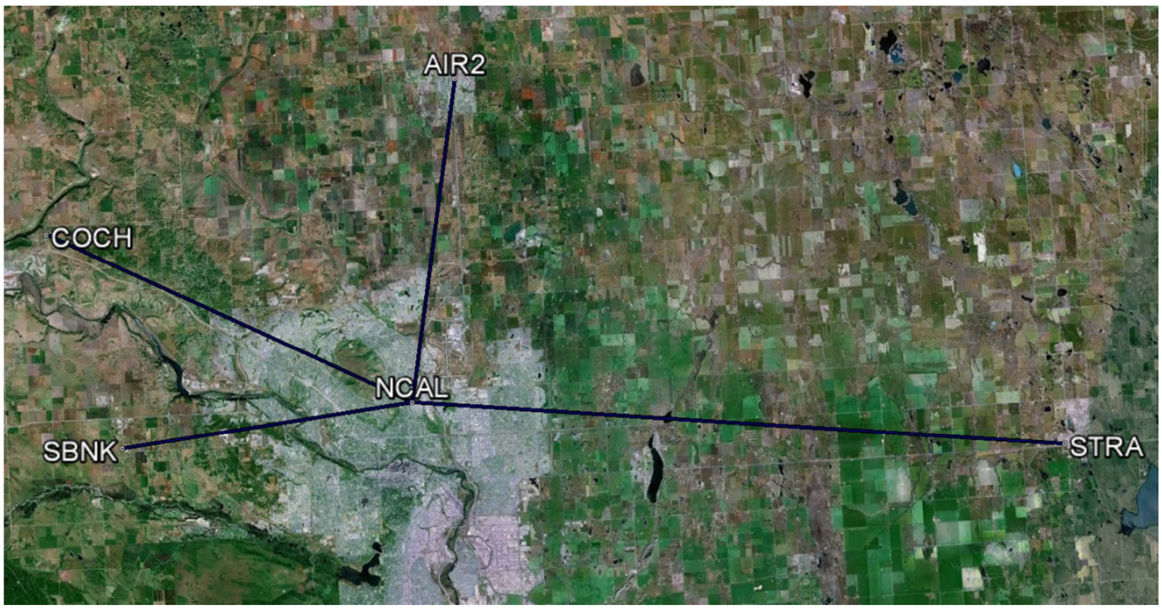

Figure 3-4: Experiment #3 Can-Net stations

3.1.2 Computation of Reference Coordinates

Data collected in the above three experiments were first processed using Bernese 4.2 (Hugentobler et al., 2001). Different techniques were used in Bernese software to compute the coordinates for the data collected in this thesis. The coordinates shown in Table 3-4 and Table 3-5 are computed using Bernese based on ionosphere-free fixed solution, 15° cut-off angle, IGS precise orbit. The standard deviation of the coordinates components for each station was below 1.7 mm. The model and mapping function for troposphere were Saastamoinen model and cosz mapping function as recommended by Tait et al., 2008. To verify these coordinates, Trimble Business Center (TBC) is used to compute the stations coordinate and compare it with Bernese software (Table 3-4). The solution achieved from TBC is fixed solution using L1 and L2. For long baselines TBC and Trimble VRS3NET are used to verify the stations coordinates (Table 3-5).

Table 3-4: Reference coordinates for experiment #1 and #2 computed by Bernese software Vs. TBC.

Station	Bernese(m)			TBC (mm)			Baseline (m)
	X	Y	Z	dx	dy	dz	
E1	-1641937.391	-3664810.674	4940009.495	10	0	1	92.474
E2	-1641936.566	-3664808.83	4940011.13	0	0	0	94.142
W6	-1641942.081	-3664797.661	4940017.63	2	2	3	108.118
NH01	-1640032.815	-3661204.911	4943430.698	0	0	0	0
N5	-1641890.232	-3664880.419	4939971.243	3	1	3	5,378.44
NH02	-1639847.077	-3661067.638	4943584.182	4	2	1	277.342
NH03	-1640076.321	-3661345.647	4943304.394	2	0	6	194.034
NH04	-1640204.237	-3661236.241	4943348.08	4	4	6	192.78
PRDS	-1659602.829	-3676725.754	4925493.591	6	12	18	30,750.78

Table 3-5: Reference coordinates for experiment #3 computed by Bernese software Vs. TBC and VRS3NET

STN	Bernese (m)			VRS3Net (mm)			TBC (mm)			BASELINE (m)
	X	Y	Z	dX	dY	dZ	dX	dY	dZ	
AIR2	-1625733.02	-3651749.87	4954880.70	8	5	4	8	12	17	28481
COCH	-1655668.87	-3646664.28	4949021.91	6	5	12	4	26	35	23127
NCAL	-1636751.26	-3666214.59	4940590.55	0	0	0	0	0	0	0
SBNK	-1656243.61	-3659412.64	4939287.01	6	9	11	6	19	26	20686
STRA	-1596478.89	-3688603.47	4937025.18	6	2	15	5	20	26	46215

The coordinates obtained in the previous tables (Table 3-4 and Table 3-5) are based on two hours GPS data at one second interval. As the baseline gets longer the ionospheric error becomes the most detrimental error for medium to long baseline carrier phase positioning. To demonstrate the impact of the ionospheric error for this experiment, the baseline between NCAL and STRA (46 km) is processed using Bernese and the double difference ionospheric error on L1 is shown on Figure 3-5). This figure shows that the ionospheric effect on the baseline for the period of the tow hours data collection was not active as it was in the range of ±3 cm.

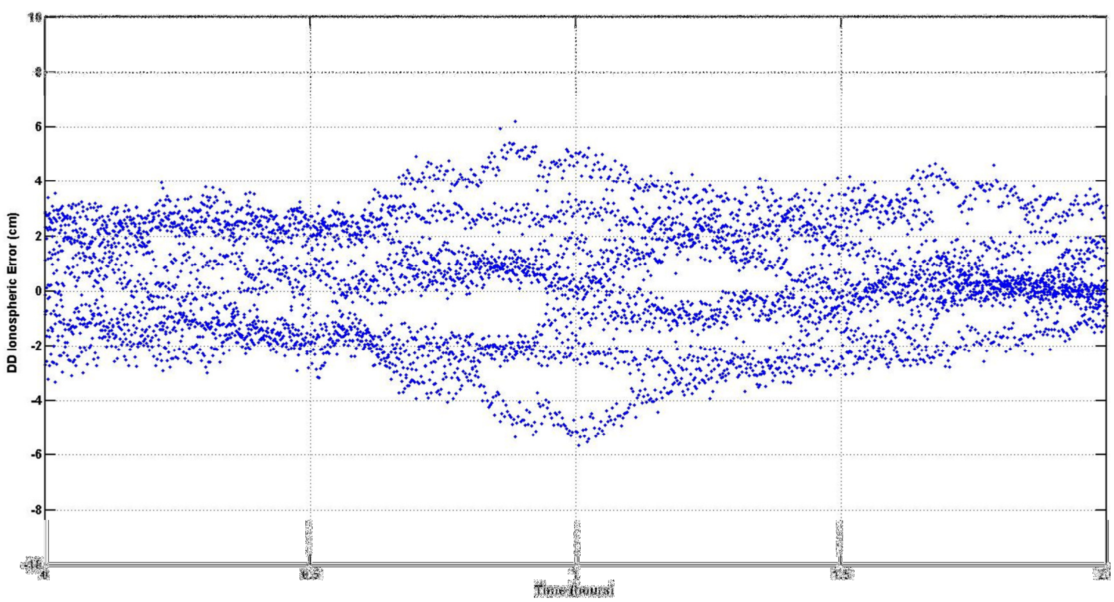

Figure 3-5: Double Difference Ionospheric error on L1 for 46 km baseline.

3.2 Batch processing implementation

A batch processing matalb toolbox is developed in this thesis to compute static differential GPS positioning based on multi-resolution correction. The structure of the data processing software is summarized in Figure 3-6.

This toolbox is dedicated to the post-processing mode using GPS data only, so that the observation and navigation data will be loaded after the compilation of the data collection. This implementation only accepts Receiver Independent Exchange Format (RINEX), a standard format widely accepted by the receiver manufactures to record the GPS navigation and measurement messages, for the observation data.

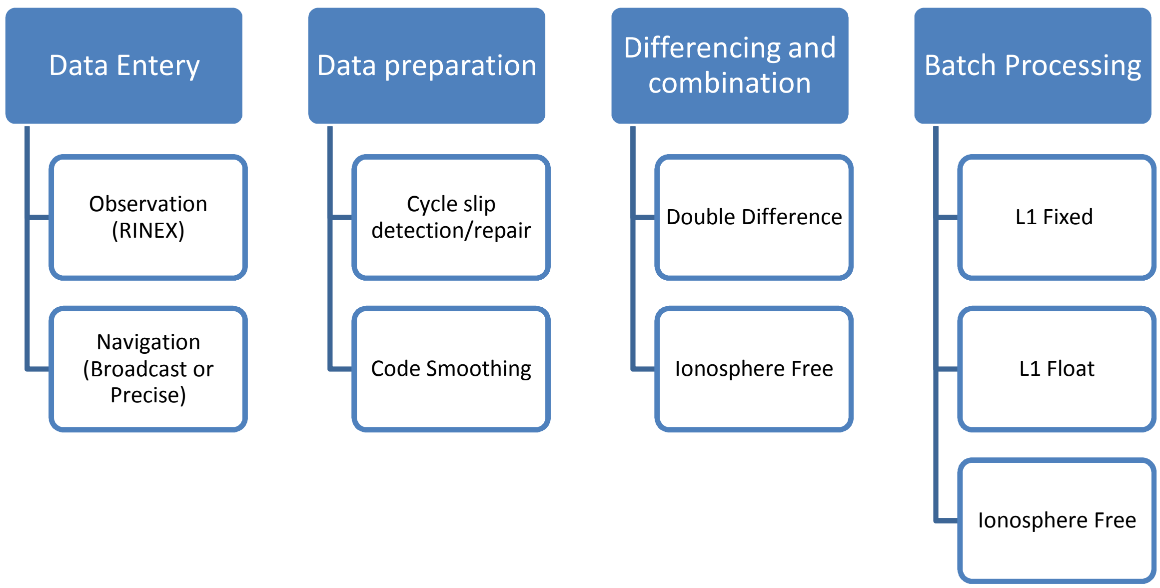

Figure 3-6: Structure of the implemented DGPS batch processing software

The data needed for the satellite positions and clock errors computation can be loaded to the toolbox using broadcast or a precise ephemeris. The broadcast ephemeris is available from the GPS, as a set of parameters sent to the user via the navigation message. The parameters are updated by the control center approximately every two hours and the accuracy of the computed coordinates is about 3 m. There are several types of precise ephemerides produced by several agencies in the world based on data from permanent GPS sites. Their accuracy ranges from about 0.2 m for predicted orbit to about 0.05 m for a final post-processed orbit. Precise ephemeris are usually distributed in Standard Product 3 Orbit Format (SP3 format), where the coordinates and satellite clock errors for all GPS satellites are listed at a 15-minute interval. In this implementation either navigation file or final precise ephemeris can be used in the processing based on the user selection. In case of precise orbits, a simple polynomial interpolation using an SP3 is used for computing the satellite positions as explained by Schenewerk (2003).

After the GPS observation and navigation data are loaded, the data collected will go through the preparation stage where cycle slip are detected and eliminated and the code measurements are smoothed. Cycle slips are detected and removed from the carrier phase measurements using the multi-scale singularity technique discussed in chapter five. Code smoothing is achieved using the multi-resolution real time technique explained in chapter 6.

After the data preparation, the double-differenced observables are formed. The double difference measurements are created using L1 only or IF measurements based on the user selection. Finally, a batch least-squares solution is obtained by processing all of the observations at once. At this step we are trying to estimate the final position parameters. This step tries to resolve integer numbers of ambiguity parameters. In this study, the LAMBDA method (Tiberius and De Jonge, 1995) is used as an ambiguity resolution procedure.

3.3 Correlated errors in the Multi-Resolution domain

3.3.1 Spectral analysis of double difference data

Converting the double difference residuals obtained from the batch processing toolbox to their frequency domain makes it possible to distinguish differences in GPS receiver noise behaviors and any systematic patterns (multipath and periodic signals) from the sites. In general, the receiver noise presents a white noise spectrum. Other systematic (or periodic) signals present a peak except for multipath, which presents a broad spectrum close to zero frequency. Power spectra in log–log scale describe a process in which the time domain behavior can be classified by the slope of the log–log spectra, also known as the spectral index. Several studies acknowledge noise in GPS data as a power-law process. Mao et al. (1999) noted that a combination of white noise and flicker noise has more power at low frequencies than high frequencies. Spectral indices of 0 and 1, respectively, appear to be the best model for noise characteristics in daily time series of GPS data. A study by Bock et al. (2000) also indicates that flicker noise is largely characteristic of GPS single-epoch solutions in the frequency band 0.01–10 MHz. Although the studies are for GPS time series residuals, it shows the same results for double difference residuals.

3.3.2 Short Baseline vs. Longer Baseline

Figure 3-7 and Figure 3-8 show the power of the double difference residuals for two baselines between NH1, NH2 and NCAL, STRA during the three days of data collection mentioned in experiments 2 and 3. Figure 3-7 shows the power spectral for short baselines (NH1-NH2), around 300 m, while Figure 3-8 shows the power spectral for longer baselines (NCAL-STRA) 46 km. All the double difference records indicate three noise types: white noise, flicker noise and low-frequency signals above the flicker noise level. White noise has equal power at all frequencies, which can be seen in Figure 3-7 and Figure 3-8 where the frequencies between 0.1 to 1 Hz have equal power at all frequencies. At this frequency window (0.1 Hz – 1 Hz) the slope of the log-log spectra is equal to 0, which indicates the presence of white noise. Flicker noise can be modeled by the slope of the log-log spectra (represented by a thick black line). Both figures show noise plus a signal, which has power above the noise level in the frequency band ~0.001–0.1 Hz indicative of longer period (low-frequency) systematic errors. These long period errors can be due to multipath errors or atmospheric errors, or both errors combined. In the case of Figure 3-7, a very short baseline is used to remove a spatial correlated error such as ionosphere. If it is assumed in this figure that differencing eliminates ionospheric error and modeling eliminates tropospheric error, the figure therefore shows the noise plus multipath error. In the case of Figure 3-8, multipath is mixed with other errors especially ionospheric errors. Therefore, it is important to isolate ionospheric error by modeling (and not spectrum filtering) before dealing with multipath, as it is hard to separate between both errors in the spectral domain. It can also be seen from both figures that the power of the low frequency in the longer baseline at Figure 3-8 is higher than the power at Figure 3-7 for small baseline, which can be due to the ionospheric error. In order to detect and quantify the existence of the periodic patterns (power peaks shown in the spectral content) in time sequence, spectrum analysis (short-time Fourier transform) is applied to the double difference data. With this approach, it is possible to examine changes in the spectral content with respect to the time scale.

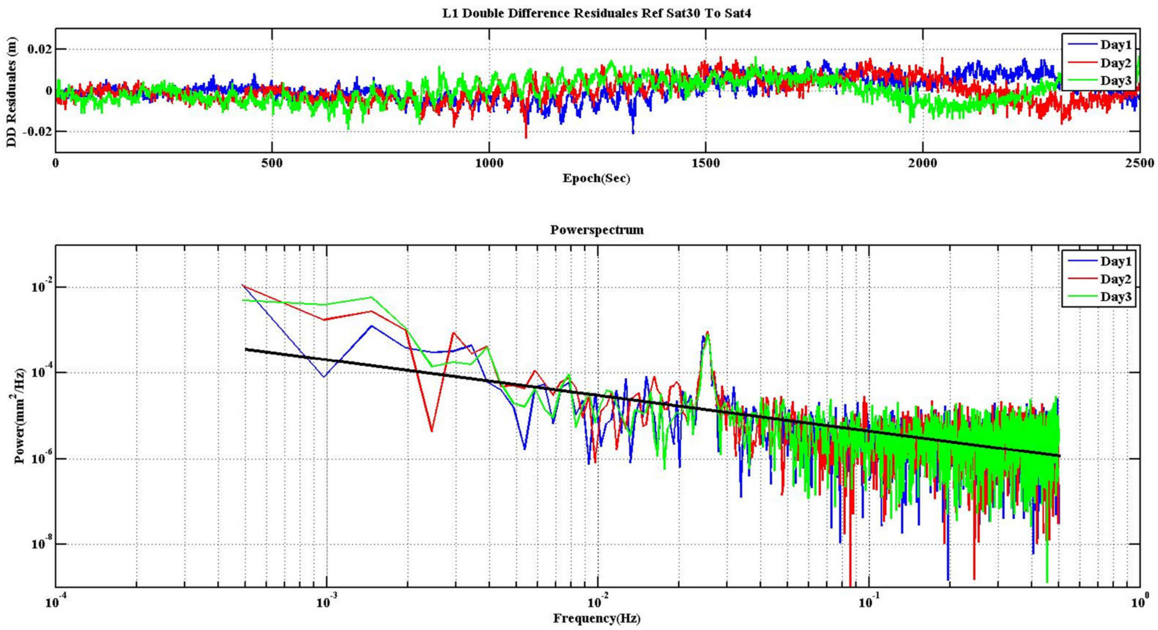

Figure 3-7: Power spectra of the double difference residuals for short baseline between NH1 and NH2 on the three days data collection.

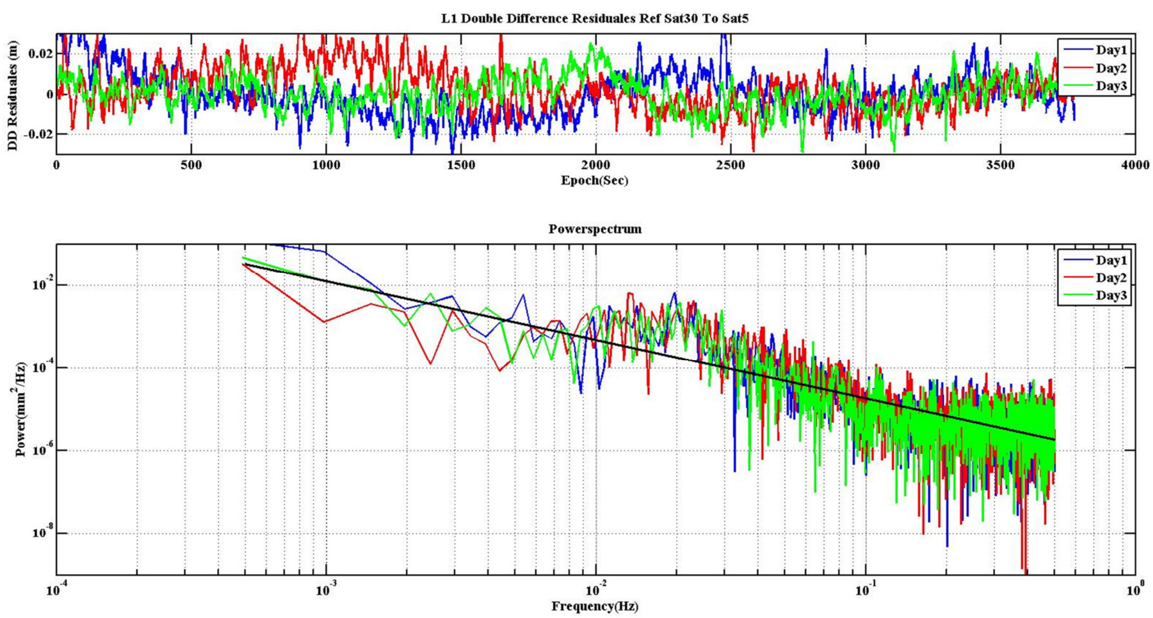

Figure 3-8: Power spectra of the double difference residuals for medium baseline between NCAL and STRA on the three days data collection.

Figure 3-9 shows the spectrogram analysis for the double difference data between satellite 30 and satellite 4 at baseline NH1-NH2 for the three days of analysis. In this spectrogram the frequency below 0.1 Hz is ignored since only white noise seems to dominate elsewhere. This figure shows the time in the horizontal axis, the frequency in the vertical axis the amplitude of a particular frequency at a particular time is represented by the intensity or colour of each point in the image. So if there is no frequency presents in the time series the intensity will be small and the color will go blue. While if there is a presence of a specific frequency at specific time the intensity colour for this time will change showing the availability of a frequency at that specific time.

It can be seen from this figure that the frequency content changes with time: something that a conventional Fourier analysis alone would not detect. In each of the images, there is a short time duration during which the ~0.025 Hz signal is strong. At no other period does this signal appear to dominate (as is the case with the global power spectra). In contrast, the low-frequency signals (<0.01 Hz) do exist during almost the entire period with some instances of intense power densities. Note the change in time axis from day to day. There is clear visual evidence of a time shift in the successive days of the occurrence of the ~0.025 Hz signal. This is at least an indicator that the effect is changing daily as a result of the change in GPS satellite constellation that affects the geometry between the satellites, antenna and the surrounding environment.

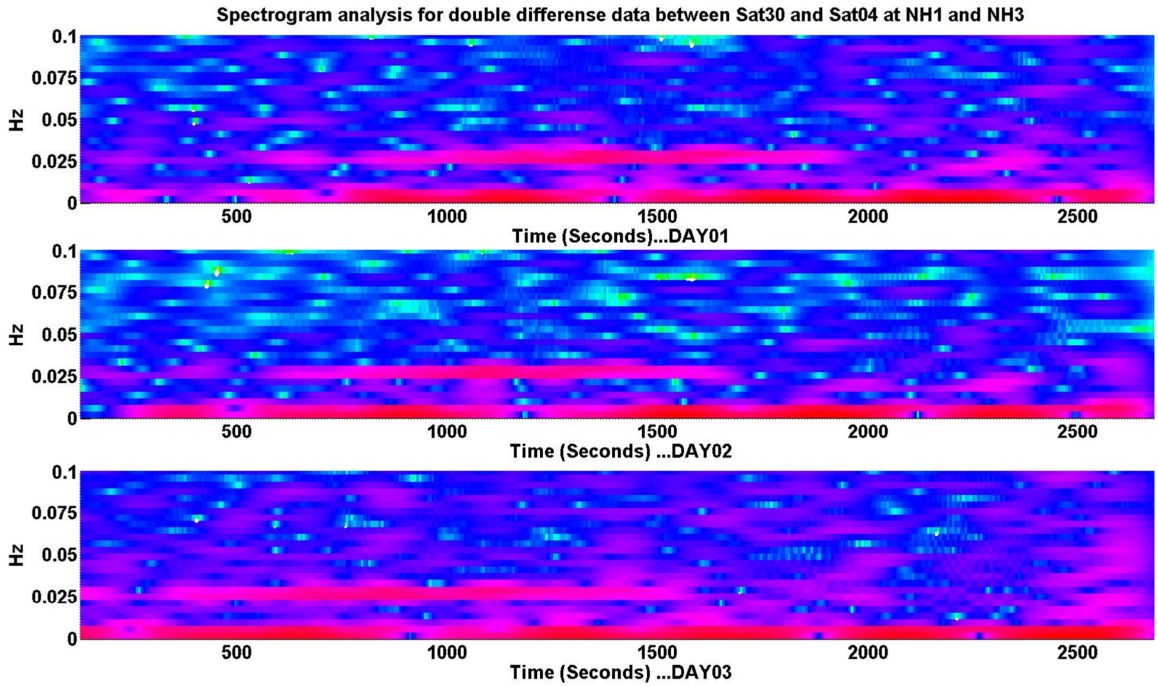

Figure 3-9: Spectrogram analysis for baseline NH1-NH2 Double Difference data during the three days of analysis.

3.3.3 Multipath identification

Based on the nearly exact repetition of GPS satellite geometry in the sky above a site every sidereal day (nominally 23 h: 56 m: 04 s), multipath error is highly correlated across subsequent days providing the same antenna and reflector environment (Ragheb et al., 2007). Three successive days of GPS observations are used in this thesis to identify multipath. The correlation coefficient was computed by using the following equation (Maybeck, 1994):

$$C_{XY} = \frac{E[(X - m_X)(Y - m_Y)]}{\sqrt{E[(X - m_X)^2]E[(Y - m_Y)^2]}} \quad \textbf{(3-1)}$$

Where, *E []* is the expectation operator, *X* is a state variable (double difference Data on Day1), *Y* is another state variable (double difference data on Day2), m_X is the mean of state variable *X*, and m_Y is the mean of state variable *Y*.

In this research thesis the correlation is not computed directly between the double difference data in successive days, instead wavelets are used to separate the double difference signal into twelve frequency bands (twelve level of decomposition). Each of these twelve levels of decomposition is subtracted from the original signal resulting in twelve modified versions of the original double difference signal. The reason for this isolation of each level of decomposition is to identify the level of decomposition that, when removed from the original signal, causes the most reduction in the correlation coefficient. This is a direct indication that a multipath signal exists at this level of decomposition.

Figure 3-10 and Figure 3-11 show the correlation reduction for the original signal when removing the syntheses signal at each level of decomposition from level 1 to 12. Figure 3-10 shows the correlation reduction for short baseline NH1-NH2 and Figure 3-11 show the correlation reduction for longer baseline NCAL-STRA. It can be seen from both figures (upper left side for cross correlation and lower left side for auto correlation) that level one and two do not change the correlation as they contain uncorrelated noise, while the levels that contain most of the multipath signal are levels three to six where the removal of these levels causes the correlation to reduce dramatically. It is also noticed that the double difference residual for the ionosphere-free data L3 (right side of the figure) gives better correlation values when compared to L1 double difference data (left side of the figure) . This is because the ionosphere-free linear combination removes the first order ionospheric error, which uncorrelated between days, leaves the multipath correlated errors untouched.

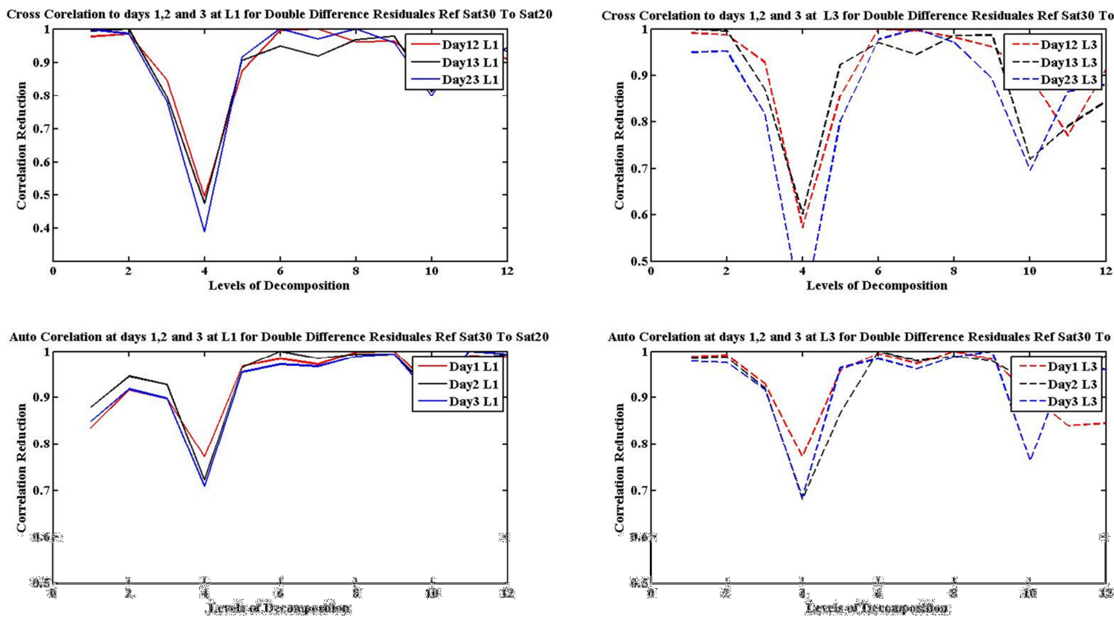

Figure 3-10: Correlation reduction at each level of decomposition for double difference data between satellite 30 and satellite 20 for baseline NH1-NH2.

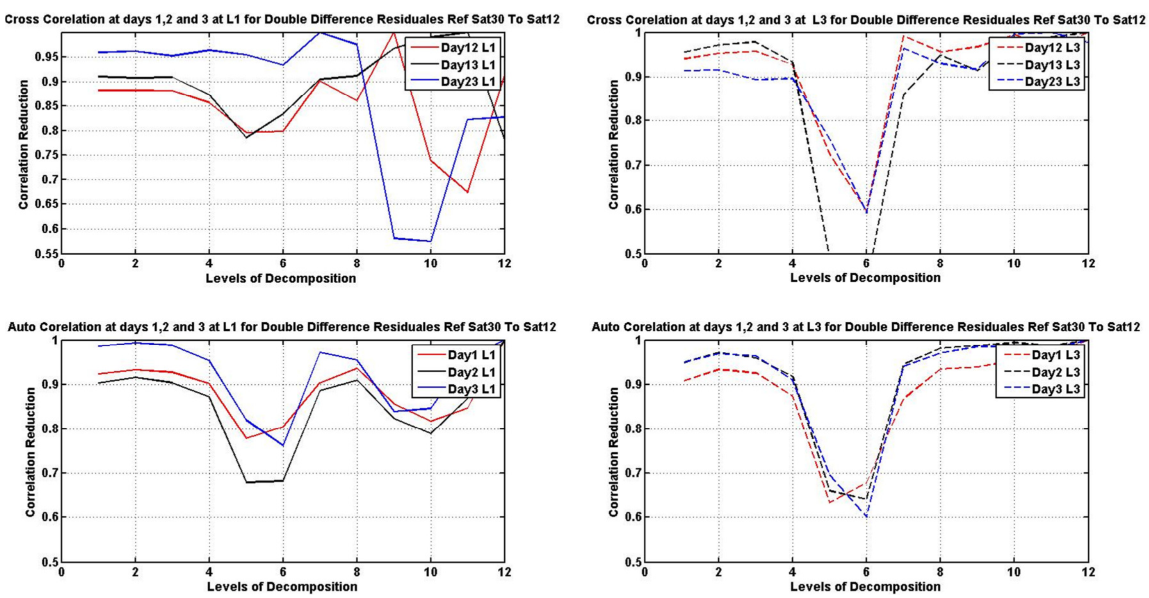

Figure 3-11: Correlation reduction at each level of decomposition for double difference data between satellite 30 and satellite 12 for baseline NCAL-STRA.

In this research thesis the spectral and correlation analysis at different levels of decomposition is used to justify the presence of multipath error and validate the removal of this error with the multi-resolution techniques that will be explained in the following chapter.

Chapter Four: Medium to High-frequency DGPS Error Reduction using De-Noising and De-Trending Procedures

Global positioning systems is known to create bias effects such as multipath, ionospheric and tropospheric delays that behave like low-frequency noise. Random measurements errors can also occur and these are typically characterized as high-frequency noise. The low-frequency nature of a multipath is what causes the largest error, which in carrier phase measurements can reach up to 5 cm. For a static base station it is required that both error components (low and high-frequency) are removed and not included in the static baseline processing. As discussed in Chapter 2, many of the techniques discussed in the literature already used wavelets as a de-noising tool (Dammalage et al., 2009; Ogaja and Satirapod, 2007; Souza and Monico, 2004 and Satirapod and Rizos, 2005) but it is still not clear which wavelet parameters should be used with GPS double difference data to mitigate the medium to high-frequency errors (mainly multipath and uncorrelated ionospheric error). Moreover, there is no compartative analysis made using different wavelets thresholding estimators or techniques to mitigate the medium to high-frequency errors or the best wavelets denoising technique for GPS error mitigation.

This chapter will introduce two different multi-resolution techniques that can be used separately or combined to remove the low to high-frequency GPS errors. The first technique is applied using the wavelets as a de-noising tool to tackle the high-frequency errors in the double difference domain and to obtain a de-noised double difference signal that can be used in a positioning calculation. A detailed analysis is also made to choose the best wavelet base function and threshold technique estimator by comparing different wavelets parameters along with different thresholding techniques. The second technique discussed in this chapter uses the wavelets technique as a de-trending tool to tackle the low-frequency portion of the double differenced measurements.

The de-trended and the de-noised double differenced measurements will be used to compute an accurate positioning for the baselines described in Chapter 3.

4.1 Wavelets De-Noising

As mentioned in the chapter's introduction, double difference errors may have low (coarse-gain) and/or high frequency (fine-gain) fluctuations. Fortunately, the high-frequency aspect is relatively easy to remove if the proper de-noising threshold is applied. Multi-resolution analysis has been proven to be an important tool for eliminating noise in signals. The strong localization properties of the wavelets in time and frequency domain allow the wavelets to detect fine and coarse variations in the signal (Hubbard, 1998). A basic wavelet de-noising algorithm consists of three steps:

1) Decompose the noisy signal (double difference GPS signal) using a wavelets multi-resolution analysis of its details and approximations.
2) De-noise the details' wavelets coefficients, which contain the high-frequency portion of the signal.
3) Reconstruct the de-noised signal by applying the inverse wavelet transform to de-noised coefficients.

$$c_n^m = \left\langle S, \Phi_{m,n} \right\rangle = \sum_{l \in Z} h_l \left\langle S, \Phi_{m-1,2n+1} \right\rangle = \sum_{l \in Z} h_{l-2n} c_l^{(m-1)} \quad \textbf{(4-1)}$$

$$d_n^m = \left\langle S, \psi_{m,n} \right\rangle = \sum_{l \in Z} g_l \left\langle S, \psi_{m-1,2n+1} \right\rangle = \sum_{l \in Z} g_{l-2n} c_l^{m-1} \quad \textbf{(4-2)}$$

As described in Chapter 2, the double differenced signal (*S*) can be represented by approximation coefficients c_n^m and d_n^m detailed part (see Equation (4-1) and (4-2)). In the Equation (4-2) the double difference GPS signal is decomposed into two-sets of coefficients: low-frequency (approximation d_n^m) and higher frequency (details c_n^m) by convolving the input signal with low-pass (L) and high-pass (H) filters, respectively. One of the main advantages of wavelets is the presence of various parameters that can be controlled to help in the classification and separation of different types of signals with different frequencies. These parameters must be selected to match the properties of the GPS double difference error. Four different parameters are used in this research to create several combinations to detect the optimum combination in reducing the high-frequency GPS errors. These parameters are:

1) Wavelet base function and vanishing moment
2) Level of decomposition
3) Threshold type
4) Threshold estimator

All the possible combinations among the factors are investigated to ensure that the use of the wavelet transform technique is efficient for GPS error mitigation. These parameters will be described in the next subsections.

4.1.1 Wavelet base function and Vanishing moment:

The main criterion for selecting the wavelet base function is that the base function matches the shape of the main error, which in this case multipath. Ray (2000) demonstrated the pattern of the carrier phase multipath error in GPS signals, which can take one of two shapes (Figure 4-1). The multipath error with a small magnitude causes a sinusoidal pattern, while the multipath error with a high magnitude causes a saw-tooth pattern. Therefore, for the purposes of this investigation, the wavelet base function that can match both sinusoidal and saw-tooth pattern will be used.

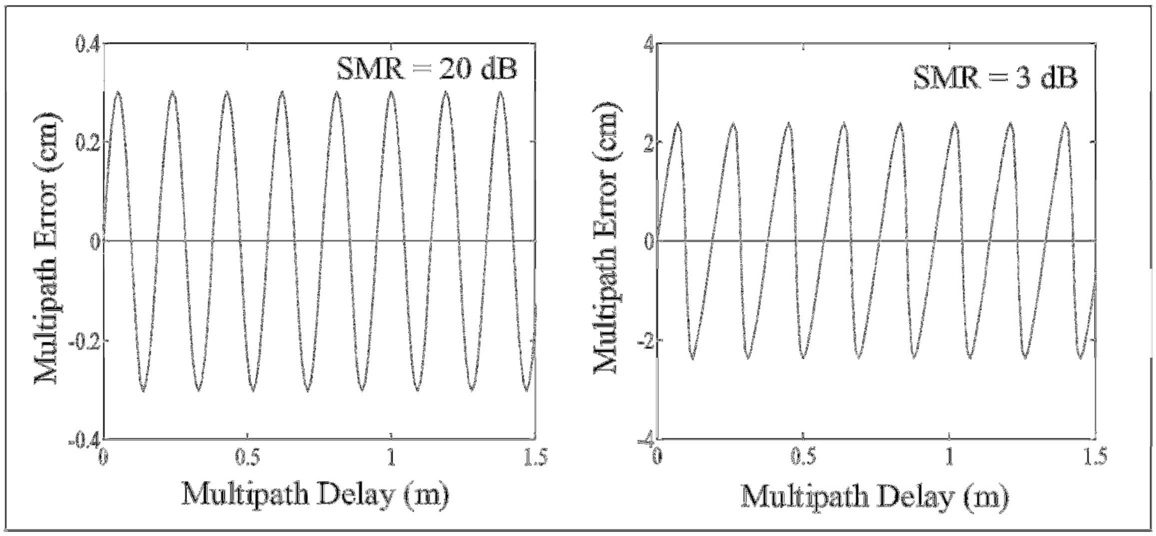

Figure 4-1: Carrier phase multipath error pattern for short multipath delays due to a reflected signal of SMR equal to a) 20 dB and b) 3 dB (after Ray, 2000)

There are a number of wavelet base functions (including Haar, Daubechies, Coiflets, Symlet, Biorthogonal) that differ in the way their scaling and wavelets functions are defined. Wavelets are classified into a family by the number of vanishing moments, *N*. This number, which is weakly linked to the number of oscillations (the more vanishing moments wavelets has, the more it oscillates), determines what a wavelet does not extract, that is, what it recognizes. Wavelets with one vanishing moment do not recognize a linear function. Therefore, two vanishing moments make wavelets blind to quadratic functions as well as three vanishing moments to cubic functions, and so on. Wavelets with many vanishing moments also yield small coefficients when used to analyze a low frequency (Hubbard 1998). Within each family of wavelets there are wavelet subclasses distinguished by the number of coefficients and by the level of iterations. The filter lengths and the number of vanishing moments for four different wavelet families are tabulated in Table 4-1. For a rapid decomposition and reconstruction of a signal in the wavelet transform domain, orthogonal wavelets must be selected. The wavelets functions shown in Table 4-1 are candidates to detect high-frequency error in GPS signals as they can match the sinusoidal and saw-tooth pattern shown in Figure 4-1.

Table 4-1: Wavelets families and their properties.

Wavelets Family	Filter length	Number of Vanishing moments	Orthogonal
Daubechies	2M	M	yes
Symlets	2M	M	yes
Coiflets	6M	2M-1	yes
Biorthogonal	max(2Nr,2Nd)+2	2M-1/2M	No

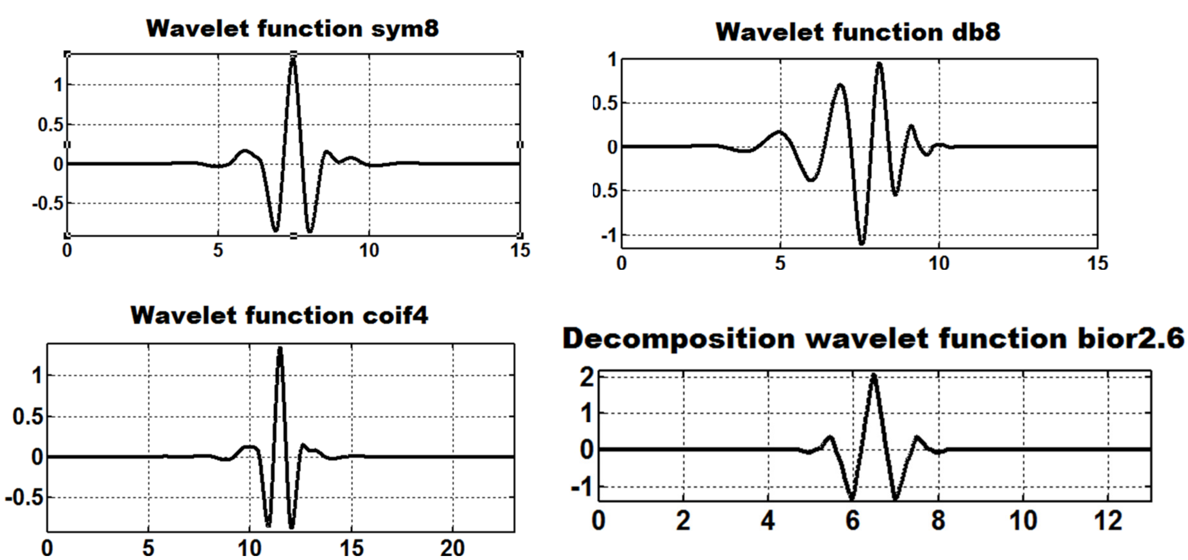

Figure 4-2: Candidate wavelet base function at different vanishing moments.

4.1.2 Level of decomposition:

Multi-Resolution Analysis (MRA), as introduced in Chapter 2, is used in the construction of orthogonal wavelet bases and the fast decomposition of a signal into independent frequency bands through a nested sequence. MRA builds a pyramidal structure that requires an iterative application of scaling or levels of decomposition and wavelets functions to lowpass (LP) and highpass (HP) filters, respectively (Figure 4-3). These filters initially act on the entire signal band at a high frequency (lower scale values) and gradually reduce the signal band at each stage. As a result of this structure, the signal is decomposed into an approximation c_n^m and a detailed d_n^m part. Decomposition into high level is required to capture the low-frequency multipath.

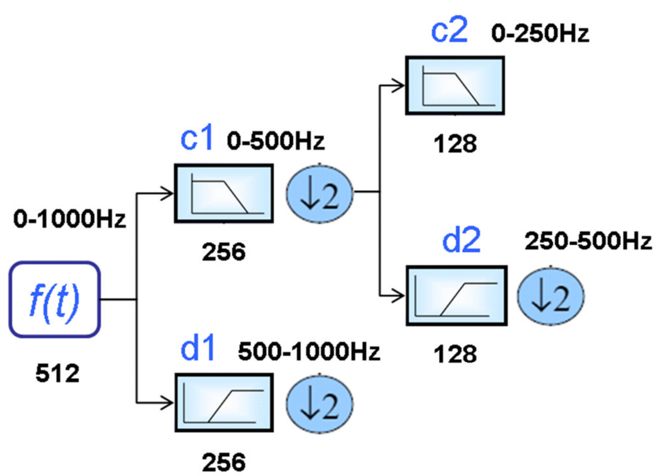

Figure 4-3: Block diagram of the one-dimensional wavelets decomposition (Elhabiby, 2007)

In this chapter an investigation is conducted on the level of decomposition that captures most of the correlated errors between levels 1 to 12 on 1Hz GPS double difference data.

4.1.3 Threshold type:

The wavelet thresholding technique was developed primarily for removing noise and outliers, compression, and pattern recognition of the signal before wavelets reconstruction. In this analysis, two thresholding methods are presented: hard and soft thresholding. The former is for matrix compression and the latter for de-noising signals.

Hard thresholding is like a gate. If a value is below a certain thresholding value, it is set to zero (Figure 4-4). The same algorithm is used for the compression of matrices. Wavelets coefficients (given as an absolute value) larger than a certain specified threshold δ should be included in the reconstruction. The reconstructed function can be expressed as follows (Ogden, 1997):

$$\hat{q}(t) = \sum_{m}\sum_{n} I_{\{|d_n^m|>\delta\}} d_n^m \psi_{m,n} \qquad \textbf{(4-3)}$$

Where $I_{\{|d_n^m|>\delta\}}$ is the indicator function of this set of wavelets coefficients for thresholding.

This function represents a “keep or kill” wavelet reconstruction technique in that it assumes a value of one for the coefficients required in the reconstruction process and zero for the coefficients that should be removed. Hard thresholding is a type of nonlinear operator on the wavelet coefficients vector and leads to a resultant vector of the estimated coefficients $\hat{d}_n^m$, which can be involved in the reconstruction process, as follows:

$$\hat{d}_n^m = \begin{cases} d_n^m, if \mid d_n^m \mid \geq \delta \\ 0, otherwise \end{cases} \tag{4-4}$$

Soft thresholding is defined as

$$\hat{d}_n^m = \begin{cases} d_n^m - \delta', if \mid d_n^m \mid \geq \delta' \\ 0, \quad if \mid d_n^m \mid \leq \delta' \\ d_n^m - \delta', if \mid d_n^m \mid < \delta' \end{cases} \tag{4-5}$$

Based on Figure 4-4, it is clear that soft thresholding is generally linear (straight line with slope to be determined). The input for this figure is wavelets coefficients d_n^m before thresholding and the output is the estimated coefficients $\hat{d}_n^m$ after thresholding. Soft thresholding is used in de-noising signals hidden in background noise. The main objective is to attenuate the noise while amplifying the signal. The thresholding δ' value is computed using a threshold estimator (Ogden, 1997).

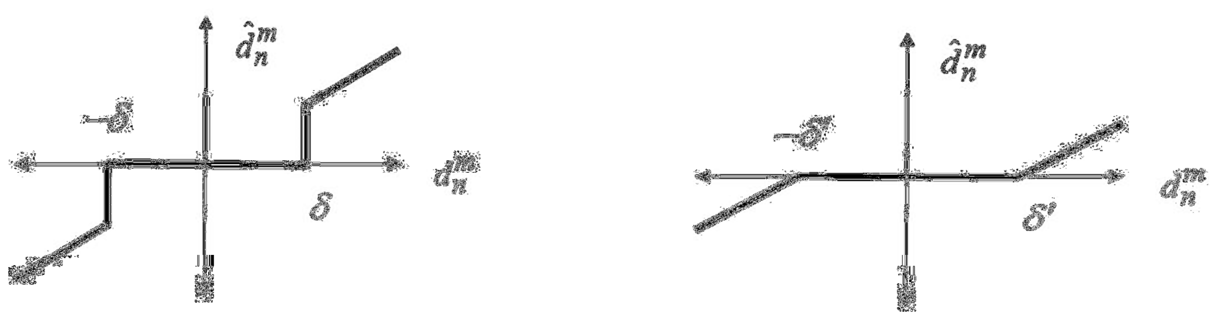

Figure 4-4. Hard threshold (left) and soft threshold (right)

4.1.4 Threshold estimator:

Choosing a threshold value in the threshold function is a key challenge for in-signal de-noising. The reason for this is that the threshold estimator, which controls the flow of noise in the signal, can have a very small threshold value. This can cause some noise to be saved after the signal de-noising. Alternatively, a larger thresholding value will cause distortion. Therefore, it is crucial to select the proper threshold value while performing the de-noising technique. Donoho and Johnstone (1994) presented several proposals about the choice of the threshold estimators. In this thesis four threshold estimators are investigated for GPS error mitigation in the double difference domain, these estimators are:

1- Stein's unbiased maximum likelihood threshold estimator (Rigrsure)

This estimator uses the SURE threshold, which was established using Stein's unbiased maximum likelihood estimator. For each threshold value the corresponding value-at-risk is founded and then the threshold that reduces the risk threshold values is chosen based on the following algorithms:

$$P = [P_0, P_1, \dots . P_{N-1}], P_0 < P_1 < \cdots < P_{N-1} \quad \textbf{(4-6)}$$

The elements of P are square of the wavelets coefficients, which is from a small to large order. The risk algorithm is:

$$R(K) = \left[N - 2K - (N-K)P_k + \sum_{I=1}^{k} P_I \right] / N \quad \textbf{(4-7)}$$

Where k=0, 1,…, N-1. According to the resulting risk curve *R(k),* the minimum corresponding value to be K_{min} and the threshold is defined as:

$$\lambda = \sigma\sqrt{PK_{min}} \quad \textbf{(4-8)}$$

2- Median threshold estimator

This threshold value is based on the following wavelet transform:

$$\lambda = \sigma\sqrt{2logN} \qquad \textbf{(4-9)}$$

Where *N* is the signal length, σ is the noise standard deviation, which can be evaluated by the following equation,

$$\sigma = \frac{median(|d_j(k)|)}{0.6745} \qquad \textbf{(4-10)}$$

Where $d_j(k)$, is the high-frequency coefficient after the Wavelets Decomposition, $median$ is calculating intermediate values of operation.

3- Heuristic threshold estimator

The heuristic threshold estimator synthesizes the two former thresholds. What is chosen is an optimal prediction variable threshold. When the ratio of the signal and noise is small, a fixed threshold is adopted; otherwise, using Rigrsure norm.

4- Minimum Maximum (Minimax) threshold estimator

The Minimax threshold estimator is a thresholding method developed by Donoho and Johnstone, (1994) that is based on minimizing the *l2* risk (Equation(4-11)). The minimax algorithm uses a fixed threshold chosen to yield minimax performance for mean square error against an ideal procedure. The minimax principle is used in statistics to design estimators. It is the option that realizes the minimum, over a given set of functions, of the maximum mean square error.

$$
\begin{aligned}
&\Lambda_n^* \le 2\log n + 1 \quad \textit{and} \lim_{n\to\infty} \Lambda_n^* = 2\log n \\
&\lambda_n^* \equiv \textit{the largest } \lambda \textit{ attaining } \Lambda_n^* \\
&\lambda_n^* \le \sqrt{2\log n} \quad \textit{and} \lim_{n\to\infty} \lambda_n^* = \sqrt{2\log n}
\end{aligned}
\qquad \textbf{(4-11)}
$$

4.2 Wavelet De-Trending

The low-frequency portion of multipath is what creates the largest error, which in carrier phase measurement can reach up to 5 cm. Wavelets are used to remove the high-frequency oscillation from the investigated signal by changing the detail coefficient values of the wavelet decomposition to zero and reconstructing the signal using the modified wavelet coefficients. If the details associated with noise cannot be determined properly, either useful signals will be missed or a reconstructed signal may contain severe noise. In the case of a double difference signal, multipath is distributed at varying levels of decomposition. In order to reach the low-frequency multipath error, a higher level of decomposition is required (Figure 4-5). Thresholding the details coefficients at a level where the largest low-frequency multipath error is suspected will reduce the overall error. But to reach that error other unwanted frequencies are induced in the reconstructed signal at the lower levels of decomposition.

A new approach based on a wavelet de-trending technique is introduced to remove the long wavelength carrier phase multipath error in the measurements domain. In order to mitigate multipath, GPS double difference observables are introduced to an adaptive wavelets analysis procedure based on high and low pass filter decomposition with varying levels of resolution (El-Ghazouly et al., 2008a).

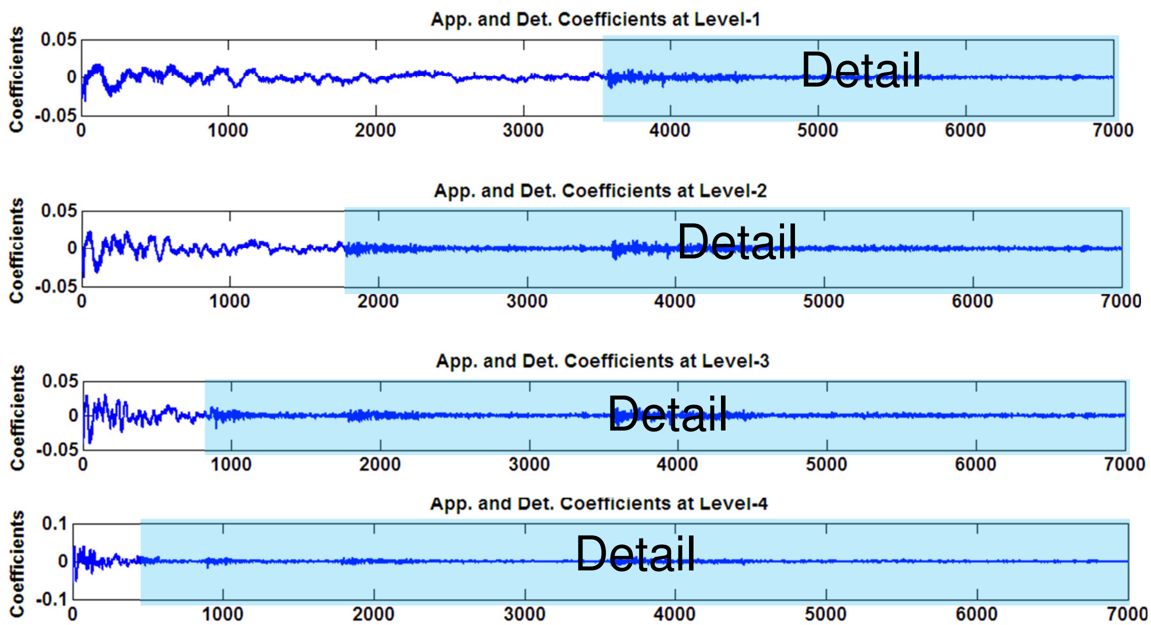

Figure 4-5: Approximation and details coefficients at different level of decomposition.

The procedure is applied after cycle slips detection and repair. Based on the previous knowledge and facts that the largest errors are caused by the low-frequency multipath, wavelet transform approach is used to separate the multipath error at high levels of decomposition. The separated wavelet coefficients (approximation or high-level decomposition coefficients) are truncated using wavelets thresholding techniques before the reconstruction of the signal to acquire the true double difference carrier phase residuals out of the low-frequency multipath (El-Ghazouly, 2009).

4.3 Case Study of baseline range 100 m-50 km

Chapter 3 described the data collection methods in addition to the receiver and antenna type, receiver locations, data sampling, and duration used in this experiment. Table 4-2 summarizes the baselines used in the analysis and the number of double difference data for each baseline. The baselines are divided into two categories according to the baseline length. Category I contains short baselines where the length varies from 100 m to 5 km, and Category II covers longer baselines from 20 km to 50 km. The table also shows each baseline reference and rover station, the number of double differenced data computed in this baseline and the reference satellite used to compute the double difference data.

The total number of baselines in these data sets is 13 with seven baselines in Category I, and six baselines in Category II. In this research case study the double difference measurements are computed in L1 GPS signal and ionosphere-free linear combination. Data was collected over three days for approximately two hours for each baseline. It is worth mentioning that three successive days of GPS observations for each baseline were used in this thesis to identify correlated errors.

Table 4-2: Baselines and double difference data used in the thesis.

Category	Ref	Rover	Baseline (m)	No. of DDs.	Ref. Sat.
I	N5	E1	92.5	13	2
	N5	E2	94.1	13	2
	N5	W6	108.1	12	2
	NH1	NH2	277.3	13	30
	NH1	NH3	194.0	13	30
	NH1	NH4	192.8	13	30
	NH1	N05	5,378.4	11	30
II	NCAL	SBNK	20,686.2	7	28
	NCAL	AIR2	23,126.6	7	28
	N05	PRDS	25,756.3	7	17
	NCAL	COCH	28,481.2	7	17
	NH1	PRDS	30,750.8	6	30
	NCAL	STRA	46,215.2	6	28
	Total			128	

4.3.1 Wavelets multipath mitigation

I. Wavelet base function and vanishing moment

Thirty-seven wavelet base functions are used to decompose the double difference data into their details and approximation coefficients (Table 4-3). Each of the 128 double difference measurements mentioned in Table 4-2 is decomposed to their approximation and details at levels of decomposition from one to 12. The criteria for selecting the best wavelets base candidate are based on a correlation between days. This is explained in the following steps:

1) Compute the correlation for each baseline over the three days of data collection using Equation (4-12). There should be three reference correlation values for each baseline reflecting the correlation between Day1 and Day2, Day1 and Day3, and Day2 and Day3 for this baseline, which are C_{12}, C_{13} and C_{23}.

$$C_{XY} = \frac{E[(X - m_X)(Y - m_Y)]}{\sqrt{E[(X - m_X)^2]E[(Y - m_Y)^2]}} \qquad \textbf{(4-12)}$$

Where, *E []* is the expectation operator, *X* is a state variable (double difference data on day1), *Y* is another state variable (double difference data on Day2), m_X is the mean of state variable *X*, and m_Y is the mean of state variable *Y*.

2) Decompose each of the 128 double difference data for day one, two and three to approximation and details at Level one. The total number of double difference data in this step is calculated as: 128 double difference data x three days = 384 double difference data.

3) At this level of decomposition set the details coefficients to zero, this step will delete all the high-frequency data at this level.

4) Reconstruct the double difference data from the modified details and approximations.

5) Re-compute the correlation based on Equation (4-12) for each modified double difference which are C_{12}\`, $C_{13}$\` and C_{23}\`.

6) Compute the correlation reduction for each baseline over two days as follow:

$$C\_red = \frac{C' - C}{C} \tag{4-13}$$

7) Repeat steps 2 through 6 for levels of decomposition 2 to 12.

Table 4-3: Candidates wavelet base function used in this chapter

	Base		Base		Base		Base		Base		Base		Base		Base
1	Db2	6	Db7	11	Sym3	16	Sym8	21	Coif4	26	Bior2.2	31	Bior3.3	36	Bior5.5
2	Db3	7	Db8	12	Sym4	17	Sym9	22	Coif5	27	Bior2.4	32	Bior3.5	37	Bior6.8
3	Db4	8	Db9	13	Sym5	18	Sym10	23	Bior1.1	28	Bior2.6	33	Bior3.7		
4	Db5	9	Db10	14	Sym6	19	Coif2	24	Bior1.3	29	Bior2.8	34	Bior3.9		
5	Db6	10	Sym2	15	Sym7	20	Coif3	25	Bior1.5	30	Bior3.1	35	Bior4.4		

At this point there should be 128 modified double differences over three days with 12 levels of decomposition. This equals 4608 correlation values. The wavelet base function that reports the highest correlation reduction in these 4608 correlation values is considered the best candidate for this analysis. This is because the wavelet base function that reports the highest correlation reduction is the one that can most efficiently isolate the correlated signals at the wavelets bandwidth to its original details.

Table 4-4 shows the wavelet base function and the number of times that it reported the maximum correlation reduction. It also shows the frequency with which each wavelet base function reports a maximum correlation reduction for each baseline category in L1 and ionosphere free measurement (L3). It can be seen from the table that a biorthogonal wavelets family achieved the highest degree of correlation reduction (60%-70%). The closest family is the Daubechies family (25%-30%). It is evident from the figure that the bior2.2 in the biorthogonal wavelets family performed better than all the other wavelets functions for short baselines in Category I, while bior3.3 performed better for longer baselines in Category II. Coiflets and Symlet performed the worst in detecting the correlated signal as they only show around 1% for Coiflets and 8% for Symlet. Moreover, the effect of the base function on both L1 and L3 measurements is almost the same except for longer baselines (Category II). This is the result of ionosphere free linear combination, which removes the first order ionospheric (uncorrelated errors) errors and makes the correlated error more clear. Consequently, the L3 Category has a higher percentage than L1 Category, particularly at the biorthogonal family.

Based on this analysis, the use of Coiflets or Symlet is not recommended for correlated error detection of GPS double difference measurements. However, the biorthogonal method is recommended to isolate the correlated error, especially bior2.2 for short baseline and bior3.3 for longer baselines.

Table 4-4: Wavelet base function and the number of times it recorded the maximum Correlation reduction.

	L1_Category I			L1_ Category II			L3_ Category I			L3_ Category II		
	N	%	Total	N	%	Total	N	%	Total	N	%	Total
db2	432	13.6		161	11.2		442	14.0		182	12.6	
db3	101	3.2		23	1.6		67	2.1		32	2.2	
db4	105	3.3		48	3.3		107	3.4		45	3.1	
db5	69	2.2		19	1.3		66	2.1		11	0.8	
db6	54	1.7		17	1.2		42	1.3		15	1.0	
db7	47	1.5		15	1.0		40	1.3		13	0.9	
db8	51	1.6		23	1.6		48	1.5		14	1.0	
db9	44	1.4		19	1.3		35	1.1		10	0.7	
db10	54	1.7	30.2	21	1.5	24.0	53	1.7	28.4	11	0.8	23.1
sym4	78	2.5		26	1.8		66	2.1		21	1.5	
sym5	43	1.4		10	0.7		38	1.2		11	0.8	
sym6	24	0.8		5	0.3		13	0.4		3	0.2	
sym7	54	1.7		16	1.1		48	1.5		13	0.9	
sym8	10	0.3		5	0.3		2	0.1		2	0.1	
sym9	34	1.1		11	0.8		24	0.8		2	0.1	
sym10	25	0.8	8.5	7	0.5	5.6	23	0.7	6.8	2	0.1	3.8
coif2	14	0.4		0	0.0		12	0.4		3	0.2	
coif3	12	0.4		0	0.0		8	0.3		2	0.1	
coif4	19	0.6		0	0.0		22	0.7		3	0.2	
coif5	38	1.2	2.6	12	0.8	0.8	23	0.7	2.1	3	0.2	0.8
bior1.1	0	0.0		0	0.0		0	0.0		0	0.0	
bior1.3	249	7.9		4	0.3		211	6.7		120	8.3	
bior1.5	82	2.6		106	7.4		62	2.0		35	2.4	
bior2.2	492	15.5		33	2.3		539	17.0		273	19.0	
bior2.4	62	2.0		264	18.3		50	1.6		16	1.1	
bior2.6	26	0.8		21	1.5		16	0.5		7	0.5	
bior2.8	27	0.9		8	0.6		21	0.7		5	0.3	
bior3.1	294	9.3		7	0.5		497	15.7		340	23.6	
bior3.3	383	12.1		298	20.7		365	11.5		177	12.3	
bior3.5	100	3.2		192	13.3		114	3.6		36	2.5	
bior3.7	49	1.5		28	1.9		32	1.0		7	0.5	
bior3.9	30	0.9		12	0.8		34	1.1		8	0.6	
bior4.4	25	0.8		12	0.8		16	0.5		7	0.5	
bior5.5	31	1.0		11	0.8		21	0.7		6	0.4	
bior6.8	10	0.3	58.7	6	0.4	69.6	11	0.3	62.8	5	0.3	72.4
Total	3168		100.0	1440		100.0	3168		100.0	1440		100.0

II. Level of decomposition.

The same criteria used in the previous section to select the best wavelet base function are used to select the level of decomposition that occurred for most of the correlated signals between days. Each of the 128 double difference measurements mentioned in Table 4-2 is decomposed to approximation and details at levels of decompositions from one to 12 using a bior3.3 base function. The criterion for selecting the best level of decomposition is the same as described in the previous section with the exception of bior3.3, which is the only base function used in this section. There were 128 double difference data over three days (a total of 384) that were decomposed using a bior3.3 wavelet base function. Each of these 384 double difference data were processed as described in the following steps:

1) Decompose each of the 384 double difference data to approximation and details at levels of decomposition from 1 to 12.
2) At each level of decomposition set the details coefficients to zero, this step will delete all the high-frequency data at this level.
3) Reconstruct the double difference data from the modified details and approximations.
4) Re-compute the correlation based on Equation (4-12) for each modified double differences which are C_{12}\`, $C_{13}$\` and C_{23}\`.
5) Compute the correlation reduction for each baseline between two days using the reference correlation values computed in the previous section.
6) For each baseline at each day record the level of decomposition that provides the maximum correlation reduction.

Table 4-5 shows the frequency with which the maximum correlation reduction is achieved for each level of decomposition. It can be seen from the table that Level 1 and 2 never indicate any maximum correlation reduction. This is because Level 1 and 2 contain mostly uncorrelated white noise. From Level 3 to Level 5, there is only 1% - 2% of the maximum correlation detected, which is a strong indication that the correlated signal did not appear until Level 5. Levels 6 and 7 indicate a maximum correlation 10% of the time. Most of the correlated signal appeared at Levels 8, 9 and 10. For Category I baselines (short baselines) Levels 8 and 9 have the most correlated signal, while Category II baselines (longer baselines) indicate most of the correlation at Levels 9 and 10. The results from L1 measurements are identical to the results from L3 measurements is a strong indication that the level of decomposition is acting the same in both L1 and L3 measurements.

Table 4-5: level of decomposition and the number of times it recorded the maxiumuin Correlation reduction .

	L1_Category I		L1_ Category II		L3_ Category I		L3_ Category II	
	N	%	N	%	N	%	N	%
3	2	0.8	0	0.0	2	0.8	0	0.0
4	5	1.9	0	0.0	5	1.9	0	0.0
5	4	1.5	0	0.0	4	1.5	0	0.0
6	32	12.1	4	3.3	32	12.1	4	3.3
7	22	8.3	0	0.0	22	8.3	0	0.0
8	99	37.5	12	10.0	99	37.5	12	10.0
9	72	27.3	42	35.0	72	27.3	42	35.0
10	28	10.6	62	51.7	28	10.6	62	51.7
Total	264		120		264		120	

III. Threshold type and threshold estimator.

Each of the 128 double difference measurements mentioned in Table 4-2 were decomposed to approximation and details at levels of decomposition from one to 12 using bior3.3. The criterion for selecting the best wavelets base candidate is described in the wavelet base function and vanishing moment section. The difference in this section is only one base function (bior3.3) was used. Table 4-6 shows the frequency with which the maximum correlation reduction is achieved for each thresholding type/estimator. It can be seen from the table that Median _s, where s stands for soft and h for hard thresholding, shows approximately 50% of the maximum correlation reduction and the second best type/estimator Minimax_s with around 30%. These results were for baselines categories I and II and for L1 and L3.

Table 4-6: Threshold type/estimator and the number of times it recorded the maxiumuin Correlation reduction.

	L1_Category I		L1_ Category II		L3_ Category I		L3_ Category II	
	N	%	N	%	N	%	N	%
Heuristic _h	126	4.0	101	7.0	145	4.6	88	6.1
Heuristic _s	75	2.4	89	6.2	72	2.3	91	6.3
Minimax _h	71	2.2	57	4.0	89	2.8	40	2.8
Minimax _s	1090	34.4	526	36.5	1152	36.4	564	39.2
Median _h	38	1.2	19	1.3	59	1.9	30	2.1
Median _s	1630	51.5	599	41.6	1566	49.4	588	40.8
Rigrsure _h	38	1.2	17	1.2	39	1.2	14	1.0
Rigrsure _s	100	3.2	32	2.2	46	1.5	25	1.7
Total	3168		1440		3168		1440	

4.3.2 Results

4.3.2.1 Short Baselines

The first category of baselines, of a few hundred meters to five kilometres, was used to compute the coordinates for E1, E2, W6, NH2, NH3, NH4 and NH5. Table 4-7 shows the coordinate differences (bias) and the root mean square error of these coordinates with respect to the reference coordinates by employing the Bernese software. Results for short baseline match the reference coordinates within 5-15 mm and RMS within 10 mm. In this category, the L1 fixed solution is used as the correlated errors are either eliminated or radically removed in the short baselines.

Table 4-7: Coordinates difference (mm) and RMS (mm) for short baseline using L1 fixed solution with respect to the coordinates computed in Chapter 3.

Ref	Rover	Baseline	Sol	X Bias	Y Bias	H Bias	Z Bias	X RMS	Y RMS	H RMS	Z RMS
N5	E1	92.5	Fixed	3.0	4.0	5.0	4.0	4.0	8.0	8.9	6.0
N5	E2	94.1	Fixed	5.0	7.0	8.6	5.0	8.0	8.0	11.3	8.0
N5	W6	108.1	Fixed	4.0	3.0	5.0	9.0	11.0	13.0	17.0	13.0
NH1	NH2	277.3	Fixed	4.0	8.0	8.9	11.0	3.0	5.0	5.8	5.0
NH1	NH3	194.0	Fixed	7.0	7.0	9.9	18.0	5.0	9.0	10.3	9.0
NH1	NH4	192.8	Fixed	6.0	9.0	10.8	12.0	4.0	6.0	7.2	6.0
NH1	N05	5378.4	Fixed	11.0	15.0	18.6	9.0	7.0	12.0	13.9	13.0

Wavelets Multi-Resolution is applied to the L1 measurement using both the median threshold estimator and the kill approximation techniques. Bior 3.3 wavelet base function is used to decompose each double difference measurement to eight levels of decomposition. The proposed wavelet de-trending technique is then used to separate and differentiate different frequencies from high to low, corresponding with GPS errors. This produced a corrected double difference data as explained in the previous section. In addition, the performance of the wavelet de-trending technique is compared with the traditional wavelet de-noising method using a median estimator. The corrected double difference measurements from both de-noising and de-trending techniques are used with the least square adjustment to produce a fixed GPS solution. Least-squares AMBiguity Decorrelation Adjustment (LAMBDA) method was used in this thesis to fix the ambiguity (Teunissen, 1993) in addition to the Saastamoinen model for troposphere error modeling. Figure 4-6 and Figure 4-7 show the bias and RMS reduction in the final solution (X, Y and Z components). The double difference measurements were corrected using both de-trending and de-noising techniques. It can be seen from Figure 4-6 that the de-noising technique reduced the bias for short baselines from 5% at X-Bias for NH1-NH2 baseline (from 8 mm to 7.6 mm) to 40% at X-Bias for N5-E2 baseline (from 5 mm to 3 mm). The RMS improvements for short baselines vary between 16% at Y-RMS from baseline N5-E1 (from 8 mm to 6.7 mm) to 44% at X-RMS for baseline NH1-N5 (from 7 mm to 3.9 mm). The average bias reduction for all the X, Y and Z components is 23%, while the average RMS reduction is 30% when using the de-noising technique (Figure 4-7). The de-trending technique reduces the bias and RMS as shown in Figure 4-6 and Figure 4-7. The bias for short baselines is reduced from 53% at Z-Bias for NH1-NH2 baseline (from 11 mm to 5.2 mm) to 84% at X-Bias for N5-E2 baseline (from 5 mm to 0.8 mm). The RMS reductions for short baselines vary between 51% at Y-RMS from baseline N5-W6 (from 13 mm to 6.3 mm) to 82.5% at Y-RMS for baseline N5-E2 (from 8 mm to 1.4 mm). The average bias reduction for all the X, Y and Z components is 74%, while the average RMS reduction is 69% when using the de-noising technique.

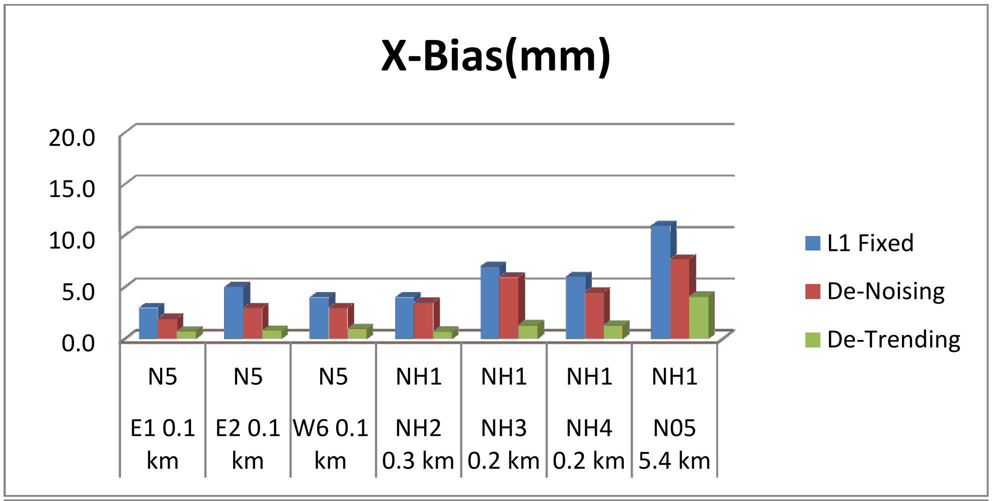

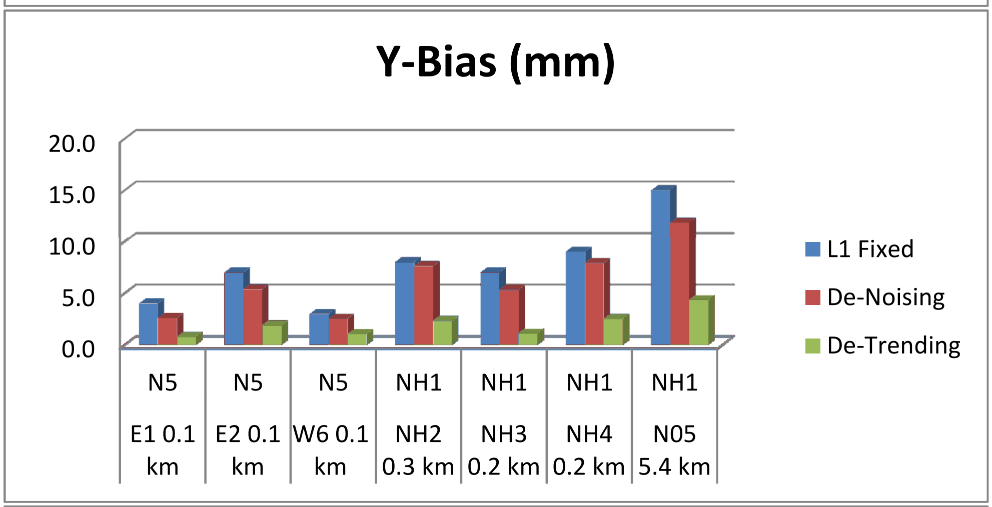

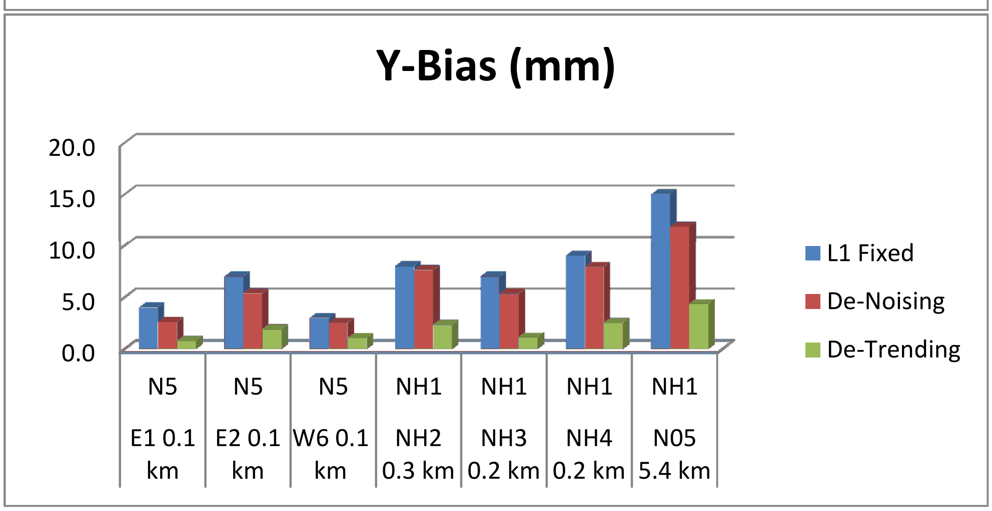

Figure 4-6: Coordinate bias when computed with raw data (L1 Fixed), De-Noising and De-Trending techniques for short baselines.

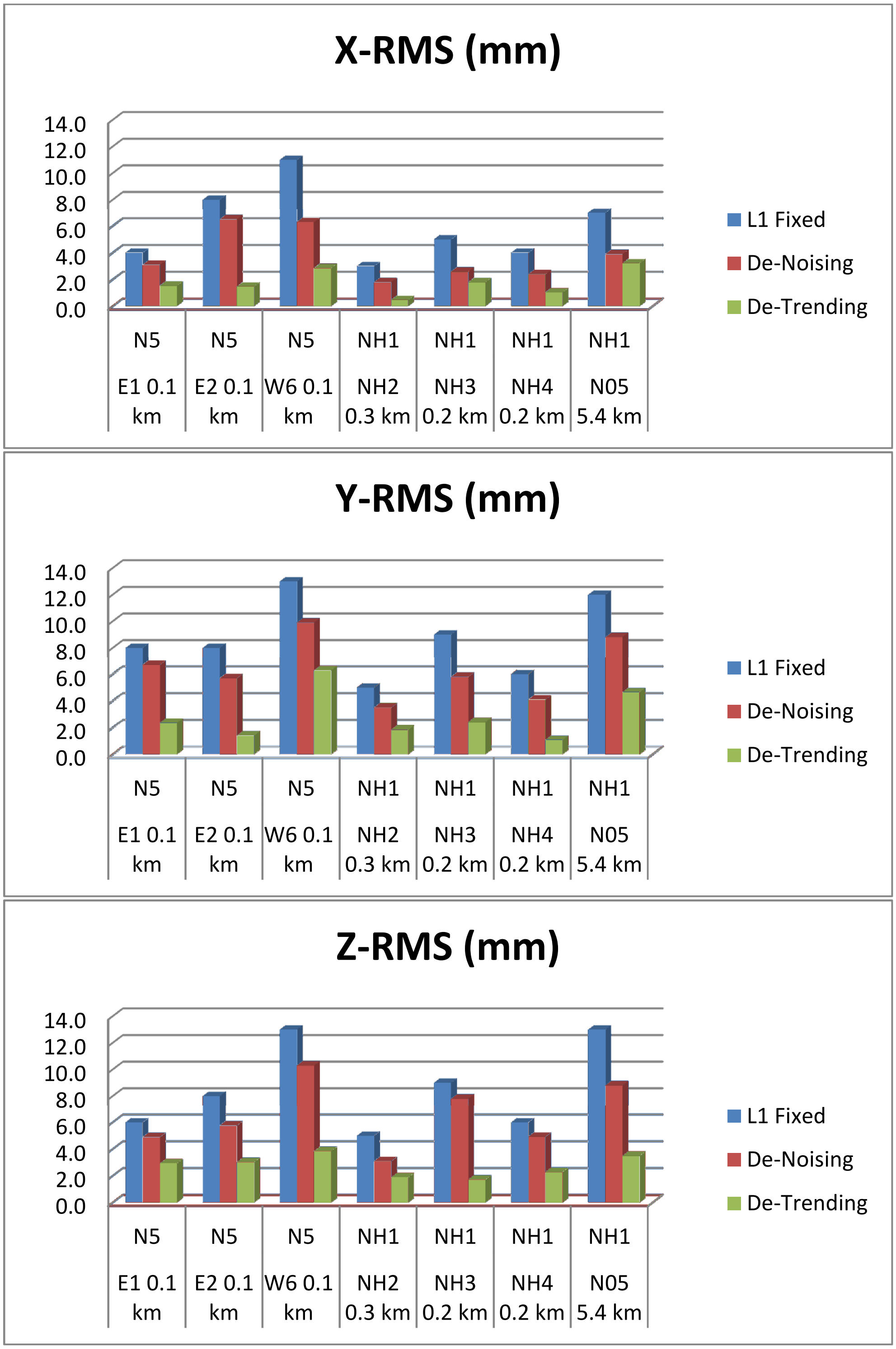

Figure 4-7: Coordinate RMS when computed with raw data (L1 Fixed), De-Noising and De-Trending techniques for short baselines.

4.3.2.2 Long Baselines

The second category baselines range from 20 to 50 kilometres. They are used to compute the coordinates for SBNK, AIR2, PRDS, COCH and STRA using the batch processing implementation described in section 3.2. The coordinate difference (bias) and the root mean square error of the computed coordinates with respect to the reference coordinates using the Bernese software are shown in Table 4-8) where L1 float solution is used, Table 4-9) where Ionosphere free float solution is used and Table 4-10 where Ionosphere free fixed solution is used.

Table 4-8: Coordinates difference (mm) and RMS (mm) for long baseline using L1 float solution with respect to the coordinates computed in Chapter 3.

Ref	Rover	Baseline	Sol	X Bias	Y Bias	H Bias	Z Bias	X RMS	Y RMS	H RMS	Z RMS
NCAL	SBNK	20686.2	Float L1	19.0	22.0	29.1	24.0	32.0	28.0	42.5	28.0
NCAL	AIR2	23126.6	Float L1	22.0	25.0	33.3	33.0	41.0	49.0	63.9	41.0
N05	PRDS	25756.3	Float L1	32.0	28.0	42.5	35.0	43.0	58.0	72.2	81.0
NCAL	COCH	28481.2	Float L1	15.0	18.0	23.4	28.0	53.0	32.0	61.9	45.0
NH1	PRDS	30750.8	Float L1	28.0	23.0	36.2	37.0	44.0	35.0	56.2	63.0
NCAL	STRA	46215.2	Float L1	35.0	42.0	54.7	48.0	28.0	52.0	59.1	77.0

Table 4-9: Coordinates difference (mm) and RMS (mm) for long baseline using IF float solution with respect to the coordinates computed in Chapter 3.

Ref	Rover	Baseline	Sol	X Bias	Y Bias	H Bias	Z Bias	X RMS	Y RMS	H RMS	Z RMS
NCAL	SBNK	20686.2	Float IF	4.0	3.0	5.0	9.0	12.0	14.0	18.4	8.0
NCAL	AIR2	23126.6	Float IF	2.0	3.0	3.6	12.0	10.0	9.0	13.5	16.0
N05	PRDS	25756.3	Float IF	5.0	4.0	6.4	11.0	14.0	11.0	17.8	18.0
NCAL	COCH	28481.2	Float IF	8.0	10.0	12.8	8.0	17.0	20.0	26.2	20.0
NH1	PRDS	30750.8	Float IF	6.0	7.0	9.2	15.0	11.0	17.0	20.2	63.0
NCAL	STRA	46215.2	Float IF	12.0	9.0	15.0	14.0	21.0	19.0	28.3	23.0

Table 4-10: Coordinates difference (mm) and RMS (mm) for long baseline using IF fixed solution with respect to the coordinates computed in Chapter 3.

Ref	Rover	Baseline	Sol	X Bias	Y Bias	H Bias	Z Bias	X RMS	Y RMS	H RMS	Z RMS
NCAL	SBNK	20686.2	Fixed IF	8	3	9	2	13.0	18.0	22	6.0
NCAL	AIR2	23126.6	Fixed IF	2	11	11	4	8.0	15.0	17	9.0
N05	PRDS	25756.3	Fixed IF	3	3	4	7	10.0	10.0	14	12.0
NCAL	COCH	28481.2	Fixed IF	9	0	9	12	15.0	7.0	17	26.0
NH1	PRDS	30750.8	Fixed IF	5	9	10	4	10.0	19.0	21	42.0
NCAL	STRA	46215.2	Fixed IF	10	4	11	12	14.0	12.0	18	20.0

The results for long baselines L1 float solution match the reference coordinates within 19-50 mm and RMS within 50 mm. Wavelets Multi-Resolution is applied to the L1 measurement using Bior 3.3 with both the median threshold estimator and the de-trending techniques to the eight levels of decomposition. The estimated error is used to correct each double difference measurements before the estimation process begins again. In addition, the performance of the wavelets de-trending technique is compared with the traditional wavelets de-noising using a median estimator. Figure 4-8 and Figure 4-9 show the bias and RMS reduction in the final solution (X, Y and Z components) after correcting the double difference measurements using both de-trending and de-noising techniques. It can be seen from Figure 4-8 that the de-noising technique reduced the bias for long baselines from 15% at Y-Bias for NCAL-COCH baseline (from 18 mm to 15 mm) to 42% at X-Bias for NCAL-COCH baseline (from 15 mm to 8.7 mm).

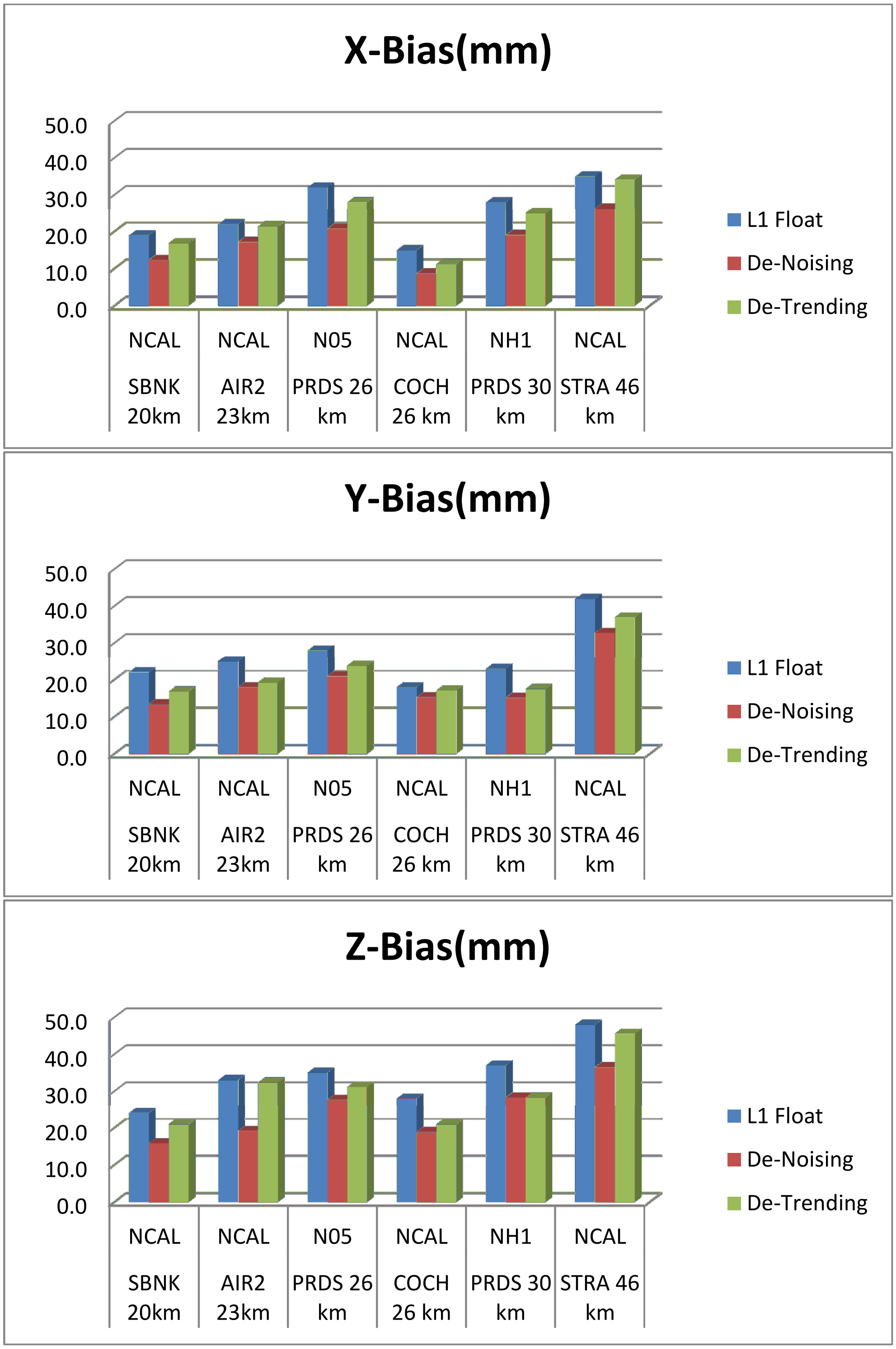

Figure 4-8: Coordinate bias when computed with raw data (L1 float), De-Noising and De-Trending techniques for long baselines.

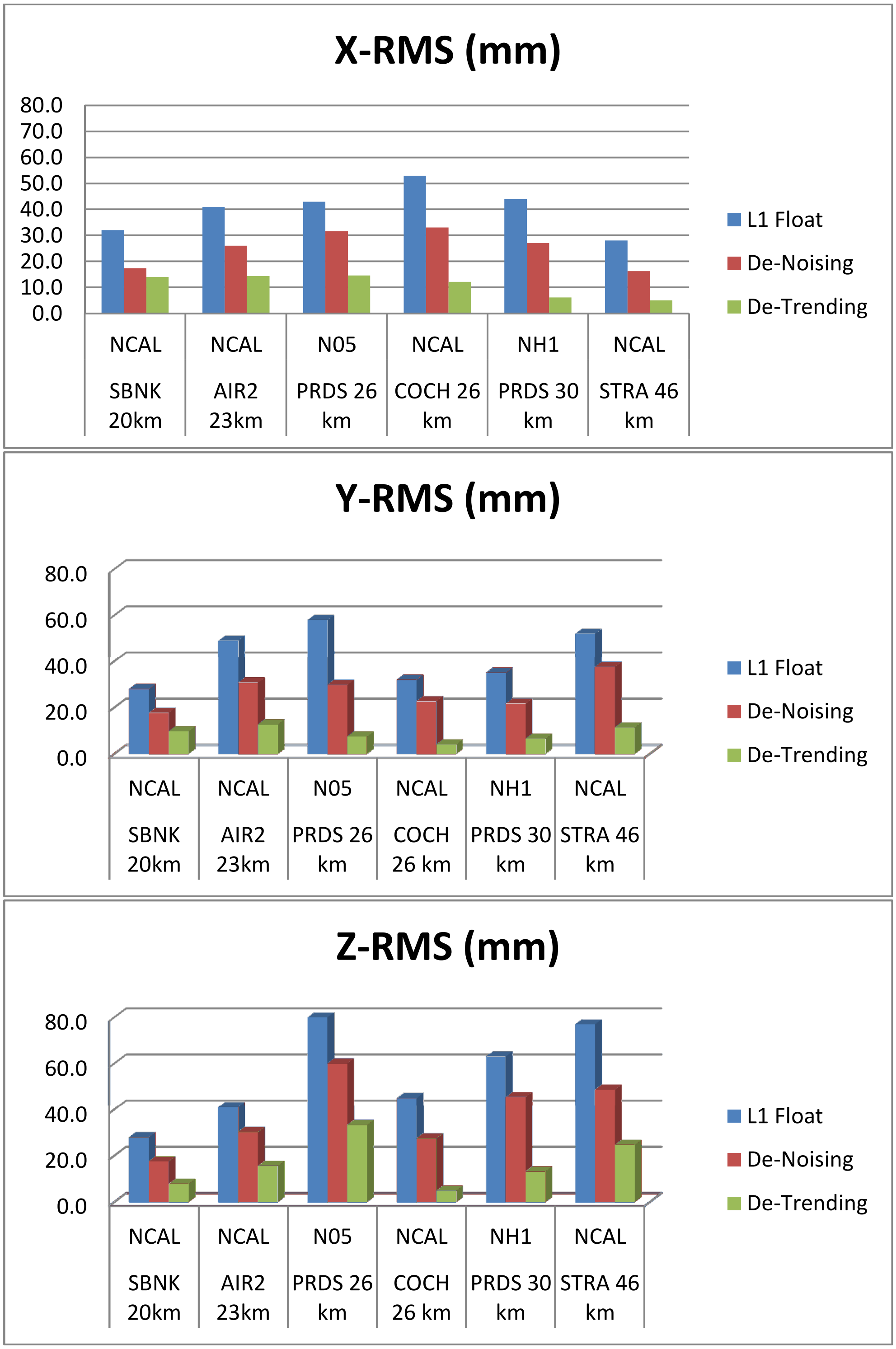

Figure 4-9: Coordinate RMS when computed with raw data (L1 Float), De-Noising and De-Trending techniques for long baselines.

The RMS reductions for long baselines (Figure 4-9) vary between 25% at Z-RMS from baseline N5-PRDS (from 81 mm to 60 mm) to 49% at Y-RMS for baseline N5-PRDS (from 58 mm to 29.8 mm). The average bias reduction for all the X, Y and Z components is 30%, while the average RMS reduction is 36% when using the de-noising technique.

The de-trending technique reduction to bias and RMS can be seen in the same figures. The bias for short baselines was reduced from 2% at Z-Bias for NCAL-AIR2 baseline (from 33 mm to 32.2 mm) to 25% at X-Bias for NCAL-COCH baseline (from 15 mm to 11 mm). The RMS improvements for long baseline L1 float solution vary from 56% at X-RMS from baseline NCAL-SBNK (from 32 mm to 14 mm) to 89% at Z-RMS for baseline NCAL-COCH (from 45 mm to 5 mm). The average bias reduction for all the X, Y and Z components is 14%, while the average RMS reduction when using the de-noising technique is 75%.

Figure 4-10 and Figure 4-11show the bias and RMS reduction in the final solution (X, Y and Z Cartesian components) after correcting the double difference measurements using both de-trending and de-noising techniques. It can be seen from Figure 4-10 that the de-noising technique reduced the bias for long baselines from 17.5% at Y-Bias for NCAL-COCH baseline (from 10 mm to 8.3 mm) to 60% at X-Bias for N05-PRDS baseline (from 5 mm to 2 mm). The RMS reductions for long baselines (Figure 4-11) vary between 22% at Z-RMS from baseline NH1-PRDS (from 63 mm to 48 mm) to 42% at X-RMS for baseline NCAL-STRA (from 21mm to 12.2 mm).

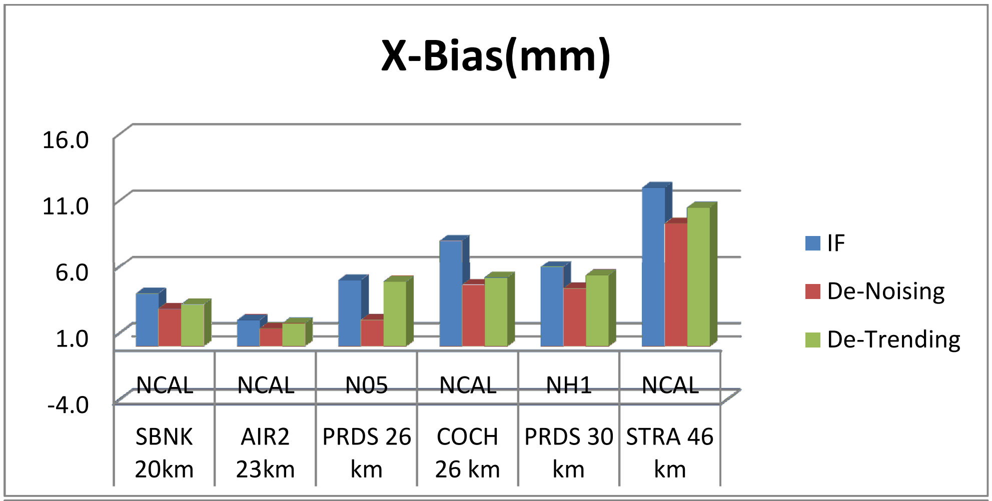

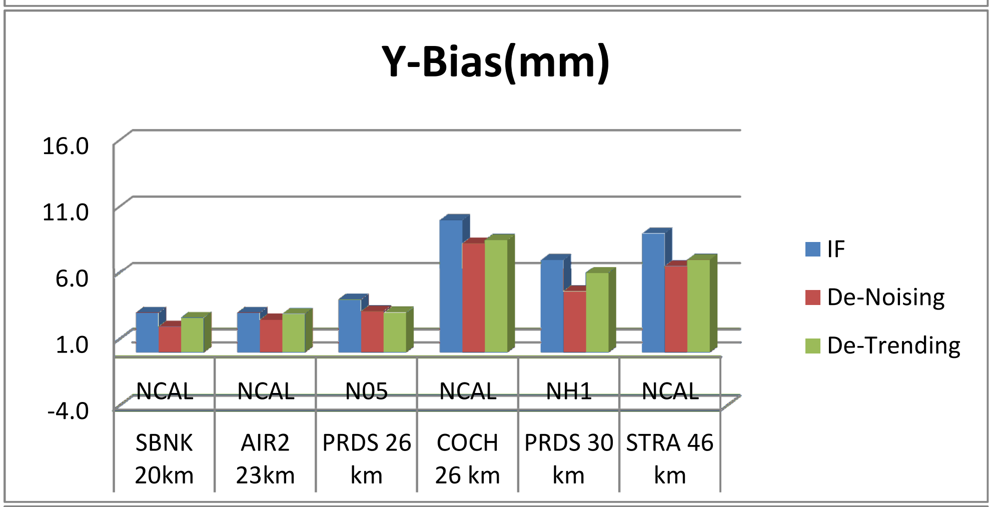

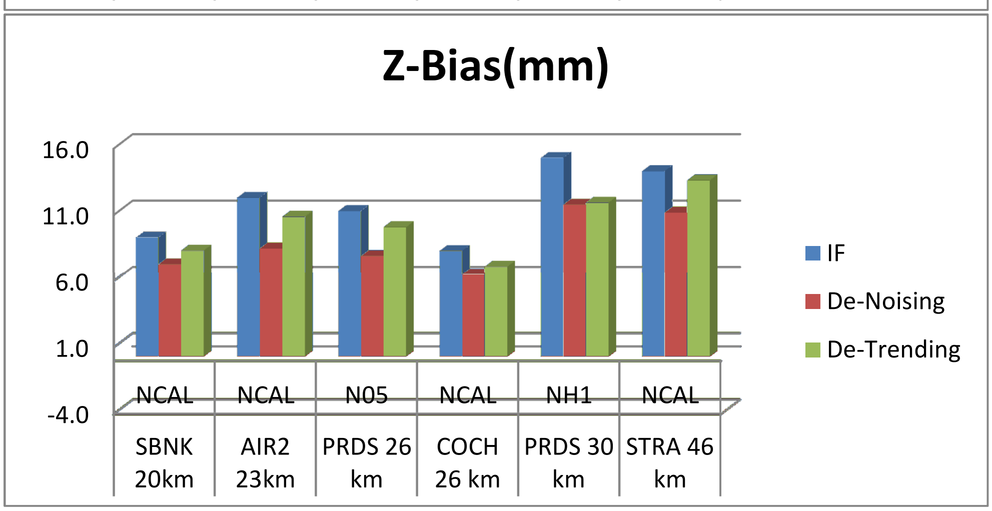

Figure 4-10: Coordinate bias when computed with raw data (IF-Float), De-Noising and De-Trending techniques for long baselines.

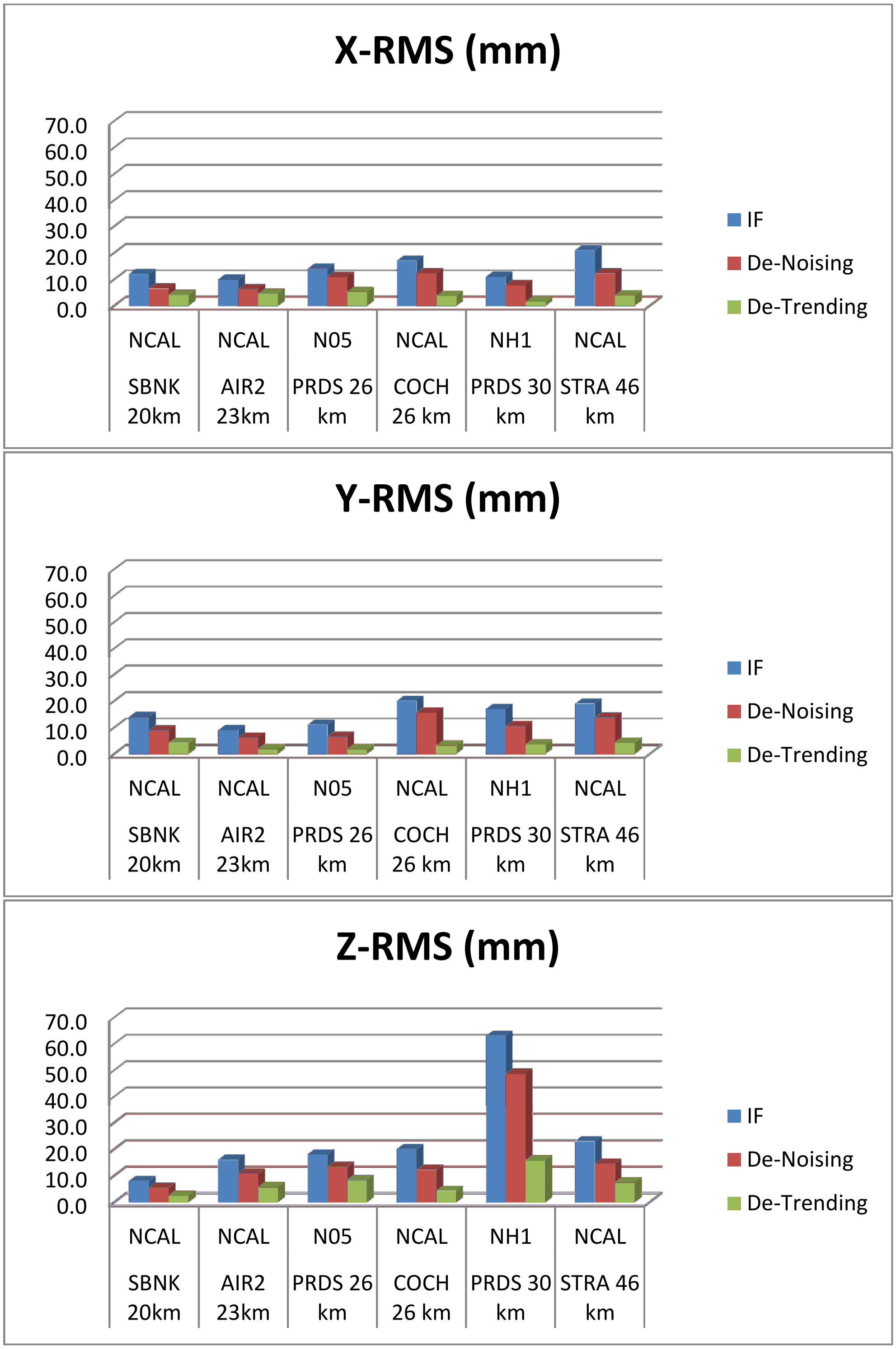

Figure 4-11: Coordinate RMS when computed with raw data (IF-Float), De-Noising and De-Trending techniques for long baselines.

The average bias reduction for all the X, Y and Z components is 20%, while the average RMS reduction when using the de-noising technique is 33%. The de-trending technique reduction to bias and RMS can be seen in the same figures. The bias for the long baselines was reduced from 3% at Y-Bias for NCAL-AIR2 baseline (from 3 mm to 2.9 mm) to 35% at X-Bias for NCAL-COCH baseline (from 8 mm to 5.2 mm). The RMS reductions, for long baseline IF solution, vary between 54% at Z-RMS for baseline NCAL-AIR2 (from 18 mm to 8.3 mm) to 86% at X-RMS for baseline NH1-PRDS (from 11 mm to 1.5 mm). The average bias reduction for all the X, Y and Z components is 15%, while the average RMS reduction when using the de-trending technique is 73%.

Figure 4-12 and Figure 4-13 show the bias and RMS reduction in the ionosphere free fixed final solution (X, Y and Z Cartesian components) after correcting the double difference measurements using both de-trending and de-noising techniques. It can be seen from Figure 4-12 that the de-noising technique reduced the bias for long baselines from 8% at X-Bias for N5-PRDS baseline (from 3 mm to 2.8 mm) to 28% at X-Bias for NH1-PRDS baseline (from 5 mm to 3.6 mm). The RMS reductions for long baselines (Figure 4-13) vary between 5% at Z-RMS from baseline NCAL-SBNK (from 6 mm to 5.7 mm) to 27% at X-RMS for baseline NCAL-SBNK (from 13mm to 9.4 mm). In case of de-trending solution, the bias was reduced from 3% at Z-Bias for NH1-PRDS baseline to 31% at Z-Bias for NCAL-STRA baseline. The RMS improvements vary from 14% at Y-RMS from baseline NCAL-COCH to 84% at X-RMS for baseline NCAL-AIR2.

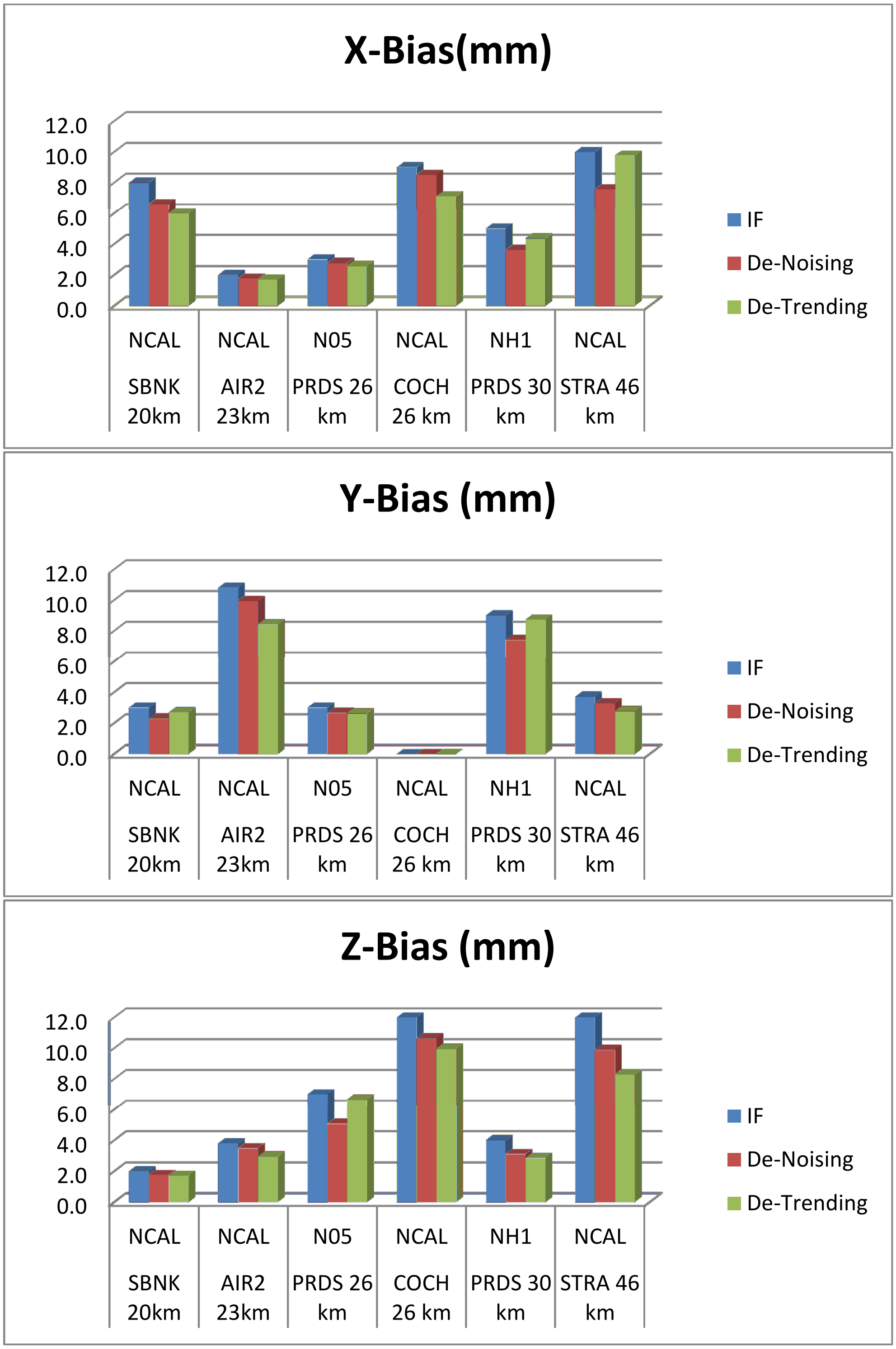

Figure 4-12: Coordinate bias when computed with raw data (IF-Fixed), De-Noising and De-Trending techniques for long baselines.

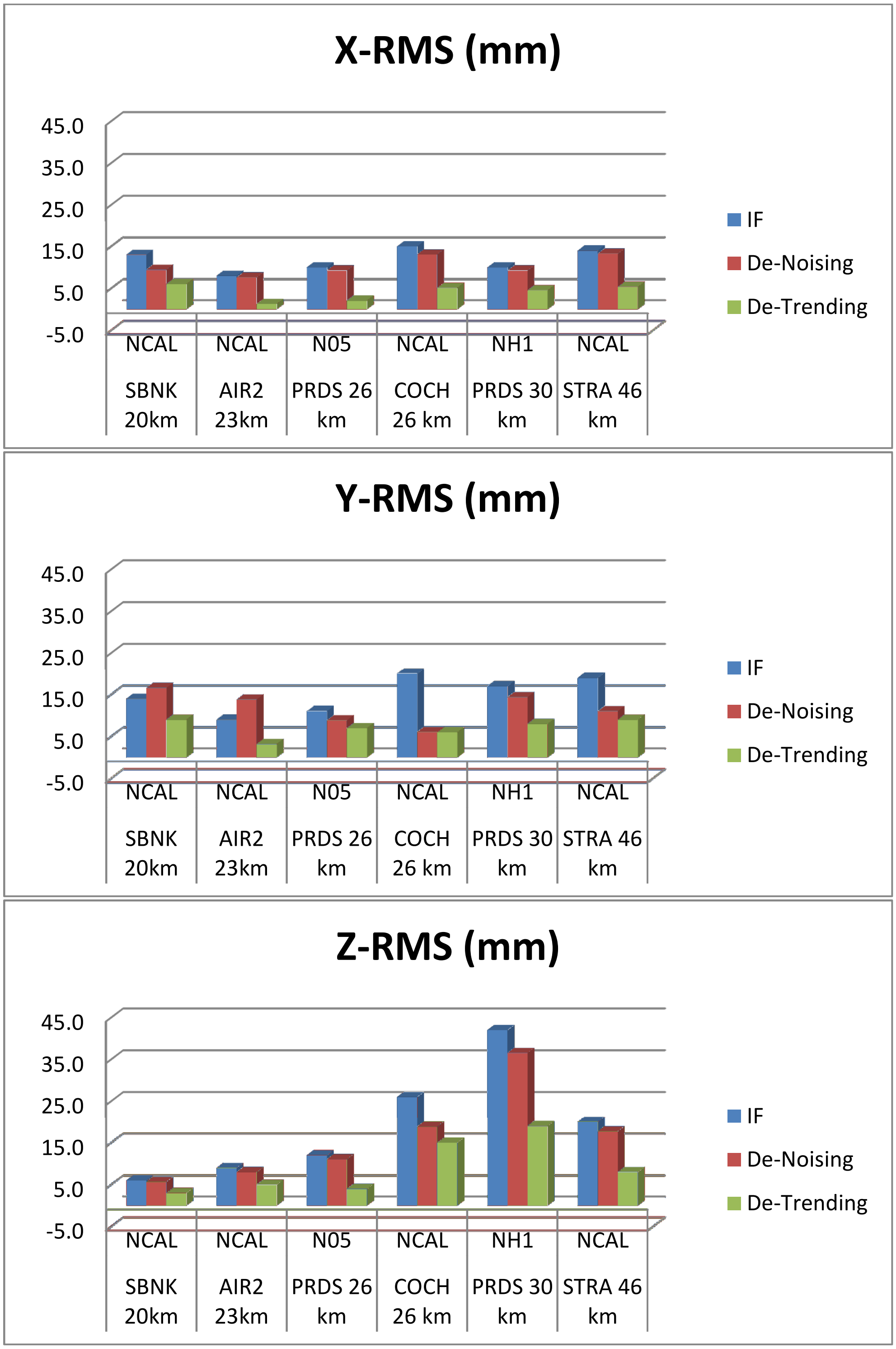

Figure 4-13: Coordinate RMS when computed with raw data (IF-Fixed), De-Noising and De-Trending techniques for long baselines.

Table 4-11 lists the summary of the analysis made in the previous sections. It can be seen from the table that the de-noising technique gives consistence results for both short and long baselines. The average bias reduction that can be achieved from the de-noising technique is around 20-30% and the average RMS reduction is around 30-40%. Moreover, the de-trending technique out-performs the de-noising technique for RMS improvement in short and long baselines. The performance in the de-trending technique is almost three times better than the traditional de-noising technique for bias and RMS reduction.

Although the de-trending technique out-performs the de-noising technique in the RMS reduction, it does produce inconsistence results for the bias reduction. The de-trending methodology performed impressively for short baselines in RMS and bias reduction as the average RMS and bias reduction were around 80%. However, for longer baselines the bias reduction is minimal although the RMS reduction is still in the range of 50-80% reduction. It can be concluded that the de-trending technique can reduce the double difference errors dramatically for short baselines. Conversely, the de-trending technique can cause a biased solution for long baselines, as it will enhance the RMS value and indicate good statistics for the solution but not enhance the bias to the same level.

Table 4-11: average bias (mm) and RMS (mm) reduction in percentage for fixed short baseline solution and long baseline float and IF solution

Fixed L1	**De-Noising**	**De-Trending**
Average Bias	23	73
Average RMS	29	68
Float L1	**De-Noising**	**De-Trending**
Average Bias	29	13
Average RMS	35	74
Float IF	**De-Noising**	**De-Trending**
Average Bias	28	14
Average RMS	32	72
Fixed IF	**De-Noising**	**De-Trending**
Average Bias	16	17
Average RMS	12	54

Chapter Five: Cycle Slip Detection and Estimation using Multi-scale Technique

5.1 Introduction

Cycle slips are integer cycle discontinuities in the GPS carrier phase measurements resulting from signal blocking, internal receiver tracking problems and low signal-to-noise ratio. Cycle slips cause the integer counter to re-initialize causing a jump in the carrier phase by integer number of cycles (Figure 5-1). Cycle slips can range between thousands of cycles and one cycle. High precision positioning and navigation results with GPS require the removal of cycle slips at the data pre-processing stage. This step requires the localization and computation of its value. The resulting error of only a few cycle slips can cause centimetre-level in both positioning or navigation errors.

In the past decade, many different research groups have studied cycle slips extensively and have proposed various techniques for locating and isolating them. One approach to detect cycle slip is by integrating GPS and INS data (Lee et al., 2003). Unfortunately, the cost and complexity of installing an INS system makes it difficult to use in many applications. Kalman filtering is a common method that many research groups use for detecting cycle slip (Han and Rizos, 1997). This method looks for any statistically significant discrepancies between the predicted time series estimated from the Kalman filter's dynamic model and the actual data time series. However, appropriate initial conditions and filter parameters must be obtained in order to conduct filter tuning. Another approach for detecting cycle slip involves the formation of a smooth (low-noise) cycle slip test quantity by linearly combining GPS measurements. These smooth quantities are generated by linear combinations of the raw carrier-phase and possibly pseudo-range observations at L1 and L2—which include time differencing, low degree polynomial fitting, Chebyshev polynomial and least-square technique (Bisnath, 2000). This can also be achieved by joining together two different measurements, such as wide-lane phase minus narrow-lane pseudo-range (Han, 1997), the geometry-free combination (Blewitt, 1990), the ionospheric total electron contents (TEC) rate (TECR) and Melbourne–Wübbena wide lane (MWWL) linear combination (Liu et al., 2011). Ultimately, the goal of all these approaches is to develop a smooth quantity that makes the cycle slip significant to detect. These techniques are highly successful in detecting the slip, unless there is high-noise due to multipath or high ionospheric activities are involved. High noise masks the cycle slip and makes it difficult to distinguish from noise. In this chapter, a new technique is introduced to differentiate between cycle slip and noise due to their different properties in the wavelet multi-scale domain. Although this technique is applied to two different combinations (code minus carrier and geometry-free), it can be used with any linear combination.

Singularities are points of sharp variations which indicate the local regularity of a signal. Cycle slip can be seen as a singularity in the GPS data, which must be detected and removed (Figure 5-2). The Continuous Wavelet Transform (CWT) is a method that successfully locates and identifies these singularities based on its ability to decompose a signal into elementary base functions using wavelet base functions that are well localized in both time and frequency domains. One of the advantages of CWT is that it provides redundant information between levels of decomposition (scales) that should be used to link the singularity between scales. Given this property, the CWT is capable of defining the local regularity of a signal. Collin and Warnant (1995) were the first to use wavelets to detect cycle slip and compare its performance with the Kalman filter. They discovered that there was no initial condition required to detect cycle slip using wavelets as is the case of Kalman filter. They also concluded that wavelets outperform Kalman filter when used to detect cycle slips in a geometry-free linear combination. In contrast, the Kalman filter outperforms the wavelet transform when applied to noisy data such as the code minus carrier observation. Recently a method for cycle slip processing in single-frequency navigation signal has been introduced by Chenxi et al., (2010). They used Haar wavelets to suppress the noise in code minus carrier observables. They reconstructed the de-noised code minus carrier from the second-layer approximation coefficients of wavelets decomposition. Then, they applied a threshold value based on the processed signal to determine cycle slips. Another approach to detect cycle slip using biorthogonal wavelets was proposed by Meng and Jia-hong, (2010). The authors benefited from the symmetry of biorthogonal wavelets to detect cycle slip in a simulated signal. They also computed the modulus maximum of wavelets coefficients to help in localizing cycle slip. Elhabiby et al., (2010) introduced the multi-scale technique to detect cycle slip based on a modulus maxima computation of the wavelet coefficients. This technique showed promising results when applied to signals with low noise values. However, when applied to signals that contained high noise it was difficult to separate singularity from noise.

Since Collin and Warnant's paper in 1995, the main focus of research was to investigate more base function (Chenxi et al., 2010; Meng and Jia-hong, 2010; Liu et al., 2011) or to use advanced techniques to localize the singularities (Liu et al., 2011; El-Ghazouly et al., 2009). But, the main disadvantage of using wavelets for cycle slip detection, which is the application of wavelets in noisy data for cycle slip detection, has not been solved or even investigated. Also, Collin and Warnant in their paper stated that Kalman filter outperforms the wavelet transform when applied to noisy data such as the code minus carrier observation. However, no research paper investigating the behaviour of any wavelet base function under different noise level has been found yet.

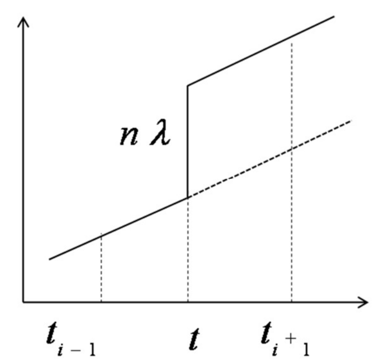

Figure 5-1. Cycle slip.

This chapter introduces a new multi-scale singularity detection and estimation technique used to detect cycle slip location and magnitude in a signal contaminated with noise. In this chapter, the property of wavelet base function (e.g. compact support and smooth functions) is discussed and the procedure for selecting a wavelet base function that annihilates the low order polynomial in the signal without data fitting is introduced. This is accomplished by interoperating the wavelet transform as a multi-scale differential operator. After that, the evolution of wavelet transform modulus maxima coefficients is discussed and the term maxima line is explained. Also in this chapter contains a computation of the decay of the wavelet coefficients between scales using Lipschitz exponent to characterize the regularity of the signal. Finally, the performance of the proposed technique is tested over code minus carrier and geometry-free linear combination GPS data combined with simulated slip. In addition, the ability of the proposed multi-scale technique to detect and estimate cycle slips over low signal to noise ratio is investigated. This chapter introduces a solution to the lack of singularity detection of the wavelets under high noise signal.

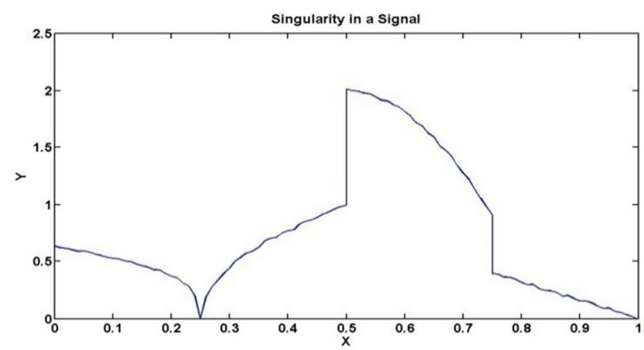

Figure 5-2. Singularity in a signal

5.2 Wavelet Base function

5.2.1 Compactly Support Wavelets

A compactly supported wavelet base function is the property whereby the wavelets coefficients can be nonzero for only a small range of the wavelets function. This "compact support" allows the wavelet transform to translate a time-domain function into a representation that is localized not only in frequency (like the Fourier transform) but in time as well. One example of a compact support wavelet is the Haar wavelet. Proposed in 1909 by Alfred Haar, the Haar wavelet is the earliest and simplest wavelet.

The Haar function (Figure 5-3) is described in Equation (5-1) as a step function, which matches the shape of singularity. This makes it the best candidate base function for detecting a jump or discontinuity. One disadvantage of the Haar base function is that it has a jump discontinuity especially in instances of smooth function which lead to poorly decaying Haar coefficients (Walnut, 2002). This means that using the Haar base function with smooth signal will lead to successive jumps in the wavelets coefficients due to the poorly decaying coefficients. Accordingly, Haar base function and its strong localization property should only be used in detecting discontinuity in linear signals while a smooth-base function should be used in cases of singularities in parabolic or polynomial signals.

$$\psi(t) = \begin{cases} 1 \; for \; t \in \,]0,0.5[\\ -1 \; for \; t \in [0.5,1] \\ 0 \quad Othewise \end{cases} \tag{5-1}$$

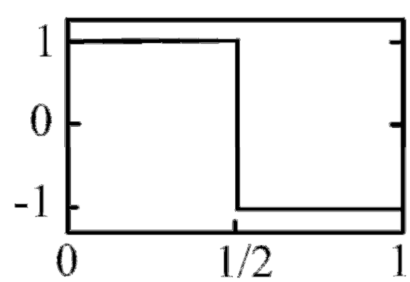

Figure 5-3. Haar base function

5.2.2 Smooth Wavelets

An important property that the wavelet base function should follow is regularity or smoothness. This property means that the wavelet function should have some smoothness and concentration (compact support) in both time and frequency domains.

5.2.3 Multi-scale Differential Operator

In cases of discontinuities in polynomial signals where the singularities are less noticeable, smooth wavelets defined by higher degree derivatives (vanishing moments) are needed. In such cases, the vanishing moment is the most important property by which the regularity of the signal can be measured. In cases using *n*-vanishing moment base function, the wavelet transform can be interoperated as a multi-scale differential operator of order *n*. A wavelet is said to have *n* vanishing moments, if and only if there exists $\theta$with a fast decay such that (Mallat and Hwang, 1992):

$$\psi(t) = (-1)^n \frac{d^n \theta(t)}{dt^n} \qquad \textbf{(5-2)}$$

Mallat and Hwang (1992) show that the wavelets coefficients at scale *s* can be computed for *n*-vanishing moments base function from Chapter 2 as follows:

$$\begin{aligned} Wf(u,s) &= \langle f * \psi_s(t) \rangle = s^n f\left(\frac{d^n \bar{\theta}_s}{dt^n}(u)\right) \\ &= s^n \frac{d^n}{du^n}(f * \bar{\theta}_s)(u) \end{aligned} \qquad \textbf{(5-3)}$$

With $\bar{\theta}_s(t) = s^{\frac{-1}{2}} \theta\left(^{-t}/_{s}\right)$

It can be seen from Equation (5-3) that the wavelet transform of a function $f(t)$ is the convolution of the n^{th} derivative of $f(t)$ and the wavelets function $\psi(t)$. Therefore, wavelets with *n*-vanishing moments are required to annihilate a polynomial of degree and order *n*−1, and detect singularity in this polynomial signal.

Figure 5-4 and Figure 5-5 shows the wavelets coefficients for a second order polynomial signal with noise (upper part). An example of a function θ that can have n vanishing moments and satisfy Equation (5-2) is the Daubechies wavelets. The wavelets coefficients are computed using Daubechies wavelets with two and three vanishing moments at levels 1, 2, and 3. It can be seen that wavelets with three vanishing moments are able to separate the noise out of the polynomial while wavelets with two vanishing moments give high coefficient values at the first levels of decomposition due to the polynomial signal. Another example of a function θ that can have n vanishing moments and satisfy Equation (5-2) is the Gaussian wavelets.

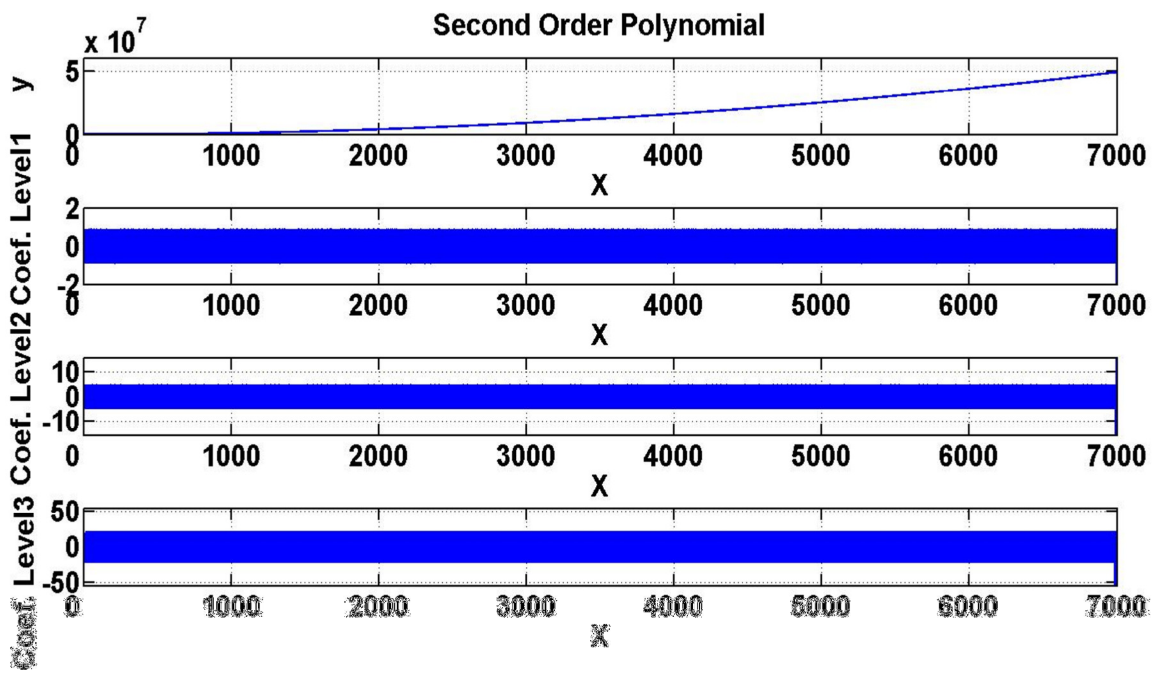

Figure 5-4. Wavelets coefficients at levels 1,2 and 3 when using Daubechies wavelets with 2 vanishing moment with second order polynomial with noise

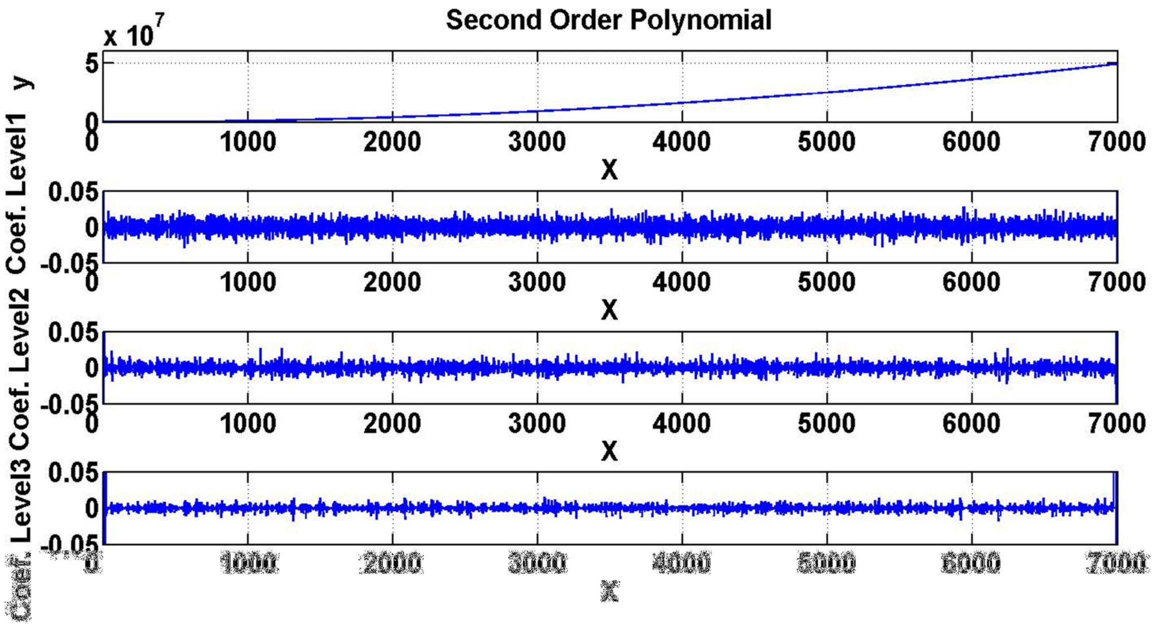

Figure 5-5. Wavelets coefficients at levels 1,2 and 3 when using Daubechies wavelets with 3 vanishing moment with second order polynomial with noise

5.3 The Wavelets-Transform and Lipschitz-Regularity

5.3.1 Lipschitz Regularity and Wavelets Decay

It is essential to precisely quantify the local regularity of a signal $f(t)$ to characterize singular structures. Lipschitz exponents provide global measurement of regularity at any point v and over time intervals as well. The decay of the wavelet transform amplitude across scales is related to the uniform and point wise Lipschitz regularity of the signal. Measuring this asymptotic decay is equivalent to zooming into signal structures with a scale that goes to zero. The term singularity at v means that the signal $f(t)$ is not differentiable at v. A function $f(t)$ is point wise Lipschitz $\alpha \geq 0$ at point v ,if K>0 exists, and a polynomial $p_v$of degree $m = \lfloor\alpha\rfloor$ such that (Mallat and Hwang, 1992):

$$|f(t) - p_v(t)| \leq K|t - v|^{\alpha} \qquad \textbf{(5-4)}$$

This can be seen as an error function $e_\alpha(t)$ that contains the difference between $f(t)$ and the polynomial $p_v(t)$.

$$f(t) = p_v(t) + e_\alpha(t) \tag{5-5}$$

With

$$e_\alpha(t) \leq K|t-v|^\alpha \tag{5-6}$$

The underlying idea for estimating Lipschitz regularity can be viewed using Equation (5-5) in two main steps. First it is required to find wavelets that can annihilate the polynomial part $p_v(t)$ and retain the error part $e_\alpha(t)$. This can be done as discussed in the previous section, using wavelet base function with *n+1* vanishing moments to remove the polynomial of order *n*. The next step is to find a relation between the wavelet transform and the Lipschitz exponent. This can be achieved by substituting the value of $f(t)$ in Chapter 2 from Equation (5-5) as follows:

$$Wf(u,s) = \int_{-\infty}^{\infty} (p_v(t) + e_\alpha(t)) \frac{1}{\sqrt{s}} \psi^*(\frac{t-u}{s})\, dt \tag{5-7}$$

If wavelet base function with *n* vanishing moments, where $n > \alpha$, is used to annihilate the polynomial signal $p_v(t)$ in Equation (5-7), the wavelet transform will be as follows:

$$Wf(u,s) = \int_{-\infty}^{\infty} e_{\alpha}(t)\frac{1}{\sqrt{s}}\psi^{*}(\frac{t-u}{s})\,dt \tag{5-8}$$

Using Equation (5-6) and (5-8), Mallat and Hwang (1992) show that if f is bounded and its wavelet transform coefficients ($Wf(u,s)$) satisfy Equation (5-9) for an $\alpha < n$, then f is uniformly Lipschitz α on $[a+\epsilon, b-\epsilon]$, for any $\epsilon > 0$.

$$\forall(u,s) \in \mathbb{R} \times \mathbb{R}^{+}, |Wf(u,s)| \leq As^{\alpha+1/2} \tag{5-9}$$

A is a constant.

Equation (5-9) is the main form of analyzing and estimating Lipschitz regularity of a function. Moreover, the Lipschitz regularity can be computed if the wavelet transform is known at two different scalesss_0, s_1, where $s_0 < s_1$, using the following Equation:

$$\alpha = \frac{log_2(|Wf(u,\ s_1)|) - log_2(|Wf(u,\ s_0)|)}{log_2(\ s_1) - log_2(\ s_0)} - \frac{1}{2} \tag{5-10}$$

5.3.2 Singularity Detection using Modulus Maxima Propagation

Measuring wavelet decay in the time-scale plane $(u,s)$for all wavelet coefficients is time consuming and faulty singularities can be found in the wavelet coefficients that have modulus maxima values. Mallat and Hwang (1992) proved that any function that has wavelet transform with no modulus maxima at fine scales is not singular in any neighbourhood. Modulus maxima of $Wf(u,s)$ is point v where $Wf(u,s)$ is locally maximum. The maximum should be strict from either left or right neighbourhoods of v to avoid modulus maxima values when $Wf(u,s)$ is constant. This suggests that:

$$\frac{\partial Wf(u_0,s_0)}{\partial u}=0 \qquad \textbf{(5-11)}$$

A maxima line is any connected curve in the time-scale space along all points that are a modulus maximum of the wavelet transform. To investigate the ability of modulus maxima in detecting singularity in the wavelets coefficient domain, the wavelet transform $f(t)$ is written as a multi-scale differential operator (Equation (5-12)). The multi-scale operator demonstrates the convolution between $f(t)$ and n-vanishing moments base function as the convolution between the n^{th} derivative of $f(t)$ and the base function $\bar{\theta}$. One example of a function θ that can have n vanishing moments and satisfy Equation (5-2) is the Gaussian wavelets. When using Gaussian wavelets with one vanishing moment to detect singularity, wavelets modulus maxima are the maxima of the first order derivative of $f(t)$ smoothed by $\bar{\theta}_s$ as illustrated in Figure 5-6 (b). Moreover, the point at which a smooth function has maximal growth (singularity) is the point at which the first derivative is maximal and the second derivative has zero-crossing. Therefore, if the Gaussian wavelet is used with two vanishing moments to detect the singularity, the singularity point will have a zero coefficient (Figure 5-6(c)). It should be noted that the coefficients in Figure 5-6(c) and Figure 5-6(d) are the derivatives of the smoothed signal $(f*\theta)$ shown at Figure 5-6(b). It can also be seen from Figure 5-6 that there are two modulus maxima in the cases that use wavelets from order two compared to only one modulus when using wavelets from order one. This shows that an increase in the vanishing moments of the wavelet base function also increases the number of modulus maxima.

$$Wf(u,s) = s^n \frac{d^n}{du^n}(f * \bar{\theta}_s)(u) \qquad (5\text{-}12)$$

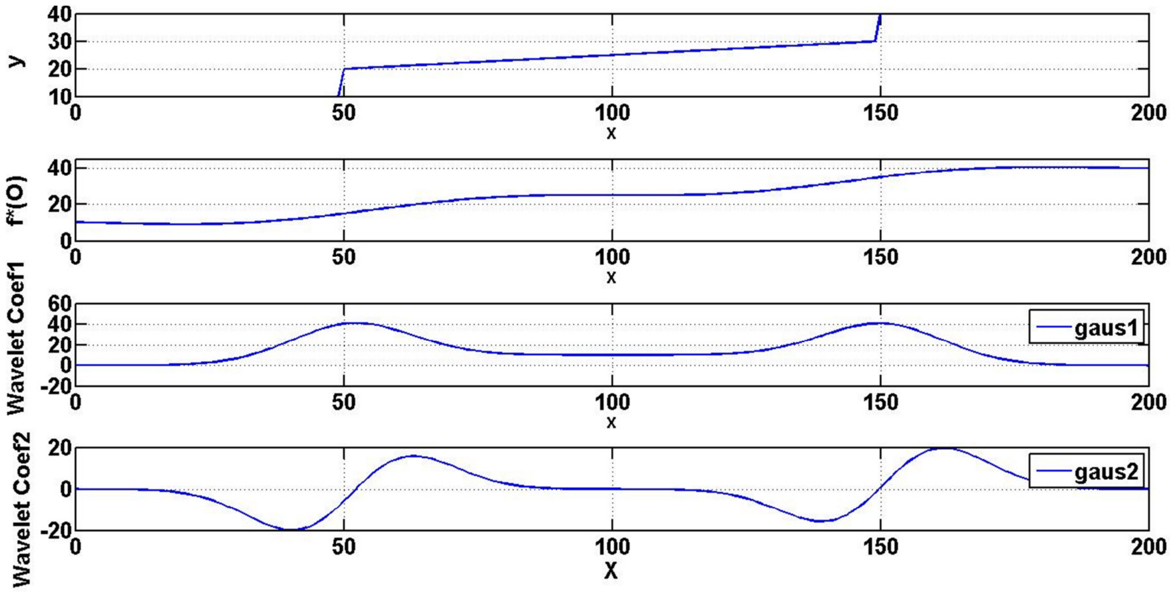

Figure 5-6. The wavelets coefficients at first level of decomposition of a signal with singularity (upper part) using gaus1 and gaus2 base functions (after Mallat and Hwang 1992).

At this point, important questions are raised concerning which wavelet base function to use and how to choose the number of vanishing moments for singularity detection. The wavelet base function used for singularity detection must guarantee that modulus maxima exist at all wavelet coefficients at the singularity point. It must also guarantee that these modulus maxima belong to a maxima line that propagates a finer scale. Mallat and Hwang (1992) showed that the Gaussian derivative wavelet base function can satisfy these conditions and is the best candidate base function for singularity detection. In previous sections, wavelets with a larger number of vanishing moments are discussed as having the advantage of being able to estimate the Lipschitz exponent by exterminating the polynomial signal. Unfortunately, this process increases the number of modulus maxima. To reduce the number of necessary computations it is therefore necessary to keep as few vanishing moments as possible. Cycle slips in GPS signals are typically the more interesting singularities in the signal. They are most often combined with other GPS errors such as ionospheric error, which has the same behaviour as a low order polynomial. The wavelets that correspond to the second derivative of the Gaussian will therefore be the preferred wavelets.

At this point the continuous wavelet transform zooming property can be introduced through the scale of the wavelet transform, or the "zoom". This is one reason why wavelet transform is useful for detecting singularities. Consider Figure 5-7, where the Gaussian wavelets with two vanishing moments are used to analyze a signal with three step singularities. The wavelet transform modulus maxima are computed using fine/small scales to coarse/large scales. The wavelet zooming property allows for focusing in or out on the signal by detecting the overall changes in the signal at coarse scales, while the signal's fine structure is detected in the fine scales. As seen in Figure 5-7, coarse scales (Scales 8 and 16) have only a few wavelet modulus maximum coefficients that correspond to the points where the signal has relatively large overall changes. Furthermore, a large number of wavelet modulus maximum coefficients corresponding to major changes and minor changes in the signal are found in the fine scale. It should be noted that the wavelet modulus maxima coefficients should fall in the wavelet filter width or the cone of influence through scales. This simply means that as the scale increases the width of the wavelet base function support enlarges. Accordingly, for a wavelet base function ψ, assume that ψ is supported between $[-C, C]$ where $C \in \mathbb{R}$ and the function ψ is compactly supported at each scale s between $[-C_s, C_s]$. Then, wavelet modulus maxima of singularity at point v must fall in the range of $[v - C_s, v + C_s]$. Another interesting observation is the way in which wavelet coefficients differ across scales. In cases of singularities due to noise, the values of the wavelets modulus maxima decrease as the scale increases. However, for the singularity at epochs 150, 400 and 650, the value of wavelet modulus maxima increases as the scale increases. This characteristic will be used in the next section to distinguish modulus maximum corresponding to singularity and noise.

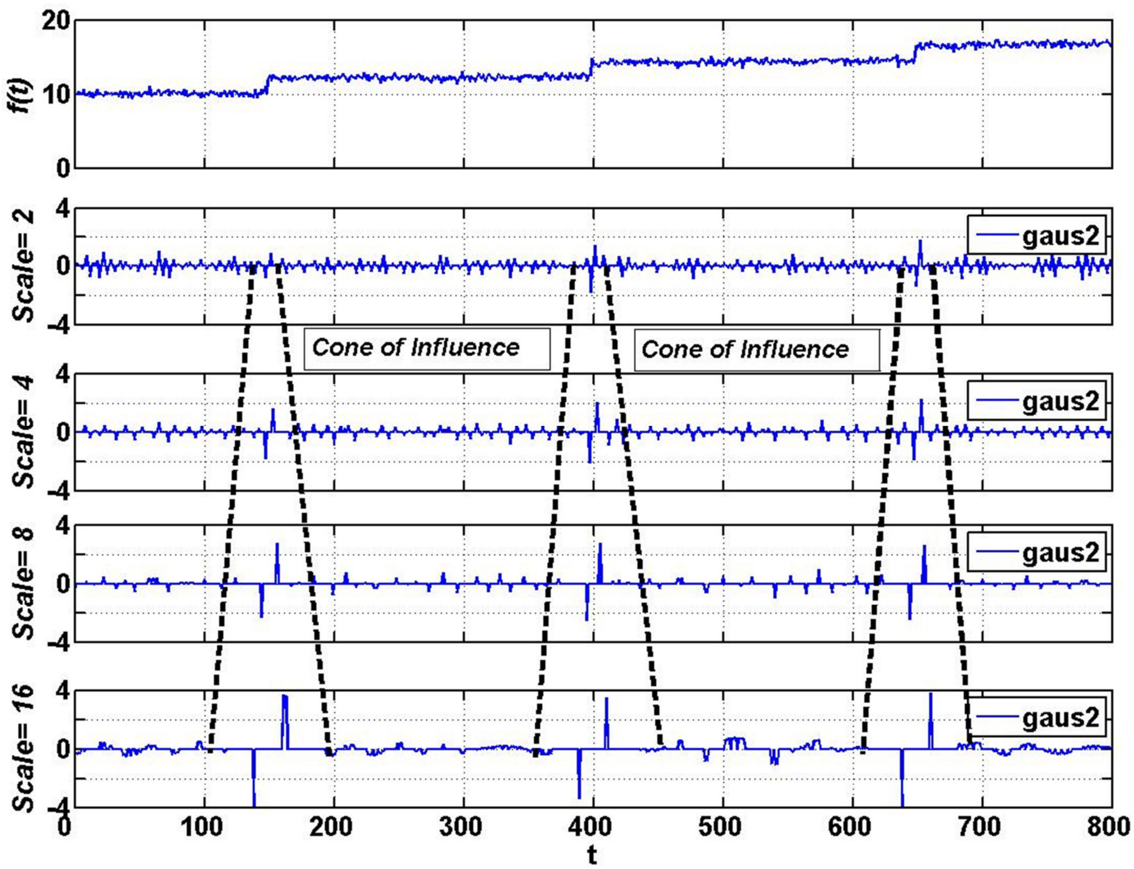

Figure 5-7. The structure of wavelets modulus maximum at four levels of decomposition when singularity occurs (upper part) using gaus2 base functions.

5.4 Multi-scale Cycle Slip Detection and Estimation

It can be said now that all irregularities can be found among the modulus maxima of the wavelet transform at fine scales. This does not imply that all local maxima at fine scales correspond to an irregularity, but rather that at this point the number of coefficients can be reduced by retaining those that are due to singularity and eliminate the rest. With the help of previous sections, a new wavelet technique is proposed to detect and mitigate cycle slip. The first step in this technique is to set up a test quantity to reduce the time varying errors. This can be accomplished by linearly combining the carrier phase measurements with code. At this point cycle slips are buried in noise and can sometimes be difficult to separate from noise, especially under a low signal to noise ratio. Wavelet coefficients for those test quantities are computed and special techniques are applied to reduce noise and retain singularities. Subsequently, cycle slip is detected using modulus maxima propagation and the concept of cone of influence. Finally, cycle slips are estimated using Lipchitz Regularity. As described in Figure 5-8, the proposed technique consists of four main components:

1- Signal Preparation
2- Noise Reduction/Elimination
3- Multi-scale Singularity Detection
4- Singularity Estimation

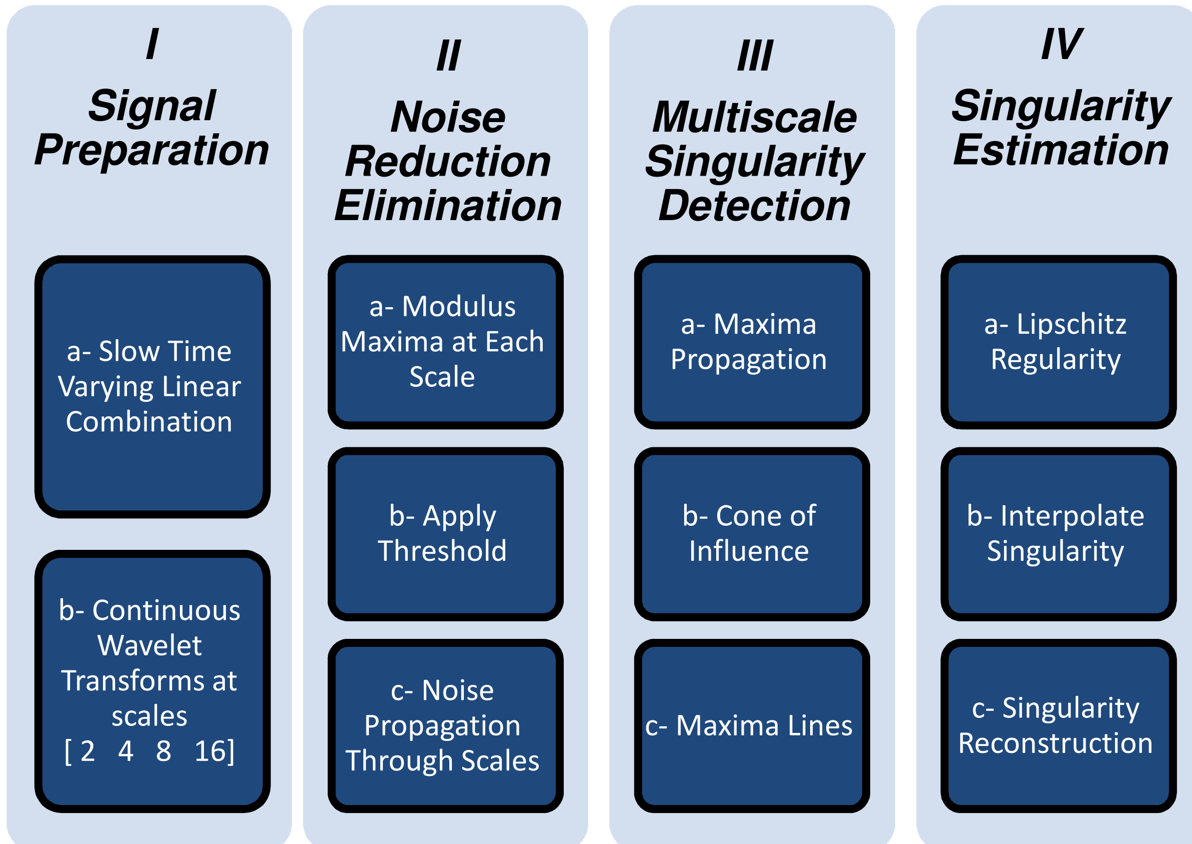

Figure 5-8. Multi-scale Cycle Slip Detection and Estimation Technique

5.4.1 Signal Preparation

Cycle slip is a sudden jump in the carrier phase observables, which is always combined with a polynomial trend due to the geometric distance between the receiver, the satellite, and errors. Equation (5-13) shows the mathematical model for carrier phase observation (Grewal et al., 2007) where carrier phase ($\lambda\phi$) and pseudo-range (ρ) measurements, geometrical range (p), $d_\phi$and $d_\rho$represent the noise in both carrier and code measurements, tropospheric error (d_{trop}), orbital error (d_{Ephem}), satellite and receiver clock errors (cdt, cdT) and ionospheric error (d_{ion}).

$$\lambda\phi = p + cdt - cdT - d_{ION} + d_{TROP} + d_{EPHEM} + d_{\phi} + \lambda N \quad \textbf{(5-13)}$$

The first step in cycle slip detection and estimation is to set up a test quantity to eliminate the geometrical trend (p) and reduce the time varying errors. This can be done by linearly combining the carrier phase measurements with code measurements ρ (Equation (5-14)) in the same frequency, i.e. C/A code and phase in L1, or with the carrier phase at different frequency, i.e. carrier phase measurements in both L1 and L2 frequency. This linear combination must be slowly time varying so that a jump in this function can indicate the occurrence of cycle slip.

$$\rho = p + cdt - cdT + d_{ION} + d_{TROP} + d_{EPHEM} + d_{\rho} \quad \textbf{(5-14)}$$

The proposed multi-scale methodology is tested on the Code minus Carrier combination (CmC) and Phase minus Phase (PmP) combinations. CmC observables are computed by subtracting Equation (5-13) from Equation (5-14) at the same frequency in L1 and L2, while PmP observables are computed by subtracting the carrier phase measurements at L1 and L2 (Equation (5-14)) from each other. The proposed technique can also be applied to any linear combination to detect cycle slips, i.e. double difference, Melbourne-Wubbena. The outcome of the linear combinations is slowly time varying observables that consist of a linear trend or low order polynomial trend that can be removed by the wavelet base function as shown in the previous sections.

The next step is to compute the wavelet coefficient using the Gaussian wavelets with two vanishing moments at different scales from fine to coarse. The continuous wavelet transform is computed in a dyadic scale $\{2^j\}_{j\in\mathbb{Z}}$ to simplify the numerical calculation.

The wavelet transform is computed up to scale 16 to separate noise from singularity as explained in the next section.

5.4.2 Noise Reduction/Elimination

This section begins with computing the modulus maxima. The modulus maxima corresponding to singularity and noise are computed at scales 2, 4, 8 and 16. The propagation of singularities between the wavelet levels of decomposition is different from the propagation of noise. As previously discussed, wavelet coefficients modulus maxima of the singularities are increased when propagated through scales. This indicates that the corresponding singularities have negative a Lipschitz exponent and reflect a large variation in the signal. However, because there is a decrease in the amplitude of the local maxima produced from noise when propagated through scales a negative singularity of white noise occurs. As a result, the amplitude of wavelet coefficient modulus maxima is checked between scales and singularities as then separated from noise. For example, when the amplitude of wavelet modulus maxima increases rapidly while the scale decreases it suggests that the corresponding singular point has a negative Lipschitz regularity. Therefore the singularity of these wavelet coefficients modulus maxima is considered a white noise and should be eliminated. Otherwise, if the wavelet coefficients modulus maxima are increased when scales are higher, the modulus maxima reflect true singularities. It is worth mentioning that by increasing scales, the Signal-to-Noise Ratio (SNR) is increased and as such, the level of decomposition is raised (scale 16). Because some small scales exist where the SNR is relatively low, the wavelet coefficients modulus maxima are mostly dominated by noise and as a result are difficult to use at that scale to detect the signal.

Although this technique will eliminate most singularities due to noise, other singularities due to noise can still propagate through scales and be seen as true singularities. These points have low amplitudes, which make them easy to identify and remove with thresholding. Based on the scale and the signal-to-noise ratio, a threshold is computed from Equation (5-15) to remove these points (Zhao et al., 2000). This threshold will be used as a keep or kill function, meaning that any value above this threshold is kept in the wavelet coefficients modulus maxima and anything lower than this value are set to zero.

$$T_0 = \frac{log_2(1 + 2\sqrt{N})}{j + Z}.K \qquad \textbf{(5-15)}$$

Where *N* is noise power, *j* is the largest scale selected, *Z* is a constant, let it be 14 and *K* is the maximal amplitude of modulus maxima at the level of decomposition in hand.

5.4.3 Multi-scale Singularity Detection

Connecting modulus maximum across scales is necessary in order to identify true singularities from unwanted ones. At coarse scales it is easier to distinguish modulus maximum corresponding to important singularities from those deemed less important. At fine scales the spatial position of the modulus maximum is good with respect to the position of the edges in the signal. The main target of this section is to identify the modulus maxima at fine scales that correspond to modulus maxima at coarse scales. This can be accomplished by connecting the modulus maxima that corresponds to similar features in the signal across scales. This relationship allows the multi-scale singularity detector to have accurate localization and detection performance. Another motivation for relating modulus maximum across scales is to estimate the local Lipschitz regularity of the modulus maxima. In this section a connection procedure is proposed to link the modulus maxima that reflect true singularities through scales.

The proposed connection procedure requires two main steps. The first step is to identify the set of modulus maximum of the wavelet transform that can be connected across scales. This modulus maxima connected curve in the time-scale space is the maxima line. This step is based on the sign of the modulus maximum and its location. Any modulus maximum that is considered in the connection procedure should follow the next two conditions:

1- The sign of modulus maxima cannot change between scales.
2- The modulus maxima should fall in support of the wavelet base function (C_s), cone of influence, at each scale.

These conditions imply that for any modulus maxima $Wf(v_1, s_1)$ at point $v_1$in scale $s_1$to be included in the connection procedure, there must be corresponding modulus maxima $Wf(v_0, s_0)$ at a finer scale $s_0$that satisfy the following two equations:

$$sign(Wf(v_1, s_1)) = sign(Wf(v_0, s_0)) \tag{5-16}$$

$$v_1 > v_0 - C_{s_0} \quad \text{or} \quad v_1 < v_0 + C_{s_0} \tag{5-17}$$

The outcome set of the previous connection step is typically redundant modulus maxima wavelet coefficients. The next step is to apply a few conditions based on the behaviour of wavelet modulus maxima when propagated through scales to remove the redundancy in the set of possible connections. These conditions are as follows:

3- Two maxima lines of opposite sign cannot cross.
4- The amplitude of the modulus maxima at the coarse scales should be larger than the amplitude at the finer scale.

5.4.4 Singularity Estimation

At this point the modulus maxima that correspond to noise and unwanted singularity should be removed and the remaining modulus maxima values should reflect a true singularity or cycle slip. In addition, the location of cycle slip can be computed from the convergence of the connected modulus maxima through scales. However, the amplitude of the local maxima is decreased by the effect of noise especially in the first scales. At the location of true singularity, the signal has a positive Lipschitz exponent while the noise has a negative Lipschitz exponent. Accordingly, if a signal has a localized singularity with amplitude larger than the noise, the magnitude of the modulus maxima of the true singularity is slightly affected at coarse scale due to noise reduction through scales. But, at fine scales the amplitude of the modulus maxima is decreased due to the effect of the noise negative Lipschitz exponent. This directly affects both the modulus maxima of the singularity and any constructed signal from these singularities. Therefore, the amplitude of the singularities at fine scales must be corrected for the noise effect before the reconstruction stage. To compute the corrected amplitude for the modulus maxima the Lipschitz regularity of the singularity through scales should be computed. This is accomplished by estimating the best Lipschitz exponent α that matches the decay of the modulus maxima at scales larger than 2^2 and 2^1 using Equation (5-10). In order to keep the same wavelets decay through scales, the estimated Lipschitz exponent α is used to interpolate the modulus maxima values from scale 2^3 to scale 2^1. This non-linear interpolation algorithm retrieves an approximation of the cycle slip of the original signal.

Finally, the interpolated modulus maxima coefficients at scale 2^1 are used to synthesize the true singularities in the signal using inverse wavelet transform to compute the corrected values of singularities. These values are the cycle slip error and are used to modify the original GPS signal. It should be noted that Mallat and Hwang (1992) used the Lipschitz exponent to detect an estimate of the singularity. While in the proposed technique, the Lipschitz exponent is used only to estimate the singularity and not detect it. This is because Mallat and Hwang (1992) computed the Lipschitz exponent in the detection process to determine whether the singularities had negative Lipschitz exponents. This means that the modulus maxima have amplitudes that decrease strongly when the scale decreases. However, this step is already conducted at the detection stage by comparing the amplitude of the modulus maxima between fine and coarse scales.

5.5 Assessment of the Multi-scale Algorithm

5.5.1 GPS Data with Simulated Cycle Slips

To demonstrate the performance of the proposed multi-scale similarity detection technique, GPS L1 and L2 pseudo-range and carrier phase are collected using two different receivers. Both the Novatel's Propak-DL-4-RT2 and Trimble R8 receivers are used to collect GPS data as explained in Chapter 3. In this section only seven satellite measurements for 3000 seconds duration are used for cycle slip detection and removal, where a clear satellite path with no jumps or gaps was detected. Different artificial cycle slips are simulated and added to all the GPS measurements at both L1 and L2 as seen in Table 5-1.The proposed multi-scale procedure in this chapter is used to detect, estimate and remove the cycle slips over three test quantities at each satellite measurements; namely Code minus Carrier in L1 (CmC1), Code minus Carrier in L2 (CmC2) and Phase1 minus Phase2 (PmP).

Table 5-1. Simulated cycle slips

Epoch	750	1000	1250	1500	1750	2000	2250	2500	2750	3000
PH1	0	1	0	2	0	3	0	2	0	0
	0	0.19	0	0.38	0	0.57	0	0.38	0	0
PH2	1	1	3	1	2	0	2	0	1	0
	0.244	0.244	0.732	0.244	0.488	0	0.488	0	0.244	0

First, the test quantity is decomposed using continuous wavelet transform at scales 2, 4, 8 and 16 resulting in the wavelets coefficients at each scales. Figure 5-9 and Figure 5-10 demonstrate the result of the proposed technique after applied to GPS data collected by the Novatel receiver. Figure 5-9) identifies the wavelet transform coefficients at the four scales using Gauss with two vanishing moment base function for CMC1 test quantity. The wavelets zooming property for singularity can be seen from the figure as the wavelets amplitude increases through scales for singularities at epochs 500, 1000, 1500, 2000 and 2500 and decreases for noise. Afterwards, the modulus maxima are computed and connected between scales using the propped multi-scale procedure (Figure 5-10-c to Figure 5-10-f). Figure 5-10-c shows the modulus maxima at scale 2^1 after removing the singularities due to noise using the multi-scale procedure part II-b and II-c (Figure 5-8). This is achieved in two steps: first any modulus maxima under the threshold mentioned in Equation (5-15) at each scale are removed. Second, all the modulus maxima that have the amplitude reduced through scales are deleted. After applying the previous step, the remaining modulus maxima are mainly due to real singularity and sharp noise. The final step is to keep the modulus maxima values due to real singularities and remove any unwanted singularities by looking at the evolution of the local maxima amplitude through scales. Any local maxima that follow the next conditions are kept in multi-scale singularity detection procedure. The conditions are as follows:

1- Each maxima point must propagate through scales and fall in a maxima line. (Figure 5-10-e). Any maxima point that does not follow a maxima line is removed.
2- Each maxima point must fall in the cone of influence (Figure 5-10-f). Any maxima point that is found outside the cone of influence is removed.

It can be seen from Figure 5-10-f that all the unwanted singularities are removed effectively by the propped multi-scale procedure and the remaining singularities are due to true cycle slips. The detection algorithm achieved the same outcome when applied to the three test quantities at each satellite for both GPS receivers. Table 5-2 shows the total number of cycle slips in each test quantity and the error in cycles for the recovered cycle slips using the multi-scale technique. It can be seen that all the cycle slips are detected and estimated correctly and the error in the estimation did not exceed the 0.15 cycle for CmC test quantities and 0.05 cycles for PmP. It should be mentioned that the signal- to - noise ratio for the test quantities is around 45.

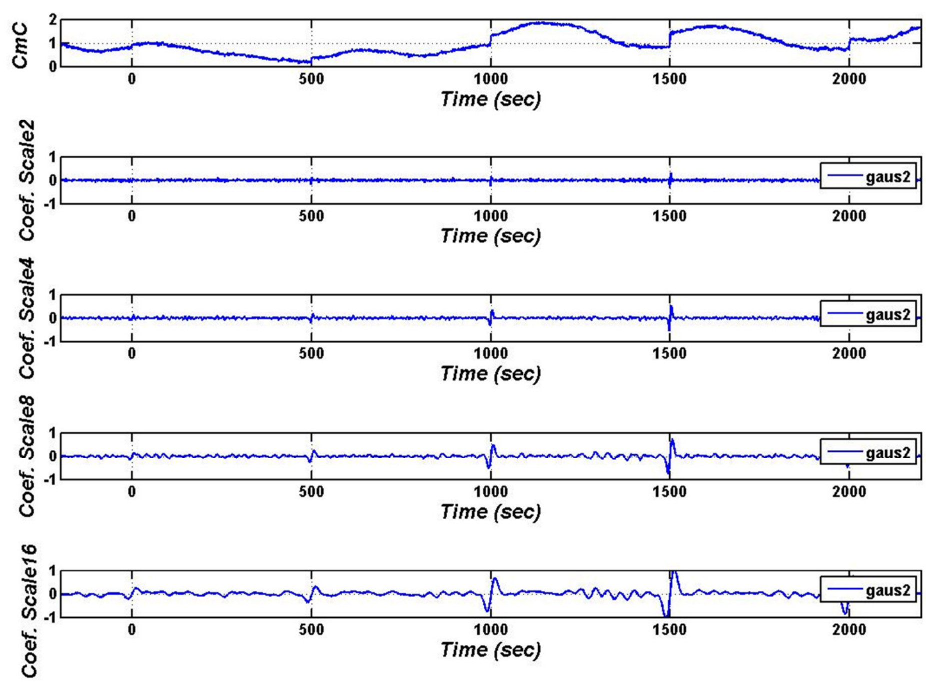

Figure 5-9. Wavelets zooming property transforms coefficients at scales 2, 4, 8 and 16.

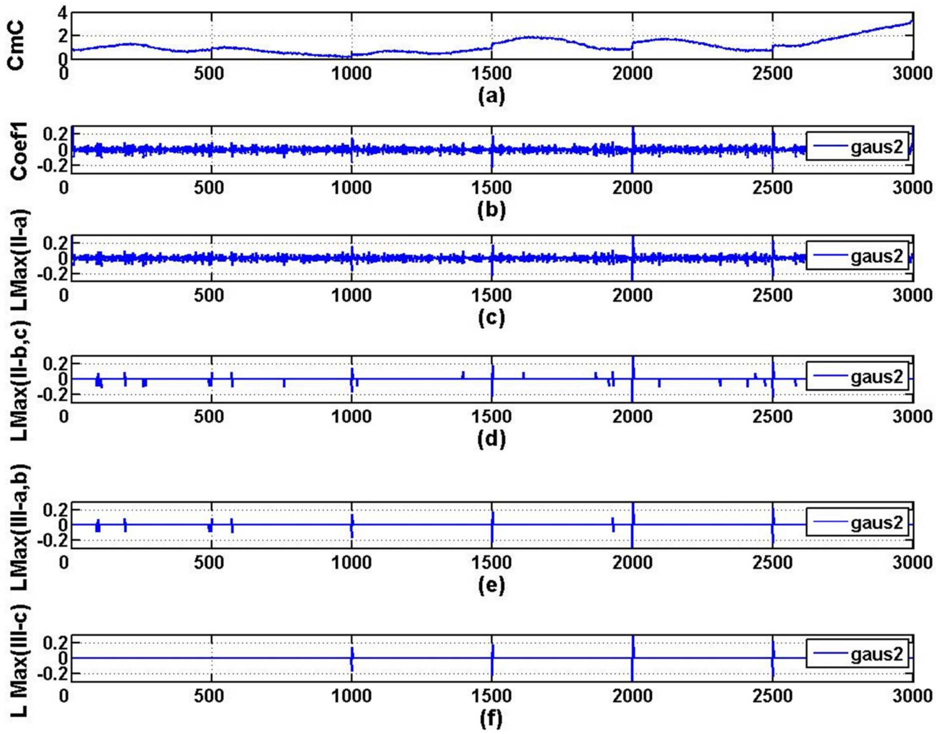

Figure 5-10. The wavelets coefficients and the wavelets local maxima at scale 2^1 when applying each step of the multi-scale technique over the CMC1 test quantity.

Table 5-2. The number of detected and recovered cycle slip and the error range for each reconstructed slip.

Test Qt.	No. Slips	0-0.05	0.05-0.10	0.1-0.15
CmC1	56	20	29	7
		35.71%	51.79%	12.50%
CmC2	98	32	49	17
		32.65%	50.00%	17.35%
PmP	112	112	0	0
		100.00%	0.00%	0.00%

5.5.2 GPS Data with Simulated Cycle Slips and Added White Noise

In the previous section, the multi-scale singularity detection and estimation technique are tested over a signal with relatively high SNR. The result shows the ability of the proposed technique to detect cycle slip in both CmC and PmP test quantities. It is not clear up to this point what the performance of the proposed technique will be under low SNR. In this section the same test quantities from the previous section are used but with added white noise. The CmC and PmP observables are tested under SNR starting from 15 up to 50. Each test quantity is passed to the proposed multi-scale singularity detection algorithm to detect and estimate the cycle slip location and magnitude under different SNR. Table 5-3 shows the number of detected singularities in each test quantity and the detection percentage with respect to the total number of cycle slips. Cycle slips are simulated at all the seven satellites that are found at each of the GPS receivers as per Table 5-1. It can be seen from the figure that the multi-scale procedure can detect all singularities in both CmC1 and CmC2 test quantities when the SNR is higher than 20. In the case of a CmC test quantity that has an SNR lower than 20, the signal is buried in noise and it is hard to distinguish the singularity from the noise. However, the proposed multi-scale singularity technique detected all the singularities in the PmP test quantity that has an SNR over 15. This is due to the fact that the noise magnitude in the case of the CmC test quantity is in the decimetre level, while in case of PmP test quantity the noise magnitude is in millimetres level.

Table 5-4 shows the error in the estimated cycle slips for the CmC test quantity when compared with the simulated cycle slips. It can be seen from the table that most cycle slips are correctly estimated with an error of less than 0.1 cycle which is equal to 2.0 centimetres for SNR higher than 35.

Table 5-3. The number of detected and recovered cycle slips in all test quantity under SNR from 15 to 50.

Test Qt. /SNR	No. Slips	15	20	25	30	35	>40
CmC1	56	10	48	56	56	56	56
		17 %	85%	100%	100%	100 %	100 %
CmC2	98	8	80	97	98	98	98
		8%	81%	99%	100%	100%	100%
PmP	112	112	112	112	112	112	112
		100%	100%	100%	100 %	100%	100 %

In most cases of signals with SNR range between 25 and 35, the error can reach 0.4 cycles. In addition, an error that is higher than 0.40 cycles occurs in the estimation process but with a small percentage. The error in the estimated cycle slips in the case of CmC test quantity with SNR lower than 25 can reach one or two cycles and this destroys the whole process as the cycle slip can be as much as one cycle. It can be concluded from this table that it is better to use the multi-scale singularity technique to safely detect cycle slips and the Lipchitz regularity process to safely estimate cycle slips for CmC test quantities that have SNR larger than 30. Furthermore, the multi-scale technique can be used to detect and estimate cycle slip in PmP test quantity with low SNR.

Table 5-4. Estimated cycle slip error range for each reconstructed slip in CmC test quantity under SNR from 20 to 60.

Error/SNR	Error in cycle				
	0-0.10	0.10-0.20	0.20-0.30	0.30-0.40	>0.40
20	29%	14%	29%	3%	26%
25	23%	26%	17%	31%	3%
30	41%	29%	15%	10%	5%
35	46%	31%	11%	6%	6%
40	52%	37%	8%	3%	0%
45	58%	36%	4%	2%	0%
50	68%	28%	4%	0%	0%

5.6 Summery

A new multi-scale singularity detection technique combined with Lipchitz exponent estimation procedure to detect and estimate cycle slips in GPS measurements is introduced. The proposed technique can detect the location of cycle slip in noisy measurements and rejects the fault singularities caused by noise. The performance of the proposed technique is evaluated and tested over GPS code minus carrier and Phase1 minus Phase2 measurements where different cycle slips are added to the measurements. Also, the performance of the proposed technique is tested over CmC test quantities under SNR range from 20 to 50. All the simulated cycle slips in CmC test quantities with SNR bigger than 30 are effectively detected by the proposed technique. The error in the estimation process is less than 0.1 cycles most of the time.

Chapter Six: Multi-resolution real-time (MRRT) code-smoothing technique

6.1 Introduction

In this chapter, an inovative code-smoothing technique is used, namely, Multi-resolution Real-time (MRRT) Code-smoothing technique. This technique is used in real-time scenarios to mitigate multipath error (medium to high-frequency) and noise (high-frequency) and retain the ionospheric error (low-frequency) untouched in the mitigation procedure. The proposed MRRT technique is superior to other techniques found in the literature, since it can effectively remove the multipath and noise in real-time scenarios and retain the smoothed code unbiased with low variance. Furthermore, the MRRT procedure is easy to use and resolves the main obstacles that face the real-time mitigation, which are:

- Elimination of the integer ambiguity part from the mitigation process.
- Elimination of the high-frequency noise in both single and dual-frequency case.
- Elimination of the time delay lag that is introduced in previous CsC techniques.
- Minimization of the boundary problem, which is the main problem in the real-time mitigation procedure.
- Minimization of the smoothed code bias without any significant increase in the standard deviation.
- Reduction of the aliasing effect in the iteration process.
- Identification of the exact wavelet parameter that can be generally used in the mitigation process.

6.2 Code minuses Carrier observable

The common errors in both carrier phase ($\lambda\phi_M$) and pseudo-range (ρ_M) measurements are the satellite and receiver clock errors (cdt, cdT), tropospheric error (d_{Trop}), orbital error (d_{EPHEM}). The ionospheric error (d_{ION}) is the same in both measurements but different in sign. The mathematical model for both code and carrier can be seen in Equation (6-1) and (6-2) (Grewal et al., 2007) . MP_ϕ , d_ϕ and MP_ρ , d_ρ represent the multipath and noise in both carrier and code measurements.

$$\rho_M = \rho + cdt - cdT + d_{ION} + d_{Trop} + d_{EPHEM} + MP_\rho + d_\rho \qquad \textbf{(6-1)}$$

$$\lambda\phi_M = \rho + cdt - cdT + \lambda N - d_{ION} + d_{Trop} + d_{EPHEM} + MP_\phi + d_\phi \qquad \textbf{(6-2)}$$

While the noise and multipath error in the carrier phase measurements is one order of magnitude lower than code measurements, the carrier phase measurement contains unknown integer ambiguity λN value that needs to be estimated in the estimation procedure. The code measurement is noisier than carrier phase but does not contain the ambiguity part, which if correctly estimated results in a better performance in case of single frequency positioning. The remaining errors in the Code minus Carrier (CmC) measurements (Equation (6-3)) are double the ionospheric error ambiguity bias, code and carrier multipath and noise. The code multipath error, which is the major error source, falls in a high to medium frequency band (0.1 to 0.003Hz), while the ionospheric error is in a lower frequency band (0 to 1.2e-4 Hz) (Zhang and Bartone, 2004). The technique used to smooth the code should separate/mitigate the multipath error and minimize the variation of the signal (standard deviation) and keep the corrected signal unbiased. Moreover, the separation between the multipath and the ionospheric error should be made correctly in a real-time scenario; otherwise, the un-separated portion will cause the smoothed signal to be biased.

$$CmC = 2d_{ION} - \lambda N + MP_{\rho} - MP_{\phi} + d_{\rho} - d_{\varphi} \tag{6-3}$$

6.3 Multi-Resolution Real-time (MRRT) technique.

In this chapter, a new multi-resolution approach (MRRT) based on a wavelet de-trending technique is introduced to isolate medium to high rate errors i.e. ionosphere error from the multipath and noise. Given that the ionosphere error has a low-frequency pattern, the wavelet transform approach is applied to the CmC measurements to isolate ionosphere errors at low levels of decomposition leaving the high to medium frequency errors at high levels of decomposition. In real-time scenarios the corrected epoch "T" is the last epoch in the CmC measurements. To achieve the real-time capability, a smoothing window with size τ is passed to the MRRT technique for error mitigation. The length of the window can vary from the largest wavelet width to the whole length of the signal. A window size of 100 seconds is used since it is the window size that is issued by the WAAS committee for real-time smoothing.

The CmC signal is decomposed into approximation and details using the successive low-pass/high-pass filter banks at different levels of decomposition. High to medium frequency errors (multipath and noise) are separated at the details part of the decomposition and the ionospheric error is kept in the approximation part along with any biases (i.e. ambiguity term). Accordingly, the objective of this decomposition is to separate the main error part (multipath and noise) in the details coefficients from level 1 to M ($d_n^{1:M}(t)$) and the low-frequency error and bias (ionosphere and ambiguity) are kept in the approximation part c_n^M where M is the level of decomposition that effectively separates these errors using a particular wavelet base function (Figure 6-1). The choice of wavelet base function and level of decomposition is discussed in the following sections.

$$CmC = \underbrace{\boxed{2d_{ION} - \lambda N}}_{c_n^M} + \underbrace{\boxed{MP_\rho - MP_\phi + d_\rho - d_\varphi}}_{d_n^{1:M}(t)} \qquad \textbf{(6-4)}$$

The multipath and noise error component (ξ) are estimated by syntheses the separated wavelet coefficients ($d_n^{1:M}(t)$) after the elimination of the low-frequency error and bias by setting the approximation coefficients (c_n^M) to zero (Equation (6-5)). This truncation procedure is referred to as the kill approximation thresholding procedure. The estimated error is directly applied to the code measurements (Equation (6-1)) in real-time scenarios smoothing the code at its current epoch (Equation (6-6)).

$$\xi = \sum_{m=1:M} \sum_{n \in Z} d_n^m \psi_{m,n}(t) \qquad \textbf{(6-5)}$$

$$CmC = 2d_{ION} - \lambda N + MP_\rho - MP_\phi + d_\rho - d_\varphi \qquad \textbf{(6-6)}$$

The innovation of the MRRT technique is in its ability to isolate the multipath errors without touching the ambiguity part as shown in Equations (6-4), (6-5) and (6-6). Moreover, the noise part is included in the upper levels of decomposition (details) and removed in the mitigation procedure without causing any real-time time lag.

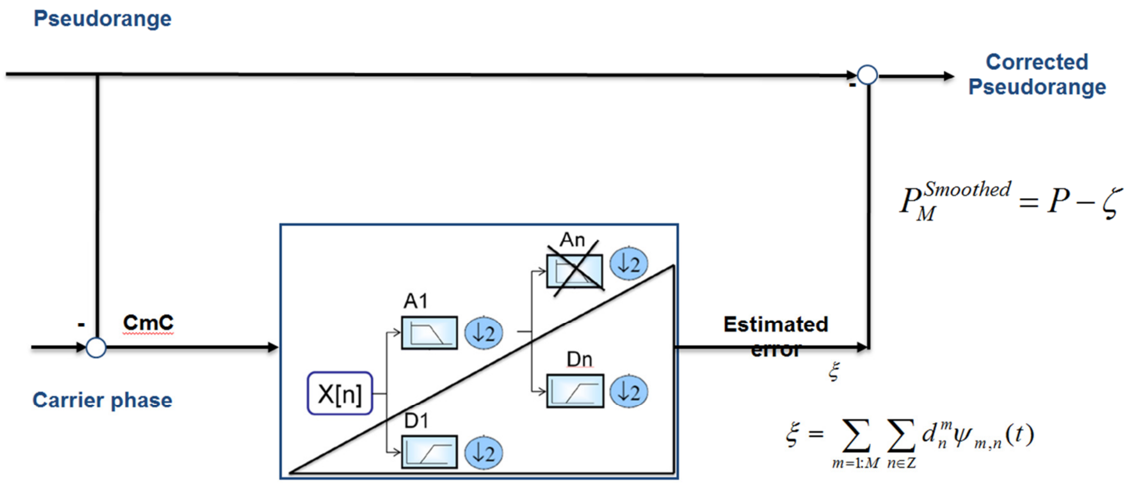

Figure 6-1. Multi-Resolution Real-time (MRRT) technique.

Figure 6-2 shows the CmC measurements for satellite No. 11 and the smoothed version using both hatch filter and the proposed MRRT technique. It can be seen from the figure that the MRRT technique is more suited to real-time variations in the signal than the hatch filter. The MRRT technique achieves three main objectives of mitigation:

- Eliminate of the integer ambiguity part from the mitigation process.
- De-noise the high-frequency part in both single and dual-frequency case.
- Eliminate of the time delay lag that is introduced in previous CsC techniques.

Zhang and Bartone (2004) applied wavelet analysis after estimation of the ambiguity bias by computing the mean of the CmC measurements for each epoch (time window) in real-time scenarios. Applying the wavelet methodology in this way is time consuming and can cause more bias to the code measurements for small window sizes.

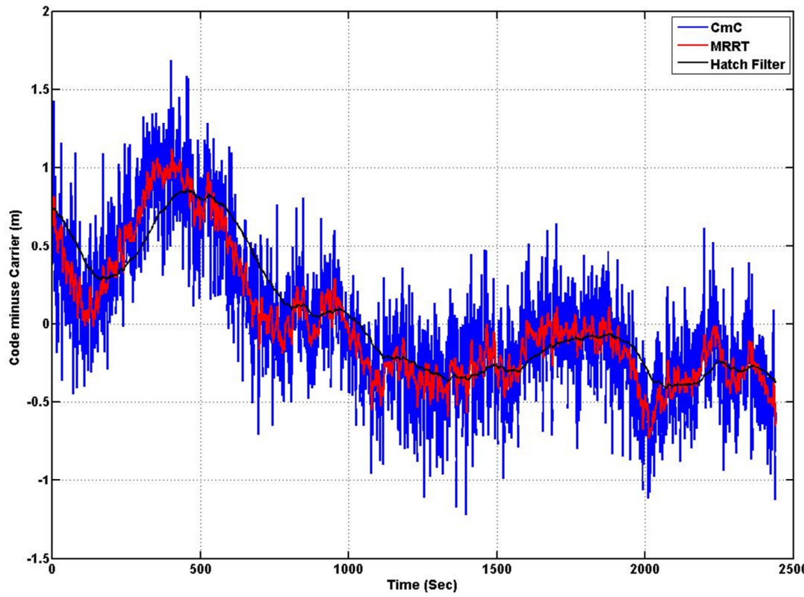

Figure 6-2: Smoothing using Hatch filter "black line" and MRRT technique "red line".

Zhang and Bartone (2004) estimated that the multipath error in cases of ionosphere linear combination from the approximation part at the first level of decomposition could effectively mitigate the multipath error. But, in this case the noise magnitude is increased dramatically and kept in the details part of the first level of decomposition, which will be directly reflected to the smoothed code. However, in the MRRT technique the noise is estimated in the details part and eliminated from the code measurements in case of single frequency. Single frequency users can use the proposed MRRT to mitigate medium to high-frequency part such as multipath and the high-frequency part of the ionosphere. However, dual-frequency users can remove the ionospheric error by combining the signals at L1 and L2 (ionosphere linear combination) and use the MRRT to mitigate the multipath error. In this chapter the MRRT is applied to single frequency users only that use L1 code and phase.

6.4 Multi-Resolution Parameters Assessment

6.4.1 Base function and scale selection

Wavelet analysis depends on several parameters that should be investigated, namely wavelet base function, level of decomposition and the extension padding mode. The key aspect in choosing the wavelet parameters is that the corrected signal remains at zero mean and has a low standard deviation. Since the wavelet approximates the signal, the shape of the wavelet determines the accuracy of the approximation. Forty discrete wavelet base functions (Table 6-1) are introduced to the wavelet de-trending technique for error isolation and removal at levels of decomposition from 1 to 10.

Table 6-1: Wavelet base functions

No.	Base	No.	Base	No.	Base	No.	Base	No.	Base	No.	Base	No.	Base	No.	Base
1	Sym6'	6	'Sym5'	11	'DB7'	16	Sym10'	21	Bior10'	26	'Haar'	31	Bior7'	36	Bior4'
2	Coif4'	7	'DB5'	12	'Sym9'	17	Bior11'	22	'DB4'	27	Sym1'	32	Bior6'	37	Coif2'
3	Sym8'	8	Bior13'	13	Bior12'	18	'DB6'	23	'DB2'	28	Bior1'	33	Bior3'	38	Coif1'
4	Sym7'	9	'DB3'	14	Bior14'	19	Bior15'	24	'Sym2'	29	Coif3'	34	Bior5'	39	Bior8'
5	'DB8'	10	'Sym3'	15	'DB10'	20	'Sym4'	25	'Bior9'	30	Coif5'	35	Bior2'	40	'DB9'

6.4.2 Boundary problem

In real-time scenarios, the corrected observation is at the last epoch of the measurements set, which is most affected by the way the wavelets treat the last epoch (Boundary problem). The main factor that affects the boundary error is the filter width. A base function with small filter width will cause a minimal boundary error (Walnut, 2002). Therefore, the analysis is made either in one or two iterations; the first iteration is achieved by applying the MRRT technique using all the above factors. The second iteration, a small filter (Haar) up to level six of decomposition is applied to mitigate the high-frequency error without inducing bias to the original signal before applying the MRRT technique using all the above factors. Several schemes exist and they can treat the boundary problem by extending the signal with m-1 samples, where m is the filter length (Gilbert and Neguyen, 1996). Two well-known techniques are investigated in this research chapter, namely the periodization and symmetrisation.

6.5 Evaluation of the MRRT Algorithm over Real-time Data

On November 9th, 2007 an experiment was conducted at the University of Calgary to test the ability of the introduced technique to mitigate multipath error (medium to high-frequency) and noise (high-frequency) in real-time scenario. NovAtel's Probak-DL-4-RT2 receiver and GPS-600-LB antenna were used on the roof of the engineering building as explained in Chapter 3. The data rate was a one-second data interval and the total data number of epochs used in this chapter was 3600 epochs. Single frequency L1 data for three satellites were used in this test scenario. Only the satellite PRN11 data was shown in the analysis since PRN11 was in a lower elevation and multipath error was relatively more significant than other satellites.

During this test, code and phase measurements for PRN11 are passed to MRRT to separate/isolate high-frequency errors as discussed in the previous sections. The MRRT is applied in two different scenarios; the first scenario is achieved by applying the MRRT technique using the 40-wavelet base functions listed in Table 6-1. In this test scenario, two extension modes were used to deal with the boundary problem: periodization and symmetrisation. The MRRT technique is applied at 10 levels of decomposition starting from level 1 to level 10. Each time the MRRT outputs an error estimate for the code measurements. In total, the MRRT technique is applied 800 times for the first case scenario to produce 800 error estimates for the code. These error estimates are compared using their mean and standard deviation (Figure 6-3 and Figure 6-4 left side). The second test scenario is accomplished by applying a preliminary step/iteration to de-noise the high-frequency errors. In this iteration MRRT is applied using Haar base function at level 6 and symmetrisation extension mode. The second iteration was the same as the first test scenario, where MRRT is applied using 40 base functions with two extension modes. The mean and standard deviation for the second case scenario are shown in Figure 6-3 and Figure 6-4 (right side).

Figure 6-3 and Figure 6-4 (left part) show the bias in millimetres and standard deviation in centimetres corresponding to the smoothed code measurements of PRN11 only, as the MRRT technique achieved the same results with all the three satellites. It can be seen from these figures that the periodization extension method (upper part) increases both the bias and standard deviation when compared to the symmetrisation method (lower part). Also, it can be noticed in the symmetrisation part that the bias and standard deviation did not change dramatically except in level 6, where 50% of the standard deviation is reduced and there is no change in the bias value. Moreover, the bias is increased gradually from level 6, while the standard deviation is reduced. In the first iteration, the base function that yields the best bias-std combination is 26-haar wavelet with 3.4 mm bias and 24.6 cm std, while the best base function in the second iteration is 25-Bior9 with 5.12 mm bias and 22.0 std. The second iteration will reduce the bias from 37 mm when the hatch filter is used to 5.12 (87% error reduction) with a small increase in the standard deviation from 18 cm (hatch filter) to 22 (MRRT).

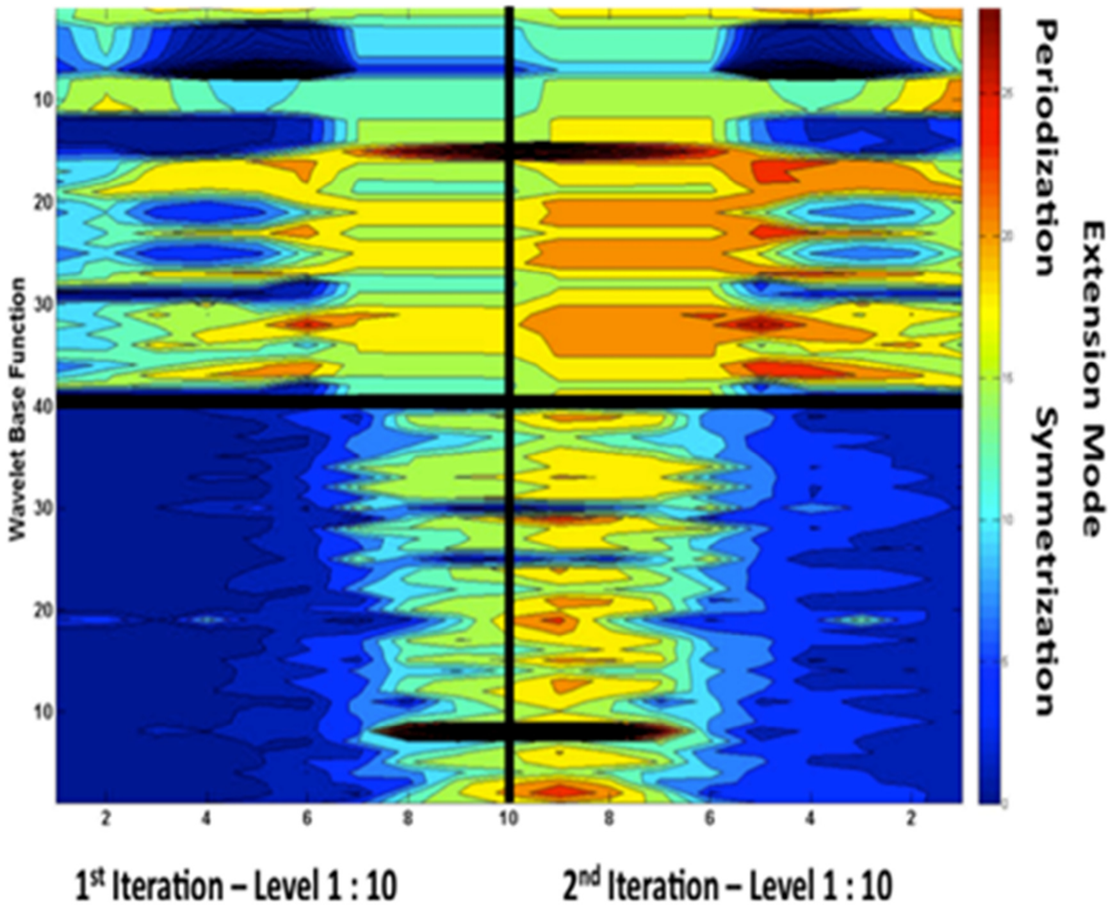

Figure 6-3: The smoothed code bias (mm): Tested factors 40 wavelet base functions, 1 to 10 level of decomposition, two extension modes and one to two iterations.

Zhang and Bartone (2004) not only ignored the boundary effect in the WAVESMOOTH technique, but did so in a way that actually increases this error. The WAVESMOOTH technique is an iteration process that uses the same wavelet parameters twice to mitigate the multipath error.

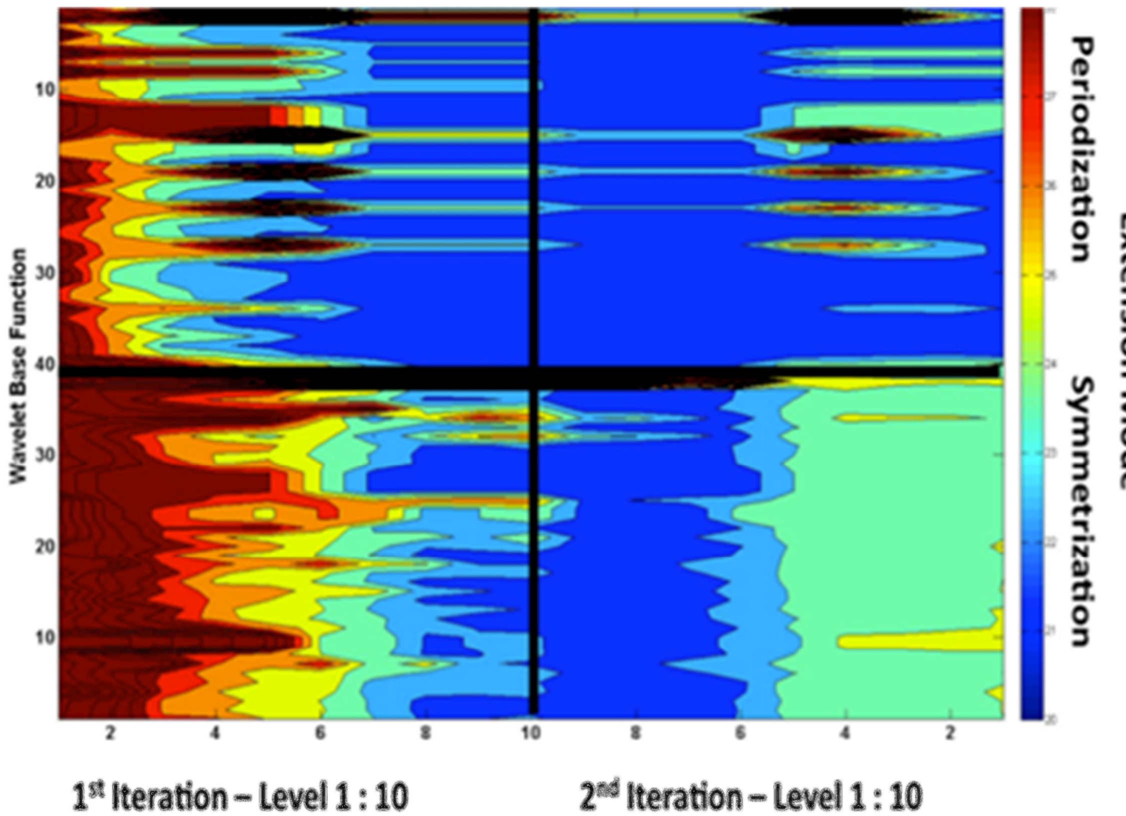

Figure 6-4: The smoothed code standard deviation (cm): Tested factors 40 wavelet base functions, 1 to 10 level of decomposition, two extension modes and one to two iterations.

Applying the wavelet multi-resolution analysis twice should reach a better solution if used properly. As mention previously, the second iteration is made with a totally different wavelet base function (i.e. db, bior) than the first iteration (Haar) and up to the eigth level of decomposition—two levels more than the first iteration. Zhang and Bartone (2004) applied the WAVESMOOTH technique using the same wavelet base function and level of decomposition in iteration one and two and as a result, added more noise to the signal and did not tackle the boundary problem. Figure 6-5 shows the approximation and details of decomposed CmC signal in its second iteration, where the wavelet parameters are the same in both iteration one and two.

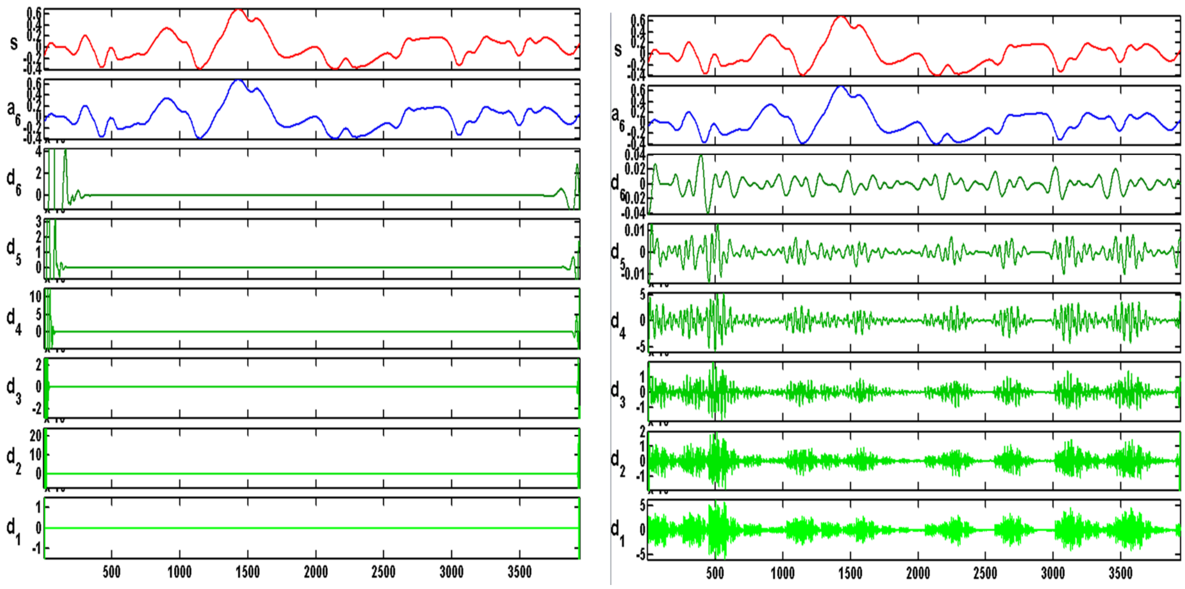

Figure 6-5: The details and approximation coefficients of the signal in the second iteration after using the same wavelet parameters in WAVESMOOTH (left) and MRRT (right).

The figure shows the CmC signal in the upper part as "S", the approximation of the six level "a6" and the details for levels one to six (d1, d2, d3, …, d6). The right side of the figure shows the decomposition using the WAVESMOOTH procedure by appling the same base function in the second iteration and the left side shows the decomposition using MRRT technique by appling different base function to the second iteration. It can be seen from the figure that decomposing the signal using the same wavelet parameters after applying WAVESMOOTH in the first iteration caused an aliasing effect at the boundary of the details (d3, d4, d5 and d6). However, using a different base function minimized the boundary effect. Therefore, application of the WAVESMOOTH technique iteratively with the same wavelet parameters deteriorates the code signal with noise.

6.6 Summary

A new wavelet multi-resolution technique (MRRT) is introduced to separate/mitigate the code multipath error in real-time scenario. The performance of the proposed technique is investigated over real GPS measurements to attain the best base function and level of decomposition. Symmetrisation is determined to be the best extension method to deal with the boundary problem in the real-time code smoothing when compared to periodization extension method. Also, to achieve minimum bias and std. by the proposed MRRT technique, Haar base function should be used first to mitigate high-frequency errors up to level 6. And, Bior9 base function should be introduced iteratively to mitigate medium multipath. Using the proposed technique led to a reduction of 86% in the bias when compared to the hatch filter with a small increase in the standard deviation. The MRRT procedure is easy to use and resolve the main obstacles that face the real-time mitigation, which are:

- Elimination of the integer ambiguity part from the mitigation process.
- De-noised of the high-frequency noise in both single and dual-frequency case.
- Elimination of the time delay lag that is introduced in previous CsC techniques.
- Minimization of the boundary problem, which is the main problem in the real-time mitigation procedure.
- Minimization of the smoothed code bias without any significant increase in the standard deviation.
- Reduction of the aliasing effect in the iteration process.
- Identification of the exact wavelet parameter that can be generally used in the mitigation process.

Chapter Seven: CONCLUSIONS AND FUTURE WORK

This chapter provides the conclusions of this research work, which will focus on a group of developments and deliverables that use multi-resolution aided techniques for GPS signals and signals combination (code minus carrier and double difference carrier) to mitigate inherent GPS measurement errors. The objective of this research thesis was successfully achieved in the development of a number of multi-resolution techniques that can detect and mitigate static GPS-inherent errors such as phase multipath in the double difference domain, code multipath and cycle slip.

7.1 Conclusions

The main goal of this research work was the development and implementation of DGPS error mitigation techniques using multi-resolution methodology. This research work was conducted in several stages with predefined objectives according to Section 1.2. The following sections provide the related research activities and their outcomes:

7.1.1 Phase multipath mitigation

Two different multi-resolution techniques were presented that can be used separately or combined to remove the low to high-frequency DGPS phase errors. The first technique is applied using wavelet as a de-noising tool to tackle the high-frequency errors in the double difference domain and to obtain a de-noised double difference signal that can be used in a positioning calculation. A detailed analysis is also conducted to help choose the best wavelet base function and threshold technique estimator by comparing different wavelet parameters along with different thresholding techniques. Based on the performed analysis it was found that the biorthogonal wavelets are recommended to isolate the correlated error, especially bior3.3 for short baselines and bior3.1 for longer baselines. It was also determined that the median threshold estimator with a soft threshold type shows approximately 50% of the maximum correlation reduction and acts with consistency on short and long baselines.

The second technique discussed in this chapter uses the wavelet technique as a de-trending tool to tackle the low-frequency portion of the double differenced measurements. It was found that the de-noising technique provides consistent results for both short and long baselines. The average bias reduction that can be achieved from the de-nosing technique is in the range of 20-30% and the average RMS reduction is around 30-40%. Moreover, the de-trending technique out-performs the de-noising technique for RMS improvement in short and long baselines. The performance in the de-trending technique is almost three times better than the traditional de-noising technique for bias and RMS reduction.

While the de-trending technique overcame the de-noising technique in the RMS reduction, it failed to offer consistent results for bias reduction. The de-trending methodology performed efficiently in the case of short baselines in both RMS and bias reduction as the average RMS and bias reduction were around 80%. However, for longer baselines the bias reduction is minimal although the RMS reduction is still in the range of 70-80% reduction. It can be concluded that the de-trending technique can reduce the double difference errors dramatically for short baselines. Conversely the de-trending technique can cause a biased solution for long baselines as well as enhance the RMS value showing good statistics for the solution but not enhance the bias to the same level.

7.1.2 Code multipath

A new adaptive wavelet multi-resolution real-time technique (MRRT) is introduced to separate/mitigate the code multipath error in real-time scenario. The performance of the proposed technique is investigated over real GPS measurements to attain the best base function and level of decomposition. It is found that the symmetrisation is the best extension method to deal with the boundary (edge) problem in the real-time code smoothing when compared to periodization extension method. Also, to achieve minimum bias and std. by the proposed MRRT technique, Haar base function should be used first to mitigate high-frequency errors up to level 6. Bior 3.3 base function is done iteratively to mitigate medium multipath in the spectrum domain with localization. Using the proposed technique led to a reduction of 86% in the bias when compared to the hatch filter, with a small increase in the standard deviation. The MRRT procedure is easy to use and resolves the main obstacles that face the real-time mitigation:

- Elimination of the integer ambiguity part from the mitigation process.
- De-noising of the high-frequency noise in both single and dual-frequency cases.

- Elimination of the time delay lag that is introduced in previous CsC techniques.
- Minimization of the boundary problem, which is the main problem in the real-time mitigation procedure.
- Minimization of the smoothed code bias without any significant increase in the standard deviation.
- Reduction of the aliasing effect in the iteration process.
- Identification of the exact wavelet parameter that can be generally used in the mitigation process.

7.1.3 Cycle slip

A new multi-scale singularity detection technique combined with the Lipchitz exponent estimation procedure to detect and estimate cycle slip in GPS measurements is introduced. The proposed technique can detect precisely the location of cycle slip in noisy measurements and rejects the faulty singularities caused by noise. The performance of the proposed technique is evaluated and assessed over GPS code minus carrier and Phase1 minus Phase2 measurements where different cycle slips are added to the measurements. Also, the performance of the proposed technique is tested over CmC test quantities under SNR range from 20 to 50. All the simulated cycle slips in CmC test quantities with SNR bigger than 30 are effectively detected by the proposed technique. The error in the estimation process is less than 0.1 cycles most of the time.

7.2 Recommendations

The following is a list of some areas requiring future work and further investigation:

- The list of wavelet families used in this study was selected based on suggestions from the author's experience, other studies, and the wavelet literature. The researcher recommends further testing on other orthogonal wavelets, especially since there are a large number of wavelet families available.

- The wavelet algorithm introduced in this thesis requires modifications for its application on long baseline error mitigation, especially to reduce the bias that is introduced in long baselines. An example is the use of second generation wavelets [Soltanpour et al., 2006].

- The behavior of the proposed multi-scale cycle slips detection and estimation in real-time scenarios should be further investigated. The primary challenge in applying this implementation in real-time situations will be the edge effect. Further investigation is required to identify its cause and propose a method for treating it.

- Further research is required for the implementation of the new wavelet algorithm for multipath mitigation in real-time scenarios. The localization and zooming capabilities of the proposed multi-resolution technique can be strongly used for detection and mitigation of DGPS errors in real-time for both code and phase measurement.

References

Aram, M., A. El-Rabbany, S. Krishnan, and A. Anpalagan (2007), "Single frequency multipath mitigation based on wavelet analysis," Journal of Navigation, 60(2),281-90.

Beutler, G., H. Bock, E. Brockmann, R. Dach, W. Gurtner, H. Habrich, U. Hugentobler, D. Ineichen, A. Jaeggi, M. Meindl, L. Mervart, S. Rothacher, R. Schaer, T. Springer, P. Steigenberger, D. Svehla, D. Thaller, C. Urschl, and R. Weber (2006), "BERNESE GPS software ," Universität Bern.

Bisnath, S. B. and R. B. Langley (2000), "Automated cycle-slip correction of dual-frequency kinematic GPS data," in Proceedings of the 47th Annual Conference of the Canadian Aeronautics and Space Institute, 121-5.

Blewitt, G. (1989), "Carrier Phase Ambiguity Resolution for GPS Applied to Geodetic Baseline up to 2000km," Geophysical Research Journal, Vol.94, No. B8, PP 10187-10203.

Blewitt, G. (1990), "An automatic editing algorithm for GPS data," Geophysical Research Letters, 17(3), 199-202.

Bock, Y., R. M. Nikolaidis, P. J. De Jonge, and M. Bevis (2000), "Instantaneous geodetic positioning at medium distances with the Global Positioning System," Journal of Geophysical Research, 105(B12), 223-58.

Braasch, M. S. (1994), "Optimum antenna design of DGPS ground reference stations," in ION GPS-94, Seventh International Meeting of the Satellite Division of the Institute of Navigation.

Bradbury, J., Ziebart, M., Cross, P.A., Boulton, P., and Read, A.(2007), “Code Multipath Modeling in the Urban Environment Using Large Virtual Reality City Models: Determining the Local Environment”. Journal of Navigation. Vol. 60, p. 95-105

Brunner, F. K. and M. Gu (1991), "An improved model for the dual-frequency ionospheric correction of GPS observations," Manuscripta Geodaetica, 16(3), 205-14.

Cannon, M. E., G. Lachapelle, W. Qiu, S. L. Frodge, and B. Remondi (1994), "Performance analysis of a narrow correlator spacing receiver for precise static GPS positioning," in Proceedings of 1994 IEEE Position, Location and Navigation Symposium - PLANS'94, 11-15 April 1994 New York, NY, USA: IEEE, 355-60.

Chenxi, L., L. Yunhua, L. Kui, Z Bocheng, and Z. Lezhu (2010), "Cycle slip processing based on wavelet reconstruction for single-frequency GPS signal in kinetic precise point positioning," in Signal Processing (ICSP), 2010 IEEE 10th International Conference, 2527-30.

Collin, F. and R. Warnant (1995), "Application of the Wavelet Transform for GPS Cycle Slip Correction and Comparison with Kalman Filter," Manuscripta Geodaetica, 20(3), 161-72.

Counselman, C. (1998), "Array antennas for DGPS," IEEE Aerospace and Electronic Systems Magazine, 13(12), 15-9.

Dammalage, T. L., C. Satirapod, S. Kibe, and C. Ogaja (2009), " Wavelet transform application to C/A code multipath mitigation at GPS reference stations for improved differential GPS corrections," Accepted for publication in Survey Review.

Daubechies (1992), Ten Lectures on Wavelets. PA SIAM.

Donoho, D. L. and I. M. Johnstone (1994), "Ideal spatial adaptation by wavelet shrinkage," Biometrika, 81 425-55.

El-Ghazouly, A., M. Elhabiby, and N. El-Sheimy (2008a), "Wavelet-Based Carrier Phase Multipath Reduction," the United States and Trade Mark Office(Submitted,September 28th,2008.12 pages).

El-Ghazouly, A., M. Elhabiby, and N. El-Sheimy (2008b), "Assessment of Wavelets Analysis for Carrier Phase Multipath Mitigation," Canadian Journal of Earth Sciences.

El-Ghazouly, A., M. Elhabiby, and N. El-Sheimy (2009), "The use of Wavelets in GPS Error Analysis with Emphasis to Singularity Detection and Multipath Removal," in The American Geophysical Union Joint Assembly.

El-Ghazouly, A. (2009), "The Aid of Wavelets Correlator in Carrier Phase Multipath Reduction and Motion Detection," in ION GNSS 2009.Session E2: Multipath Effects & Mitigation, September.

El-Ghazouly, A., M. Elhabiby, and N. El-Sheimy (2010), "De-Trending Multi-resolution technique to Reduce/Eliminate Long Baselines errors in Static GNSS Mode," in European Navigation Conference ENC.

El-Ghazouly, A., M. Elhabiby, and N. El-Sheimy (2011), "Multiresolution real-time (MRRT) code-smoothing technique," Journal of Applied Geodesy, Volume 5(Issue 3-4), 147-54.

Elhabiby, M. (2007), "Wavelet Representation of Geodetic Operators," Ph.D. University of Calgary.

Elhabiby, M., A. El-Ghazouly, and N. El-Sheimy (2010), "Wavelet Spectral Techniques for GPS Errors Reduction," in 7th International Conference on Electrical Engineering.

Elhabiby, M., A. El-Ghazouly, and N. El-Sheimy (2010), "Multi-Resolution Ionospheric Attenuation for Single Frequency Receivers," in INTERGEO.

Fenton, P. and P. Jones (2005), "The theory and performance of NovAtel Inc.'s vision correlator," in Proceedings of ION GNSS.

Garin, L., F. van Diggelen, and J. Rousseau (1996), "Strobe & Edge Correlator Multipath Mitigation for Code,"in Proceedings of ION GPS-96 , 657-64.

Garin, L. and J. Rousseau (1997), "Enhanced Strobe Correlator Multipath Rejection for Code & Carrier," in Proceedings of ION GNSS, 559-68.

Grewal, M. S., L. R. Weill, and A. P. Andrews (2007), GLOBAL POSITIONING SYSTES, INERTIAL NAVIGATION, AND INTEGRATION. Hoboken, New Jersey.: John Wiley & Sons, Inc.

Han, S. and C. Rizos (1997), "Multipath effects on GPS in mine environments," Fremantle, Australia: 447-57.

Han, S. (1997), "Carrier phase-based long-range GPS kinematic positioning," UNISURV S-49, School ofGeomatic Engineering, The University of NewSouth Wales.

Hansen, Andrew J., Todd Walter, and Per Enge (1997), "Ionospheric correction using tomography," in Proceedings of the 1997 10th International Technical Meeting of the Satellite Division of the Institute of Navigation, ION GPS-97. Part 1 (of 2), September 16, 1997 - September 19, 1997 Kansas City, MO, USA: Inst of Navigation, 249-57.

Hatch, R. (1982), "The synergism of GPS code and carrier phase measurements," in Proceedings of the 3rd international geodetic symposium on satellite doppler position in new Mexico: 1213-32.

Hernandez-Pajares, M., J. M. Juan, and J. Sanz (1999), "New approaches in global ionospheric determination using ground GPS data," Journal of Atmospheric and Solar-Terrestrial Physics, 61(16), 1237-47.

Hofmann-Wellenhof, B., H. Lichtenegger, and J. Collins (2001), Global Positioning System theory and practice. Springer Wien New York.

Hopfield, H. S. (1969), "Two-quartic tropospheric refractivity profile for correcting satellite data," Journal of Geophysical Research, 74(18), 4487-99.

Huang, B., L. Liu, G. Gao, and J. Zhou (2006), "Detection of cycle-slip in the GPS precise point positioning based on wavelet transform," Geomatics and Information Science of Wuhan University, 31(6), 512-5.

Hubbard, B. B. (1998), The world according to wavelets: the story of a mathematical technique in the making. Wellesley, Mass.

Hugentobler, U., S. Schaer, P. Fridez, G Beutler, H. Bock, E. Brockmann, R. Dach, W. Gurtner, D. Ineichen, J. Johnson, M. Meindl, L. Mervart, T. Springer, and R. Weber (2001), "Bernese GPS Software, Version 4.2," University of Bern, 2001.

Izadpanah, A., C. O´Driscoll, and G. Lachapelle (2008), "GPS Multipath Parameterization and Mitigation Based on Kalman Filtering," in GNSS08 (Savannah, GA, 16-19 Sep, Session C2).

Jones, P., P. Fenton, and B. Smith (2004), "Theory and performance of the pulse aperture correlator," in Tech.Rep., NovAtel, Calgary, Alberta, Canada.

Keller, W. (2004), Wavelets in geodesy and geodynamics. Walter De Gruyter Inc.

Klobuchar, J. A. (1986), "Design and characteristics of the GPS ionospheric time delay algorithm for single frequency users," in IEEE PLANS '86 Position Location and Navigation Symposium. Record (Cat. No.86CH2365-5), 4-7 Nov. 1986 New York, NY, USA: IEEE, 280-6.

Klobuchar, J. A. (1987), "Ionospheric time-delay algorithm for single-frequency GPS users," IEEE Transactions on Aerospace and Electronic Systems, AES-23(3), 325-31.

Komjathy, J. A. (1997), "Global ionospheric total electron content mapping using the global positioning system," Ph.D. dissertation Department of Geodesy and Geomatics Engineering .

Kunysz, W. (2005), "High performance GPS pinwheel antenna," http://www.novatel.com/Documents/Papers/ gps_pinwheel_ant.pdf .

Laxton, M. C. and S. L. DeVilbiss (1997), "GPS multipath mitigation during code tracking," in Proceedings of 16th American CONTROL Conference, 4-6 June 1997 Evanston, IL, USA: American Autom. Control Council, 1429-33.

Lee, H. K., J. Wang, and C. Rizos (2003), "Effective cycle slip detection and identification for high precision GPS/INS integrated systems," Journal of Navigation, 56(3), 475-86.

Lee, Y. W., Y. C. Suh, and R. Shibasaki (2008), "A simulation system for GNSS multipath mitigation using spatial statistical methods," Computers & Geosciences, 34(11), 1597-609.

Linlin, Ge., S. Han, and C. Rizos (2000), "Multipath mitigation of continuous GPS measurements using an adaptive filter," GPS Solutions, 4(2), 19-30.

Liu, T., S. Li, R. Wang, W. Jiang, and J. Jia (2011), "Adaptive detection and modification algorithm of GPS cycle slips based on wavelet analysis," in International Conference on Mechatronic Science, Electric Engineering and Computer (MEC), 1907-10.

Liu, J. (2003), "Implementation and Analysis of GPS Ambiguity Resolution Strategies in Single and Multiple Reference Station Scenarios," Msc. University of Calgary.

Mallat, S. and W. L. Hwang (1992), "Singularity detection and processing with wavelets," IEEE Transactions on Information Theory, 38(2), 617-43.

Mallat, S. (1998), A wavelet tour of signal processing. Academic Press.

Mao, A., C. Harrison, and T. Dixon (1999), "Noise in GPS coordinate time series," Journal of Geophysical Research: Solid Earth, Volume 104(Issue B2), 2797-816.

Mendes, V. B. (1999), "Modeling The Neutral-Atmosphere Propagation Delay in Radiometric Space Techniques," Ph.D. dissertation Department of Geodesy and Geomatics Engineering.

Meng, L. and L. Jia-Hong (2010), "Cycle slips and outliers detection based on biorthogonal wavelet transform modulus maximum," in International Conference on Computer Application and System Modeling (ICCASM).

Misra, P. and P. Enge (2006), “Global Positioning System Signals, Measurements, and Performance”. 2nd Edition. Ganga-Jamuna Press, Lincoln, MA

Mitchell, C. N. and P. S. J. Spencer (2003), "A three-dimensional time-dependent algorithm for ionospheric imaging using GPS," Annals of Geophysics, 46(4), 687-96.

Ogaja, C., J. L. Wang, and C. Rizos (2003), "Detection of wind-induced response by wavelet transformed GPS solutions," ASCE- Journal of Surveying Engineering-, 129(3), 99-104.

Ogaja, C. and C. Satirapod (2007), "Analysis of high-frequency multipath in 1-Hz GPS kinematic solutions," GPS Solutions, 11(4), 269-80.

Ogden, R. T. (1997), Essential wavelets for statistical applications and data analysis. Birkhäuser.

Park, K. D., R. S. Nerem, M. S. Schenewerk, and J. L. Davis (2004), "Site-specific multipath characteristics of global IGS and CORS GPS sites," Journal of Geodesy, 77(12), 799-803.

Ragheb, A. E., P. J. Clarke, and S. J. Edwards (2007), "GPS sidereal filtering: coordinate- and carrier-phase-level strategies," Journal of Geodesy, Volume 81(Issue 5), 325-35.

Raquet, J. and G. Lachapelle (1996), "Determination and reduction of GPS reference station multipath using multiple receivers," in Proceedings of the 1996 9th International Technical Meeting of the Satellite Division of the Institute of Navigation, ION GPS-96. Part 1 (of 2), September 17, 1996 - September 20, 1996 Kansas City, MO, USA: Inst of Navigation, 673-81.

Ray, JK. (2000), "Mitigation of GPS Code and Carrier Phase Multipath Effects using a Multi-Antenna System," Ph.D. thesis University of Calgary.

RTCA Inc. (1998), "Minimum Aviation System Performance Standards for the Local Area Augmentation System (LAAS),".

Saastamoinen, J. (1973), "Contributions to the theory of atmospheric refraction, part II: refraction corrections in satellite geodesy," Bulletin Géodésique, 107 13-34.

Satirapod, C. and C. Rizos (2005), "Multipath mitigation by wavelet analysis for GPS base station applications," Survey Review, 38(295), 2-10.

Schenewerk M. (2003), "A brief review of basic GPS orbit interpolation strategies", GPS solutions, Volume 6, Number 4. pp 265-267.

Shallberg, K, P Shloss, E Altshuler, and L Tahmazyan (2001), "WAAS Measurement Processing, Reducing the Effects of Multipath," in ION GPS 2001.

Shi, Xing, Xue Su, and Ren Sheng (2005), "Cycle-slip detection of GPS carrier phase observable based on wavelet technology," Journal of Nanjing University of Science and Technology, 29(1), 105-22.

Soltanpour A., H. Nahavandchi, and W. F eatherstone (2006). “The use of second-generation wavelets to combine a gravimetric quasigeoid model with GPS-levelling data.: Journal of Geodesy, 80(2), pp.82-93.

Souza, E. M. and J. F. G. Monico (2004), "Wavelet shrinkage: High-frequency multipath reduction from GPS relative positioning," GPS Solutions, 8(3), 152-9.

Souza, E. M. and J. F. G. Monico (2007), "The wavelet method as an alternative for reducing ionospheric effects from single-frequency GPS receivers," Journal of Geodesy, 81(12), 799-804.

Strang, G. and T. Nguyen (1996), Wavelets and Filter Banks. Wellesley- Cambridge Press.

Tait, M., L. Sheng, and M. E. Cannon (2008), "The Feasibility of Replacing Precise Levelling with GPS for Permafrost Deformation Monitoring," in INGEO 2004 and FIG Regional Central and Eastern European Conference on Engineering Surveying.

Teunissen, P. J. G. (1993), "Least squares estimation of the integer GPS ambiguities," in General Meeting of the IAG.

Tinghua, Yi, Li Hongnan, and Wang Guoxin (2006), "Cycle slip detection and correction of GPS carrier phase based on wavelet transform and neural network," in 2006 6th International Conference on Intelligent Systems Design and Applications, 16-18 Oct. 2006 Los Alamitos, CA, USA: IEEE Computer Society, 5.

Townsend, B. and P. Fenton (1994), "A Practical Approach to the Reduction of Pseudo-range Multipath Errors in a L1 GPS Receiver," in Proceedings of ION GPS-94, 143-8.

Van Dierendonck, A. J., P. Fenton, and T. Ford (1992), "Theory and Performance of Narrow Correlator Spacing in a GPS Receiver," Journal of The Institute of Navigation, 39(3), 265-83.

Van Nee, R. D. J. (1995), "Multipath and Multi-Transmitter Interference in Spread Spectrum Communication and Navigation Systems," Ph.D. Delft University Press.

Walnut, D. (2002), An Introduction to Wavelet Analysis. Birkhauser Boston.

Wang, G., Z. Wang, and H. Yin (2007), "An cycle-slip correction method for real-time kinematic GPS data based on triple differences observation," Geomatics and Information Science of Wuhan University, 32(8), 711-4.

Wang, J., J. L. Wang, and C. Roberts (2009), "Reducing GPS Carrier Phase Errors with Emd-Wavelet for Precise Static Positioning," Survey Review, 41(312), 152-61

Weiss, J.P., Axelrad, P. and Anderson, S. (2006),"Assessment of Digital Terrain Models for multipath Prediciton at Geodetic GNSS Installations". Proceedings of the ION GNSS 19th International Technical Meeting of the Satellite Division, p. 2815-2823, September 2006, Fort Worth, TX.

Xiong, Y. L., D. F. Huang, and C. K. Shum (2003), "GPS phase measure cycle-slip detecting and GPS baseline resolution based on wavelet transform," Survey Review, 37(289), 200-7.

Zhang, H. P., W. Y. Zhu, J. H. Peng, and C. Huang (2005), "Analysis of the ionosphere wave-motion with GPS," Chinese Science Bulletin, 50(13), 1373-81.

Zhang, Y and C. Bartone (2004), "Multipath mitigation in the frequency domain," in PLANS 2004. Position Location and Navigation Symposium, 26-29 April 2004 Piscataway, NJ, USA: IEEE, 486-95.

Zhao, J., Y. Ma, H. Gao, and J. Yang (2000), "Denoising Method of AE Signal by Using Wavelet Transform," in 15th World Conf.on NDT.

Zheng, Z., X. Lu, and X. Han (2008), "GPS phase measurement cycle-slip detection based on a new wavelet function," Geomatics and Information Science of Wuhan University, 33(6), 639-43.

Zhong, P., X. L. Ding, D. W. Zheng, W. Chen, and D. F. Huang (2008), "Adaptive wavelet transform based on cross-validation method and its application to GPS multipath mitigation," Gps Solutions, 12(2), 109-17.